2006

The ACS Virgo Cluster Survey. VI. Isophotal Analysis and the Structure of Early-Type Galaxies

Laura Ferrarese

Patrick Cote

Andres Jordan

Recommended Citation
Astrophysical Journal Supplement Series 164 (2006) 334-434

Accepted by The Astrophysical Journal Supplements
Preprint typeset using LaTeX style emulateapj v. 10/10/03

THE *ACS* VIRGO CLUSTER SURVEY. VI. ISOPHOTAL ANALYSIS AND THE STRUCTURE OF EARLY-TYPE GALAXIES[1]

Laura Ferrarese[2], Patrick Côté[2], Andrés Jordán[3,4], Eric W. Peng[2], John P. Blakeslee[5,6], Slawomir Piatek[7], Simona Mei[5], David Merritt[8], Miloš Milosavljević[9,10], John L. Tonry[11], & Michael J. West[12]

Accepted by The Astrophysical Journal Supplements

ABSTRACT

We present a detailed analysis of the morphology, isophotal parameters and surface brightness profiles for 100 early-type members of the Virgo Cluster, from dwarfs ($M_B = -15.1$ mag) to giants ($M_B = -21.8$ mag). Each galaxy has been imaged in two filters, closely resembling the Sloan g and z passbands, using the *Advanced Camera for Surveys* on board the *Hubble Space Telescope*.

Dust and complex morphological structures are common. Dust is detected in as many as 18, preferentially bright, galaxies. The incidence rate in the 26 galaxies brighter than $B_T = 12.15$ mag, which form a magnitude limited sample, is 42%. The amount and distribution of dust show no obvious correlations with galaxy morphology; dust features range from faint wisps and patches on tens of parsec scales, to regular, highly organized kpc-scale dust disks. Blue star clusters are interspersed within the larger, clumpier dust disks, while thin, dynamically cold stellar disks are seen in association with the smaller, uniform nuclear dust disks.

Kiloparsec-scale stellar disks, bars, and nuclear stellar disks are seen in 60% of galaxies with intermediate luminosity ($-20 \lesssim M_B \lesssim -17$). In at least one case (VCC 1938 = NGC 4638), the large-scale stellar disk has a sharp inner edge, possibly produced when disk instabilities led to the formation of a (now dissolved) bar. This process might indeed be seen unfolding in one galaxy, VCC 1537 (=NGC 4528). A spiral structure might be present in VCC 1199, an elliptical companion of M49. In dwarf galaxies, spiral structures are confirmed in VCC 856 and detected for the first time in VCC 1695.

Surface brightness profiles, ellipticities, major axis position angles, and isophotal shapes are derived typically within 8 kpc from the center for the brightest galaxies, and 1.5 kpc for the faintest systems, with a resolution (FWHM) of 7 pc. For all but 10 of the galaxies, the surface brightness profiles are well described by a Sérsic model with index n which increases steadily from the fainter to the brightest galaxies. In agreement with previous claims, the inner profiles (typically within 100 pc of the center) of eight of the 10 brightest galaxies, to which we will refer as "core" galaxies, are lower than expected based on an extrapolation of the outer Sérsic model, and are better described by a single power-law function. Core galaxies are clearly distinct in having fainter central surface brightness, μ_0, and shallower logarithmic slope of the inner surface brightness profile, γ, than expected based on the extrapolation of the trend followed by the rest of the sample, for which both μ_0 and γ increase steadily with galaxy magnitude. Large-scale, global properties also set core galaxies apart: the effective radius in particular is found to be almost one order of magnitude larger than for only slightly less luminous non-core galaxies. Contrary to previous claims, we find no evidence in support of a strong bimodal behavior of the inner profile slope, γ; in particular the γ distribution for galaxies which do not show evidence of multiple morphological components (disks or bars) is unimodal across the entire magnitude range (a factor 460 in $B-$band luminosity) spanned by the ACSVCS galaxies. Although core galaxies have shallow inner profiles, the shallowest profiles (lowest γ values) are found in faint dwarf systems. The widely adopted separation of early-type galaxies between "core" and "power-law" types, which had originally been prompted by the claim of a clear bimodal distribution of γ values, is therefore untenable based on the present study.

Once core galaxies are removed, dwarf and bright ellipticals display a continuum in their morphological parameters, contradicting some previous beliefs that the two belong to structurally distinct classes. However, dwarfs span a wider range in morphological characteristics than brighter systems: their surface brightness profiles vary from exponential to almost $r^{1/4}$ laws, they comprise both nucleated and non-nucleated varieties, and several systems display evidence of disks, spiral structures and recent star formation. This is taken as evidence that dwarf galaxies, as currently classified, form a heterogeneous class.

Subject headings: galaxies: clusters: individual (Virgo)–galaxies: ISM: dust–galaxies: elliptical and lenticular–galaxies: nuclei

[1] Based on observations with the NASA/ESA *Hubble Space Telescope* obtained at the Space Telescope Science Institute, which is operated by the association of Universities for Research in Astronomy, Inc., under NASA contract NAS 5-26555.

1. INTRODUCTION

The innermost regions of galaxies have long played a pivotal role in guiding our understanding of how galaxies form and evolve. Beginning in the mid 1980's, ground-based studies started to pave the way towards a characterization of the core (by "core" we hereby refer loosely to the innermost few hundred parsecs) structural parameters (Lauer 1985; Kormendy 1985). However, the full extent of the diversity and complexity of the core structure was not fully appreciated until high-resolution *Hubble Space Telescope* (HST) images became available (Crane et al. 1993; Jaffe et al. 1994; Ferrarese et al. 1994; van den Bosch et al. 1994; Forbes, Franx & Illingworth 1995; Lauer et al. 1995, 2002, 2005; Verdoes Kleijn et al. 1999; Quillen, Bower, & Stritzinger 2000; Rest et al. 2001; Ravindranath et al. 2001; Laine et al. 2003). These studies unveiled the existence of small, 100 pc scale, nuclear stellar and gas/dust disks, which have become instrumental in probing the central potential and the masses of central compact objects (Harms et al. 1994; Ferrarese et al. 1996; van der Marel & van den Bosch 1998). They exposed nuclear bars and "evacuated" cores, possibly scoured out by the coalescence of supermassive black holes. They allowed the study of the properties of dust and nuclear star clusters. In short, these observations dispelled the myth of elliptical galaxies as easily characterizable, regular, dust-free stellar systems.

Despite a limited sample of just seven early-type galaxies (all but one within 15 Mpc, observed with the pre-refurbishment HST *Faint Object Camera* in one or more bands resembling Johnson's U, B and V filters), the first HST study by Crane et al. (1993) established that in none of the galaxies could the surface brightness profile be characterized as isothermal. This result was subsequently confirmed by Ferrarese et al. (1994) based on a somewhat larger and magnitude limited sample of 14 early-type galaxies in the Virgo cluster, observed in a single filter ($\sim$ Johnson's V) with the HST *Planetary Camera 1*. Capitalizing on the completeness of their sample, Ferrarese et al. (1994) noted that, for the brightest half of their Virgo galaxies, the surface brightness profile could be characterized as a broken power-law (these galaxies were referred to as "Type I"). For the rest of the sample ("Type II" galaxies), the profiles could be reasonably well described by a single power-law to the smallest radii resolved by the instrument.

These issues were revisited in a series of papers by Lauer et al. (1995), Gebhardt et al. (1996), Byun et al. (1996), and Faber et al. (1997). Armed with a larger sample of 45 to 61 galaxies (depending on the paper), including a few spirals, these studies significantly strengthened the conclusion that in no cases were cores observed to have constant central surface density. Lauer et al. (1995) applied Hernquist's (1990, his equation 43) double power-law model to the surface brightness profiles of their galaxies − the model, dubbed "Nuker law" by the authors, is similar to the broken power-law proposed by Ferrarese et al. 1994, but includes an additional parameter regulating the transition between the outer and inner power-laws. Lauer et al. advocated the view that early-type galaxies can be divided cleanly in two classes (which those authors named "core" and "power-law" and correspond closely to the Type I and Type II galaxies in Ferrarese et al. 1994) based on their central surface brightness profiles. The working definition of a "core" galaxy in Lauer et al. (1995) is a galaxy for which the logarithmic slope of the profile within the break radius (i.e., the transition radius between the inner and outer power-law) is $\gamma < 0.3$. The authors also found that the distribution of γ is bimodal, with no galaxies in the range $0.3 < \gamma < 0.5$.

Although ground-breaking, the study of Lauer et al. (1995) suffered from an ill-defined sample (although the galaxies span a wide range in luminosities $-15.1 < M_V < -23.82$ and structural properties, they are sampled at vastly different spatial resolutions, ranging in distance between 3 and 280 Mpc, and were partly selected for exhibiting features deemed interesting), and the fact that all observations were made in one band ($\sim$ Johnson's V) with the pre-refurbished HST. These shortcomings have been partly overcome by Rest et al. (2001) and Lauer et al. (2005). Both of these investigations capitalize on the use of the refurbished HST *Wide Field and Planetary Camera 2* (WFPC2), but take rather different approaches to sample selection. Rest et al. (2001) randomly targeted an unbiased (though incomplete) sample of 67 galaxies selected from a magnitude and space-limited sample of 130 objects within 54 Mpc. Each galaxy was observed in a single band, similar to Johnson's R. The Lauer et al. (2005) sample, on the other hand, is not easily characterizable, being comprised of 77, mainly bright early-type galaxies at distances between 10 and 100 Mpc. These galaxies were observed as part of unrelated HST programs (and therefore with different filter configurations and varying signal-to-noise ratios) and downloaded from the HST public archive. Despite these drawbacks, the Lauer et al. (2005) study was the first to make extensive use of color information, with roughly half of the sample observed in two filters, $\sim$ Johnson's V and I.

Both studies confirmed the presence of dust in roughly half of the galaxies. Rest et al. (2001) find embedded nuclear stellar disks in 51% of their sample, while Lauer et al. (2005) suggest that "all power-law galaxies harbor disks; their visibility is simply due to viewing angle",

[2] Herzberg Institute of Astrophysics, National Research Council of Canada, 5071 West Saanich Road, Victoria, BC, V8X 4M6, Canada; laura.ferrarese@nrc-cnrc.gc.ca, patrick.cote@nrc-cnrc.gc.ca, eric.peng@nrc-cnrc.gc.ca
[3] European Southern Observatory, Karl-Schwarzschild-Str. 2, 85748 Garching, Germany; ajordan@eso.org
[4] Astrophysics, Denys Wilkinson Building, University of Oxford, 1 Keble Road, Oxford, OX1 3RH, UK
[5] Department of Physics and Astronomy, The Johns Hopkins University, 3400 North Charles Street, Baltimore, MD 21218-2686; jpb@pha.jhu.edu, smei@pha.jhu.edu
[6] Department of Physics and Astronomy, PO Box 642814, Washington State University, Pullman, WA 99164
[7] Department of Physics, New Jersey Institute of Technology, Newark, NJ 07102; piatek@physics.rutgers.edu
[8] Department of Physics, Rochester Institute of Technology, 84 Lomb Memorial Drive, Rochester, NY 14623; merritt@cis.rit.edu
[9] Theoretical Astrophysics, California Institute of Technology, Mail Stop 130-33, Pasadena, CA 91125; milos@tapir.caltech.edu
[10] Sherman M. Fairchild Fellow
[11] Institute for Astronomy, University of Hawaii, 2680 Woodlawn Drive, Honolulu, HI 96822; jt@ifa.hawaii.edu
[12] Department of Physics and Astronomy, University of Hawaii, Hilo, HI 96720; westm@hawaii.edu

at odds with previous claims in Lauer et al. (1995) but in agreement with Ferrarese et al. (1994). Lauer et al. (2005) reaffirm the strong dichotomy in the distribution of γ, with core galaxies having $\gamma < 0.3$ and power-law galaxies having "a steep $\gamma > 0.5$ cusp [which] continues into the HST resolution limit". This conclusion is based on Nuker model fits to the surface brightness profiles, despite warnings by Rest et al. (2001) that the dichotomous behavior of core and power-law galaxies observed by Lauer et al. (1995) might be partly due to the fact that the adoption of the Nuker model will bias the value of the inner slope for profiles with slopes that vary smoothly with radius. By introducing a non-parametric estimate of the logarithmic slope of the inner profile, Rest et al. (2001) find that core and power-law galaxies form a continuous sequence, with "transition" objects bridging the gap between the two, a conclusion also reached by Ravindranath et al. (2001) based on HST/NICMOS data.

The stability of Nuker model fits has been challenged most recently by Graham et al. (2003). The authors conclusively demonstrated that the recovered Nuker model parameters are sensitive to the radial extent of the data being fitted, owing to the simple fact that the kpc-scale surface brightness profiles of early-type galaxies are not well described by power-laws. Graham et al. (2003) and Trujillo et al. (2004) show that a Sérsic model (Sérsic 1968) provides a more stable and accurate parametrization of the surface brightness profiles for all but the brightest early-type galaxies, which are best described by a Sérsic model transitioning to a power-law in the inner regions. The authors define as "core" galaxies displaying "a deficit of flux relative to the inward extrapolation of the outer Sérsic profile". In a follow-up paper, Graham & Guzman (2003) find that the distribution of the inner profile slope is continuous, with γ increasing steadily from dwarf to giant ellipticals, only to decrease again for the very brightest ($M_B < -20.5$ mag) systems.

This paper presents the next effort in the characterization of the properties of early-type galaxies. Based on data obtained with the *Wide Field Channel* (WFC) of the HST *Advanced Camera for Surveys* (ACS), we discuss the morphology and structural parameters for 100 confirmed early-type members of the Virgo cluster, each imaged in the g and $z-$bands. Compared to previous studies, the sample presented in this paper is superior in terms of sample size, completeness and dynamic range (a factor 460 in $B-$band luminosity), depth (a factor three higher signal-to-noise ratio compared to a typical galaxy in the most recent study by Lauer et al. 2005), color baseline (a factor 1.5 greater wavelength range compared to Johnson's V and I, with all galaxies observed in two bands), spatial resolution (a factor of ∼three improvement compared to studies based on WFPC2 data, due both to the smaller distance of Virgo, and to the sharper ACS/WFC point spread function), and field of view (a factor 25 in area compared to studies based on WFPC2 data). This is the sixth paper in a series discussing results from the ACS Virgo Cluster Survey (ACSVCS). Previous papers have discussed the scientific rationale and observational planning (Côté et al. 2004, hereafter Paper I), data reduction pipeline (Jordán et al. 2004a, hereafter Paper II), the X-ray binary population in M87 (Jordán et al. 2004b), the calibration of Surface Brightness Fluctuations (SBF) for distance measurements (Mei et al. 2005a,b), the discovery of the population of ultra-compact dwarfs (Hasegan et al. 2005), the properties of the galaxy nuclei (Côté et al. 2005, hereafter Paper VIII), the color distribution and half-light radii of the globular clusters (Peng et al. 2005a; Jordán et al. 2005), and the nature of diffuse star clusters (Peng et al. 2005b).

The structure of this paper is as follows. The sample selection and observational setup are described in §2. Data analysis, including basic image reduction, correction for internal dust extinction, recovery of the isophotal parameters, and parametrization of the surface brightness profiles can be found in §3. The next section reports on the morphological characteristics of the sample galaxies (incidence of dust and other morphological peculiarities, such as stellar disks, rings, bars and spiral structures, §4.1), the choice of parametrization of the surface brightness profiles (§4.2), and scaling relations linking the structural parameters (§4.3). A general discussion is given in §5, where we reconsider the definition of "core" galaxies and discuss their association with supermassive black holes (SBHs, §5.1 and §5.2), address the connection between dwarf and giant early-type galaxies (§5.3), comment on the isophotal shapes (§5.4) and present color-color and color-magnitude diagrams (§5.5). Notes on individual galaxies are presented in an Appendix.

In this paper, we adopt a distance modulus to Virgo of 31.09 ± 0.03 (random) ± 0.15 (systematic) mag, which corresponds to the mean Cepheid-calibrated surface brightness fluctuation (SBF) distance as determined by Tonry et al. (2001), corrected to reflect the latest calibration of the Cepheid PL relation (Freedman et al. 2001; Blakeslee et al. 2002). The same mean distance modulus to Virgo serves as the calibration for the SBF distance scale adopted by Mei et al. (2005) for the ACSVCS galaxies. The corresponding linear distance is 16.52 ± 0.22 (random) ± 1.14 (systematic) Mpc. At this distance, $1''$ corresponds to $80.1 \pm 1.1 \pm 5.53$ pc, and the ACS/WFC pixel scale ($0''.049$) to $3.92 \pm 0.05 \pm 0.26$ pc.

2. SAMPLE DESCRIPTION AND OBSERVATIONAL STRATEGY

We refer the reader to Paper I for a comprehensive description of the sample and the scientific rationale that motivated the observational setup. In essence, the ACSVCS comprises high resolution HST g and $z-$band images of 100 early-type galaxies, selected from the Virgo Cluster Catalog (VCC) of Binggeli et al. (1985). Our initial sample consisted of all galaxies 1) classified in the VCC as "certain" or "probable" members of Virgo, based on the observed morphology, surface brightness, and (when available) radial velocity; 2) located above $+5°$ in declination, thereby excluding galaxies in the Southern Extension (Sandage et al. 1985); 3) brighter than $B_T = 16$ mag; and 4) with an E, S0, dE, dE,N, dS0 or dS0,N morphological classification. This sample of 163 galaxies was further trimmed to a total of 100 galaxies due to observing time limitations, by excluding S0 or dwarf galaxies with uncertain or disturbed morphology, significant dust contamination, lacking a visible bulge component, or previously imaged with the WFPC2 (see Paper I for details). The final ACSVCS sample spans a range of 460 in blue luminosity ($9.31 \leq B_T \leq 15.97$).

As an early-type galaxy catalog, it is magnitude limited down to $B_T < 12.15$ mag (26 galaxies), and 54% complete in the $12.15 < B_T < 16.00$ magnitude range. If only E galaxies are considered, the catalog is complete and magnitude limited over the entire luminosity range. Morphologically, 25% of the ACSVCS galaxies are classified in the VCC as E, 33% as S0, 7% as E/S0, 5% as dE, 24% as dE,N, and 6% as dS0. Basic properties of the galaxies, ordered by increasing B_T magnitude (decreasing luminosity), are listed in Table 1. In addition to right ascension and declination (both from NED), we list B_T (from the VCC, uncorrected for extinction), J, H, and K_s isophotal magnitudes and errors from 2MASS (see below), foreground extinction $E(B-V)$ (from Schlegel et al. 1998), heliocentric systemic velocity (from NED) and Hubble type (from the VCC). Infrared photometry was retrieved from the 2MASS All-Sky Extended Source Catalog for all but the brightest 15 of galaxies, for which the 2MASS Large Galaxy Atlas was used instead (Jarrett et al. 2003). In all cases, the magnitudes listed in Table 1 were measured within a $K_s = 20$ mag arcsec^{-2} elliptical isophotal aperture.

All ACSVCS observations were carried out with the *Wide Field Channel* (WFC) of the *Advanced Camera for Surveys* (ACS) between 2002, December 25 and 2003, December 28. The WFC consists of two 2048×4096 pixel CCDs (WFC1 and WFC2), with a spatial scale of 0″.049/pixel. For each galaxy, the center was placed on the WFC1 chip at the reference pixel position (2096,200), and then offset away from the gap separating the two chips by an additional 5″ to 10″. In practice, therefore, the center of each galaxy is $\sim 130''$ and $\sim 155''$ from the nearest and farthest corners of the CCD, respectively, and 15″ to 20″ from the gap separating the WFC1 and WFC2 CCDs. Each galaxy was observed with an identical strategy. Exposures in F475W (which resembles the SDSS g filter) totaled 750s, split in a pair of 375s exposures to aid the removal of cosmic rays. Exposures in F850LP ($\sim$ SDSS z) totaled 1210s and were divided in a pair of 560s exposure plus a shorter 90s exposure; the latter was designed to allow recovery of the central regions of galaxies whose nuclei might saturate in the longer 560s exposure. All observations were performed in fine lock, giving a nominal pointing stability of 5 mas (RMS) or better over 60-second intervals.

3. DATA REDUCTION AND ANALYSIS

3.1. *Data Reduction*

Details of the data reduction procedure are given in Paper II. Images were downloaded from the STScI data archive using the "On the Fly Reprocessing" option, which processes the images with the task CALACS as described in the ACS Data Handbook (Pavlovsky et al. 2004). CALACS performs bias and dark subtraction, flat fielding, and overscan removal. Rotation and shifts between the five images of each galaxy were calculated by matching coordinates for a list of objects in common. Rotations were found to be negligible in all cases, while shifts of up to 0.2 pixels were measured and applied to bring the frames into alignment. Images taken with the same filter were combined, rejecting cosmic rays in the process, using PYRAF's task MULTIDRIZZLE. Distortion corrected images were also generated by MULTIDRIZZLE using a Gaussian kernel: although a Lanczos3 kernel is preferable for some applications (such as the SBF analysis, since it reduces the correlation between output pixels), a Gaussian kernel is more effective in repairing bad pixels, and therefore more suitable for the analysis of the morphology and surface brightness profiles presented here (Paper II). The final, combined and geometrically corrected images have size 4256×4256 pixels, with a pixel scale of 0″.049. Because of geometric distortion, thin wedges along the sides of the final image, as well as the 2″.5 gap separating the WF1 and WF2 chips, are not illuminated (e.g., see Figure 1). The resulting field of view is approximately 202″× 202″ in the shape of a rhomboid.

As described in Paper II, background estimates for the program galaxies were obtained directly from the processed images as the mode of the counts measured in two 5″ wide, 186″ long strips along the top and bottom (in the CCD coordinate frame) edge of each field. This procedure is sound only if the galaxies do not fill the field of view (FOV) of the detector, a condition which is not satisfied by the brightest ten galaxies (Figure 2 of Paper II). For these, the background in each filter was estimated from the relation, which is followed quite accurately by the fainter 90% of the sample, between background count rates and the angle Φ_{Sun} from the Sun to HST's V1 axis at the time of the observations (Figure 3 of Paper II). We note that background estimates can be slightly biased for galaxies which lie close to brighter companions, in particular VCC 1192 (NGC 4467) and VCC 1199, both of which project less than 5′ from VCC 1226 (M49).

Images for the brightest two galaxies in the sample are shown in Figure 1; images of all galaxies can be found on the ACSVCS website (http://www.cadc.hia.nrc.gc.ca/community/ACSVCS/). All images are corrected for geometric distortion and have been background subtracted (see Figures 2 and 3 of Paper II); the orientation differs from galaxy to galaxy (but is kept the same for all figures pertaining to the same galaxy), and is shown by the arrows in the upper left panel. The upper left panel in the Figure shows the entire ACS FOV. The bottom left panel shows a contour plot, drawn at the same levels given in the caption. Finally, the panels on the right-hand side show a zoom around the galaxy center (top panel), chosen to highlight particularly interesting features, and a ratio image (bottom panel), produced by dividing the g and $z-$band background subtracted images.

3.2. *Recovery of the Isophotal Parameters*

The IRAF task ELLIPSE was used to measure isophotal parameters for each of the 100 ACSVCS galaxies, in both filters. ELLIPSE adopts the methodology described in Jedrzejewski (1987): for each semi-major axis length, the intensity $I(\phi)$ is azimuthally sampled along an elliptical path described by an initial guess for the isophote's center (X, Y), ellipticity (ϵ), and semi-major axis position angle (θ). $I(\phi)$ is expanded into a Fourier series as:

$$I(\phi) = I_0 + \sum_k [A_k \sin(k\phi) + B_k \cos(k\phi)]. \qquad (1)$$

The best fitting set of parameters X, Y, ϵ, θ are those that minimize the sum of the squares of the residuals between the data and the ellipse when the expansion is truncated to the first two moments (which completely describe an ellipse). Higher order moments ($k \geq 3$) define deviations of the isophotes from ellipses. In practice, moments beyond the fourth cannot be measured accurately; third and fourth-order moments are calculated from the equation above by fixing the first and second-order moments to their best-fit values. The third-order moments (A_3 and B_3) represent isophotes with three-fold deviations from ellipses (e.g., egg-shaped or heart-shaped) while the fourth-order moments (A_4 and B_4) represent four-fold deviations. Rhomboidal or diamond-shaped isophotes translate into a non-zero A_4. For galaxies which are not distorted by interactions, B_4 is the most meaningful moment: a positive B_4 indicates "disky" isophotes (i.e., with semi-major axis $B_4 \times 100$ percent longer than the best fitting ellipse), while a negative B_4 indicates "boxy" isophotes (i.e., with semi-major axis $B_4 \times 100$ percent shorter than the best fitting ellipse; Jedrzejewski 1987).

When running ELLIPSE on the program galaxies, we adopted the following guidelines. To avoid having the isophotal solutions affected by bright globular clusters, foreground stars, or bad pixels, points deviating by more than three times the standard deviation of the mean intensity along each trial isophote were excluded from the fit. Furthermore, any bright galaxy in the FOV, any hot or dead pixel flagged during the drizzling process, as well as any area affected by dust (see below) were masked. The semi-major axis was increased logarithmically, i.e., each isophote was calculated at a semi-major axis 10% longer than that of the isophote preceding it. In general, all parameters were allowed to vary freely, although in a few specific cases (see below), it was found necessary to fix one or more of the parameters to achieve convergence. The isophotal center was not allowed to wander by more than 2 pixels between consecutive isophotes; in practice, when X and Y were allowed to vary, the center was found to be stable. The fit was terminated when less than 50% of the fitted ellipse resides within the CCD boundaries; in practice, ELLIPSE fails to converge well before this condition is met, since usually the small radial gradient in the surface brightness profile which characterizes the outer regions prevents convergence to be reached. When this happens, the surface brightness profile at larger radii was recovered by running ELLIPSE with θ, ϵ and isophotal center fixed to the mean values calculated for the outermost five fitted isophotes (which span a factor $(1.1)^4 = 1.46$ in semi-major axis length).

It is important to stress that the procedure outlined above is designed for predominantly elliptical isophotes. It will fail to converge on isophotes which display large deviation from ellipses: in such cases convergence can be achieved only by fixing the value of one or more parameters (in what follows these cases will be clearly identified). We therefore caution the reader that azimuthally averaged parameters for edge-on disk systems (e.g. VCC 2095, VCC 1125) or systems with strong bars (e.g. VCC759, VCC 654) might be uncertain.

Dust obscuration was dealt with in the following manner. Galaxies affected by dust were identified visually by inspecting both the residual images obtained by subtracting from the $g-$band image a smooth model galaxy described by the same isophotal parameters as those derived for the original image; and the color image produced as the ratio of the background-subtracted F475W and F850LP frames. As discussed in Paper I, the longer baseline afforded by the F475W-F850LP filter combination, when compared to the more commonly used F555W−F814W ($V-I$) color, results in a 50% increase in the sensitivity to dust obscuration. Based on the $g-z$ color maps and $g-$band residual maps, dust is firmly detected in 16 galaxies, and likely present in two additional objects (Table 2). Under the simplifying assumption that the dust responsible for the obscuration is in the galaxy's foreground (i.e., the "screen approximation"), at each pixel location (x, y), the absorption in the $g-$band is given by:

$$A(x,y)_g = -\frac{2.5}{A_z/A_g - 1} \times$$
$$\times \left[\log \frac{I(x,y)_{out,z}}{I(x,y)_{out,g}} - \log \frac{I(x,y)_{in,z}}{I(x,y)_{in,g}} \right], \qquad (2)$$

where I_{in} and I_{out} are the intrinsic (unextincted) and emerging (extincted) flux respectively; and A_g and A_z are the absorption (in magnitudes) in the g and $z-$band respectively. Following Cardelli, Clayton & Mathis (1989), and assuming the spectral energy distribution of a G2 star, $A_g = 3.634E(B-V)$ and $A_z = 1.485E(B-V)$, therefore $A_g/A_z = 2.447$. It follows that A_g (and therefore A_z) can be calculated if $I_{in,z}/I_{in,g}$ (i.e., the intrinsic galaxy color) is known. This is estimated by linearly interpolating across the dust affected area (or extrapolating, if the dust affects the center) the 1-D azimuthally averaged values of $I_{out,z}/I_{out,g}$ measured in the dust-free regions immediately surrounding it. A pixel is then flagged as affected by dust if 1) $A(x,y)_g$ is positive; 2) $A(x,y)_g$ is larger than the local standard deviation in the dust extinction map, and 3) if more than two contiguous pixels are affected. The last two conditions are necessary to avoid flagging noise spikes. In a typical ACSVCS galaxy, this methodology is sensitive to $g-$band absorptions A_g of 0.01−0.04 magnitudes or larger within the innermost $1''$. The case is significantly less favorable for galaxies with extremely low central surface brightness (e.g., VCC 9, VCC 1857), for which A_g would have to be larger than a few tenths of magnitudes for dust to be detected.

Because the dust is likely distributed throughout the body of the galaxy, rather than in the foreground, the extinction calculated as in equation (2) represents a firm lower limit to the true extinction. If the dust is distributed in a thin sheet in the galaxy mid-plane, for instance, the extinction increases as

$$A(x,y)_{mid-plane} =$$
$$= -2.5 \log \left[2 \times \left(10^{-0.4 A(x,y)_{foreground}} - 0.5 \right) \right], \qquad (3)$$

where $A(x,y)_{foreground}$ is given by equation (2).

Knowledge of $A(x, y)$ allows the recovery of the intrinsic fluxes, simply by multiplying the original images by an "extinction image" equal to $10^{-0.4A(x,y)}$. For most galaxies, this procedure generates smooth, dust-free images, but fails spectacularly in a few cases in which the unextincted color within the dust region is not well represented by the color extrapolated from the surrounding areas, as is the case when star formation is on-going within the dust patches. A thorough discussion of these issues will be presented in a future contribution, where dust masses will also be discussed.

Areas affected by dust were masked when running ELLIPSE. When the dust affects less than 50% of the pixels along individual isophotes (which is sometimes the case when the dust is distributed in thin filaments or small patches), a full isophotal solution can still be recovered in the dust affected areas. For galaxies where more than 50% of an individual isophote is affected by dust (for instance in the presence of dust disks), ELLIPSE was run on the image corrected for dust as described above.

The complete results of the ELLIPSE fitting for the brightest two galaxies are shown in Figure 2 for both filters. Plots showing the results for all other galaxies can be found on the ACSVCS website (http://www.cadc.hia.nrc.gc.ca/community/ACSVCS/). Surface brightness μ, ellipticity ϵ, position angle θ (measured in degrees from North to East) of the major axis and deviation of the isophotes from pure ellipses, as described by the A3, A4, B3 and B4 coefficients (equation 1), are plotted as a function of the 'geometric mean' radius r_{geo}. This is defined as $a \times \sqrt{1-\epsilon(a)}$, a being the radius measured along the isophotal semi-major axis. The data are plotted up to the geometric mean radius at which the surface brightness falls below 10% of the sky surface brightness, shown by the two short horizontal lines (the upper in the $z-$band and the lower in the $g-$band) in the upper left panel of each figure. Measurements in the g and $z-$band are plotted using open and closed circles, respectively. A horizontal solid bar in the upper left panel marks the region within which the isophotal parameters are derived from images corrected for dust, using the procedure detailed above. Isophotal shapes cannot be reliably recovered from the corrected images, and therefore the A3, A4, B3 and B4 coefficients are not plotted within this range. These coefficients are also not plotted when the isophotal fit is carried out by fixing the ellipticity and position angle as described above (these regions are identified in the Figures by horizontal open bars).

The transformation to the AB photometric system was performed as described in Paper II:

$$g_{AB} = -2.5 \log f(F475W) + 26.068 \quad (4)$$

$$z_{AB} = -2.5 \log f(F850LP) + 24.862, \quad (5)$$

where $f(F475W)$ and $f(F850W)$ refer to the integrated fluxes in units of electrons/second (Sirianni et al. 2005). Note that the surface brightness profile and color profile shown in Figure 2 are not corrected for foreground extinction. In the following discussion, it will be made clear whether correction for foreground extinction is performed; in such case, we adopt the differential $E(B-V)$ reddening values listed in Table 1 (from Schlegel et al. 1998), and the absorption coefficients listed immediately following equation 2.

The mean ellipticity, position angle and B4 coefficients recovered by ELLIPSE in the g and $z-$band are compared in Figure 3. The means are calculated between $1''$ (thus excluding a possible nuclear component) and one effective radius r_e (estimated as described in the next section), excluding areas affected by dust. The parameters recovered in the two bands compare favorably, attesting to the robustness of the fitting procedure. A comparison of central surface brightnesses (here and for the rest of the paper, central surface brightnesses are measured at $0''.049$), corrected for foreground extinction as described above, is also shown in the Figure. The solid line represents a $g-z$ color of 1.0; the tendency of brighter galaxies to be redder than fainter ones is real and will be discussed in §5.5.

Tables containing the results of the isophotal analysis for each galaxy will be made available electronically on the ACSVCS website: http://www.cadc.hia.nrc.gc.ca/community/ACSVCS/.

A Background Check for the Brightest Galaxies

As mentioned earlier, background determination for the ten brightest galaxies is particularly challenging since these galaxies completely fill the ACS/WFC FOV. A comparison of our measured profile with wide-field $B-$band surface brightness profiles available from the literature for nine of the ten brightest galaxies (Caon et al. 1990, 1994; Michard 1985; no attempt to compare profiles for VCC 1535 (NGC 4526) was made, because of the severe dust obscuration in this galaxy) shows generally excellent agreement. In a few cases, however, some small discrepancies exist at large radii ($r > 50''-100''$). To avoid biases associated with an incorrect background determination, as well as to increase the radial range of the data, the ACS g and z surface brightness profiles for these galaxies were combined with the ground-based $B-$band profiles. To do so, all three profiles were first fit with spline polynomials, and the mean $B-g$ and $B-z$ colors over the range $10''$ to $15''$ were determined. Constant offsets were then applied to the $B-$band profiles, to create pseudo g and z profiles; the fixed color offset seems warranted given that these galaxies show little or no evidence for strong radial color gradients within $\sim 0.5 r_e$. The final composite g and z profiles for each galaxy then consist of the original ACS data inside $30''$, and the transformed B-band profiles outside of this radius. Figure 4 shows the final brightness profiles for the nine galaxies. The fitted curve in each case represents the best-fit Sérsic or core-Sérsic models, described in §3.3.

3.3. *Parametrization of the Surface Brightness Profile*

Galaxy Profiles

We opt to fit the surface brightness profiles of the ACSVCS galaxies using both a Sérsic (1968; see Graham & Driver 2005 for a review) and a core-Sérsic model (as in Trujillo et al. 2004, see also Graham et al. 2003).

This section is designed to provide a brief exposition of other models available in the literature, in particular the "Nuker" model (Lauer et al. 1995), and to justify our choice.

The first HST studies of early-type galaxies (Crane et al. 1993; Ferrarese et al. 1994; Lauer et al. 1995) revealed surface brightness profiles which remained steep all the way to the smallest resolved radius, and could be closely approximated, in the inner regions, as power-laws, $I(r) \propto r^{\gamma}$. It was immediately apparent that in order to fit the HST profiles, one had to move beyond traditional parametrizations, such as exponential laws, de Vaucouleurs or Jaffe profiles (de Vaucouleurs 1948; Jaffe 1983). To reproduce the profiles of 14 bright elliptical galaxies in Virgo, observed with the (pre-refurbishment) Planetary Camera on board HST, Ferrarese et al. (1994) introduced a double power-law model described by four parameters: the inner and outer power-law slopes, the break radius which marks the transition between the two, and the intensity at the break radius. Examining a larger sample of galaxies, again observed with the pre-refurbished HST, Lauer et al. (1995) proposed a modified five parameter model (the "Nuker" model):

$$I(r) = I_b 2^{(\beta-\gamma)/\alpha} \left(\frac{r}{r_b}\right)^{-\gamma} \left[1+\left(\frac{r}{r_b}\right)^{\alpha}\right]^{(\gamma-\beta)/\alpha}. \quad (6)$$

Like the model of Ferrarese et al. (1994), the Nuker model is a blend of inner and outer power-laws (of slopes γ and β respectively), but has the added flexibility that the sharpness of the transition between the two, which occurs at the break radius r_b, can be controlled by the parameter α.

Graham et al. (2003) point out that since the Nuker model was specifically designed to describe only the innermost part of the profile (none of the profiles studied by Lauer et al. (1995) extends beyond $10''$, corresponding to ~ 800 pc at the distance of a typical galaxy in their sample), the model fails to reproduce the kpc-scale profiles of bulges and early-type galaxies, which deviate significantly from power-laws. More seriously, Graham et al. showed that the fitted Nuker parameters are sensitive to the extent of the radial range which is being fit; the degree of sensitivity is enough to compromise the physical interpretation of scaling relations based on such parameters. Finally, the integral of a Nuker model for $0 \leq r \leq \infty$ has no guarantee of converging, preventing the calculation of fundamental quantities such as effective radii and total magnitudes. To remedy these shortcomings, Graham et al. proposed a new model, composed of an outer Sérsic (1968) model, given by

$$I(r) = I_e \exp\left\{-b_n\left[\left(\frac{r}{r_e}\right)^{1/n} - 1\right]\right\}, \quad (7)$$

and an inner, power-law profile. The "core-Sérsic" model is therefore described as

$$I(r) = I'\left[1+\left(\frac{r_b}{r}\right)^{\alpha}\right]^{\gamma/\alpha} \times \exp\left[-b_n\left(\frac{r^{\alpha}+r_b^{\alpha}}{r_e^{\alpha}}\right)^{1/(\alpha n)}\right]. \quad (8)$$

where I' is related to the intensity, I_b, at the break radius r_b, as:

$$I' = I_b 2^{-\gamma/\alpha} \exp\left[b_n\left(2^{1/\alpha} r_b/r_e\right)^{1/n}\right]. \quad (9)$$

As in the Nuker model, r_b separates the inner power-law of logarithmic slope $-\gamma$ from the outer part of the profile, which in this case is described by a Sérsic model with effective radius r_e. The parameter α controls the sharpness of the transition between the inner and outer profile, with higher values corresponding to sharper transitions.

For a Sérsic model (or for the Sérsic component of a core-Sérsic model) with $1 \lesssim n \lesssim 10$, the effective radius r_e contains roughly half the integrated light of the model if $b_n \approx 1.992n - 0.3271$ (e.g., Capaccioli 1989; Caon et al. 1993; Graham & Driver 2005). Effectively, therefore, the number of free parameters in a Sérsic model is three, and in a core-Sérsic model six. The parameter n controls the overall shape of a Sérsic profile, with low n values producing curved profiles with logarithmic slopes which are shallow in the inner regions, and steep in the outer parts, while high n values produce extended profiles with less overall curvature (i.e. steep inner profiles and shallow outer profiles). For $n = 1$, a Sérsic model becomes a pure exponential, which is known to provide a good fit to the surface brightness profiles of some dwarf ellipticals, while for $n = 4$ it reduces to a classical de Vaucouleurs profile, which is a good approximation of the large-scale profiles of most bright ellipticals.

Trujillo et al. (2004) found it convenient to restrict the core-Sérsic model to the limit $\alpha \to \infty$, corresponding to an infinitely sharp transition between the Sérsic and power-law profiles at the break radius r_b:

$$I(r) = I_b\Big[(r_b/r)^{\gamma} u(r_b - r) + \\ + e^{b_n (r_b/r_e)^{1/n}} e^{-b_n (r/r_e)^{1/n}} u(r - r_b)\Big]; \quad (10)$$

where $u(x - z)$ is the Heaviside step function and all other parameters have the same meaning as in equation 8. For $\alpha \to \infty$, the number of free parameters in a core-Sérsic model is reduced from six to five, the same number of parameters as in the Nuker model. The intensities (and corresponding surface brightnesses) at the effective radius and at the break radius are related as:

$$I(r_e) = I_b \exp\left\{b_n\left[\left(\frac{r_b}{r_e}\right)^{1/n} - 1\right]\right\} \quad (11)$$

$$\mu_e = \mu_b - 2.5 b_n\left[\left(\frac{r_b}{r_e}\right)^{1/n} - 1\right]\log e. \quad (12)$$

The Sérsic and core-Sérsic models offer significant advantages compared to a Nuker model. First and foremost, they provide as good a description of the inner (100 pc scale) profiles, and a significantly better description when the profiles are extended to kpc-scale (Graham et al. 2003; Trujillo et al. 2004) . The Sérsic profile might have wide applicability: for instance, Merritt et al. (2005) find it to provide a good description of the mass profiles of ΛCDM halos. Unlike the case of the Nuker model, the parameters of a Sérsic and core-Sérsic model are robust against the extent of the radial range covered by the data (as long as the profile is sampled to radii of order r_e, i.e. large enough to allow to secure the curvature, Graham et al. 2003), and both models have finite integrals for $r \rightarrow \infty$. Finally, while the Nuker model was designed specifically as a phenomenological description of the observed projected profile, the Sérsic model has a simple physical interpretation: the roughly Boltzmann energy distribution corresponding to a Sérsic model is what is expected for systems which are well mixed as a consequence of violent relaxation or merging (Hjorth & Madsen 1995).

Based on these considerations, we opt to fit Sérsic and core-Sérsic models for the ACSVCS galaxies, with only one caveat. Many of the ACSVCS galaxies host distinct stellar nuclei at their centers (Paper VIII); in these cases, we allowed the inclusion of a nuclear component $I_{nuc}(r)$ in the models. This component was modeled as a King (1966) profile, which is described by a lowered isothermal distribution function of the form

$$f(E) = \exp(-\beta E) - 1, \tag{13}$$

where E is the energy. There is no analytic expression for the density corresponding to this distribution function, but the function $I_{nuc}(r)$ is readily obtained by integrating Poisson's equation. The King (1966) models are a one parameter family usually characterized by the concentration parameter $c = \log(r_t/r_c)$, where r_t is the tidal radius (i.e., the radius beyond which the density is zero) and r_c is the core radius (i.e., is the radius at which the density falls to about half its central value). In addition there are two scale parameters, the overall flux I_k and a spatial scale parameter, which we take to be the half-light radius r_h. The core and half-light radii are uniquely related, as their ratio is a function of c (e.g., McLaughlin et al. 2000). Thus, a King model adds three parameters, c, r_h, and I_k, to the fit of the surface brightness profiles of the ACSVCS galaxies.

Finally, we point out that in the interest of providing a homogeneous analysis, single Sérsic and core-Sérsic models (with the possible addition of a nuclear King model) were applied to all galaxies, including those showing evidence of multiple morphological components (e.g., stellar disks or bars, see §4.2). For these galaxies our approach is clearly unsatisfactory, and 2-D multi-component fits should be used instead for a rigorous analysis (e.g., Peng et al. 2002). *We therefore caution the reader against attaching too much weight to the profile fits for galaxies flagged as having multiple components; in the following discussion and figures, we will single out these galaxies to remind the reader of the limitation of our single 1-D model fits.*

Parameter fitting

We used a χ^2 minimization scheme to find the Sérsic and core-Sérsic (the latter with α set to infinity as in Trujillo et al. 2004) models which best fit the g and $z-$band intensity profiles of each galaxy. When the presence of a nucleus could be established, either based on the inspection of the images, or of the surface brightness profiles (see Paper VIII), a central King profile was also included in the fitting. Because of difficulties in estimating reliable errors in the intensity measurements, we adopt the usual procedure (e.g. Byun et al. 1996) of assigning equal fractional weights to all points in the profile (i.e. the amount by which the fitted profile is allowed to deviate at each point is proportional to the intensity at that point, see equation 14). The assumption of equal fractional weights is not unjustified given the way the profiles are constructed: the lower signal-to-noise ratio associated with the lower intensity of the profile at large radii is offset somewhat by the larger number of points sampled along the outer isophotes. As will be shown shortly, the profile fits under this assumption appear satisfactory, however, the lack of reliable error estimates in the intensity measurements prevents us from deriving meaningful errors in any of the fitted parameters. Finally, to avoid parameter mismatches due to differing initial conditions in the minimizations, the same starting inner radius was used when fitting the model in both filters.

All minimizations were carried out using the `Minuit` package in CERN's program library. The minimization procedure used consists of a Simplex minimization algorithm (Nelder & Mead 1965) followed by a variable metric method with inexact line search (MIGRAD) to refine the minima found by the Simplex algorithm. The models are convolved with the ACS point spread function (PSF) before being compared to the observed profile. PSFs for F850LP and F475W were obtained from images of the globular cluster 47Tuc, processed in exactly the same way as the ACSVCS images analyzed here. The PSF varies across the field of view and, at a fixed location, it depends on the star's centroid within the pixel; therefore to each galaxy we associate the PSF corresponding to the exact (sub-pixel) location of the galaxy center, measured as the light centroid within the inner 5 pixels (see Paper II and Paper VIII for additional details).

Although the best-fit parameters need not be the same in the two filters (e.g., the presence of color gradients would lead to a physically meaningful difference in a parameter related to the profile slope), to first order such differences should be small. However, external factors (for instance, the fact that it is sometimes possible to fit the surface brightness over a larger radial extent in one filter than in the other) might cause the minimization routine to converge to significantly different solutions in the two filters, a situation which is not physically justified.

To circumvent this problem, the fitting procedure was divided in two separate steps. First, we fit models *simultaneously* to the g and z profiles, $I(g)$ and $I(z)$. In doing so, initial guesses for the parameters are chosen based on the observed profiles; all parameters are constrained to be identical in both filters, with the exception of the intensity parameters, which are kept independent. For

instance, in the case of a Sérsic fit with a nuclear component included, we obtain the parameters by minimizing

$$\chi^2_{sim}[I_e(z), I_e(g), r_e, n, c, r_h, I_k(z), I_k(g)] =$$

$$= \sum_i \{[I_i(g) - S[r_i|I_e(g), r_e, n, c, r_h, I_k(g)]]/\epsilon I_i(g)\}^2$$

$$+ \sum_i \{[I_i(z) - S[r_i|I_e(z), r_e, n, c, r_h, I_k(z)]]/\epsilon I_i(z)\}^2, \quad (14)$$

where the sum is performed over all measured values of I, S is the PSF-convolved Sérsic plus King model profile and ϵ is an arbitrary factor (set to 0.001) chosen to effectively assign fractionally small (and equal) errors to all points. Second, the best parameters obtained from the simultaneous fit are used as initial guesses for individual fits to the g and z intensity profiles. In this case, for each band we obtain the best fit parameters by minimizing (using again the Sérsic fit with a nuclear component as an example):

$$\chi^2_{Sersic}(I_e, r_e, n, c, r_h, I_k) =$$

$$= \sum_i [(I_i - S(r_i|I_e, r_e, n, c, r_h, I_k)/\epsilon I_i]^2. \quad (15)$$

Because the nuclei of galaxies brighter than $B_T = 13.5$ mag are generally rather extended and do not clearly stand out against the bright galaxy background, fits for these galaxies were performed by constraining the Sérsic index n, the half-light radii and the concentration parameter of the King model to be the same in the two filters (see Paper VIII for further details).

The parameters of the Sérsic or core-Sérsic models best describing the surface brightness profiles of the ACSVCS galaxies are listed in Table 3. Global properties derived from these profiles are listed in Table 4, and will be discussed in more detail in later sections. The best fit Sérsic (blue) and core-Sérsic (red) profiles for the brightest four galaxies are shown over-plotted to the g and $z-$band surface brightness profiles in Figure 5. Fits for all other galaxies can be found on the ACSVCS website (http://www.cadc.hia.nrc.gc.ca/community/ACSVCS/). Solid curves show the final fits, including a nuclear component when present, while dashed and dotted curves show the individual galaxy and nuclear components respectively. Residuals are shown in the lower panels. With the best-fit parameters in hand, we calculated the total g and $z-$ band magnitudes and effective radii (defined as containing half of the total light of the galaxy[13]) by integrating the model to $r = \infty$[14].

[13] In the case of a core-Sérsic model, and with the definition of b_n given in the text, r_e in equations 8 and 10 represents the radius within which half of the total light of the outer Sérsic model, rather than of the complete model, is contained (see Trujillo et al. 2004). In this case, the r_e values in Tables 3 and 4 are not equal.

[14] We note that with this definition, the total magnitudes of galaxies which are tidally truncated might be overestimated.

The model profiles (before and after PSF convolution) will be made available on the project website. The results of the profile fitting will be discussed in §4.2. Before doing so, we will digress momentarily to describe, in broad strokes, the galaxies' morphologies (§4.1).

4. RESULTS

4.1. *Galaxy Morphologies*

The ACSVCS galaxies display a staggering variety of morphologies. A detailed description of the morphological features detected in each galaxy is given in the Appendix, while Table 2 summarizes the incidence of dust, stellar disks, bars, stellar nuclei and other morphological anomalies. The properties of the stellar nuclei are the subject of Paper VIII, and will be discussed only briefly here.

Dust Features

Dust is firmly detected in 16 galaxies, and likely present in two additional systems (Table 2). Forty-two percent (11 out of 26) galaxies brighter than $B_T = 12.15$ mag (which, as mentioned earlier, form a magnitude-limited sample), have dust features. This is consistent with previous studies which targeted preferentially bright elliptical galaxies (e.g., Goudfrooij et al. 1994; van Dokkum & Franx 1994; de Koff et al. 2000; Tran et al. 2001). Dust is also detected in seven of the galaxies fainter than $B_T = 12.15$. Although only one of these (VCC 1779) is classified in the VCC as a dwarf (giving a nominal detection rate of $1/35 = 3\%$), strong selection effects are at play, since the generally low surface brightness of dwarf galaxies prevents us from detecting low levels of dust obscuration. Three bright early-type Virgo galaxies excluded from the ACSVCS are known to have dust based on ground based observations (VCC 2066 = NGC 4694, VCC 801 = NGC 4383 and VCC 758 = NGC 4370; Sandage & Bedke 1994; Caon, Capaccioli & D'Onofrio 1994). A firm lower limit on the incidence of dust in the 65 E+S0 galaxies in the ACSVCS, plus VCC 2066, VCC 801 and VCC 758 is therefore $(17 + 3)/(65 + 3) = 29\%$.

Dust features can be broadly grouped in four categories:

C1. Faint wisps and patches, often crossing the center (VCC 1226=M49, VCC 1316=M87, VCC 881=M86, VCC 1632=M89, VCC 355=NGC 4262, VCC 1619=NGC 4550, VCC 1779 and, possibly, VCC 1422, VCC 798=M85);

C2. Large, kiloparsec-scale, high extinction irregular dust lanes (VCC 763=M84, VCC 571);

C3. Large (over 700 pc, or $8''.7$, across), patchy dust disks (VCC 1535=NGC 4526, VCC 1154=NGC 4459, VCC 1030=NGC 4435, VCC 1250=NGC 4476);

C4. Small (less than 300 pc, or $3''.7$ across), thin, featureless, regular dust disks (VCC 759=NGC 4371, VCC 685=NGC 4350, VCC 1327=NGC 4486A).

Evidence of recent/on-going star formation, in the form of bright blue associations, is always associated with the large, clumpy dust disks (category 3). Star formation within cold, dusty gas disks has been discussed by Tan & Blackman (2005); indeed all three of the smaller, regular disks (category 4) are seen in conjunction with regular, smooth blue stellar disks/rings, perhaps suggesting that these disks might represent a later evolutionary phase of the larger, clumpier dust disks. Star formation is not seen in connection with the irregular dust lanes, which may therefore represent an earlier evolutionary phase of the large dust disks, when the dust has not yet had the time to settle into a stable configuration and star formation has yet to begin. This would suggest an evolutionary scenario in which dust features evolve from category C2 to C4 through C3. Since the unsettled, irregular morphology of the dust lanes (C2) implies an external origin (Goudfrooij et al. 1994l; van Dokkum & Franx 1995; de Koff et al. 2000; Tran et al. 2001; Temi et al. 2004), this would argue for an external origin even for the regular, smaller dust disks (C4). Alternatively, the nuclear dust disks might be the result of the bar-induced accumulation of gas and dust towards the center, and might be the precursors of the blue, nuclear stellar disks seen in several of the ACSVCS galaxies (§4.1.2). The connection between the disks/lanes, and the thinner, less massive, more tenuous dust filaments, none of which is accompanied by star formation, is not immediately apparent. These issues will be discussed in more detail in a future contribution.

Large-scale, highly organized dust disks are not found in the faintest half of the sample; had they been present in the galaxies omitted from the ACSVCS, they would certainly have been detected based on ground based images. This fact aside, there appears to be no correlation between either the amount of dust obscuration, or the morphology of the dust features, and the magnitude or morphology of the host galaxy. For instance, VCC 1226 (M49) and VCC 1316 (M87, Figure 1), the two brightest galaxies in Virgo, show only faint dust wisps and patches, while VCC 1250 (NGC 4476), which is 3.6 mag fainter, sports a clumpy, nuclear dust disk 1.8 kpc ($\sim 22''$) across. VCC 571, 1.8 magnitudes fainter still, shows only thin dust filaments emanating from the center. The most massive dust features, well organized disks ~ 1.4 kpc ($17''.5$) across, are seen in VCC 1535 (NGC 4526) and VCC 1154 (NGC 4459), two bright galaxies of similar magnitude. These disks are remarkably similar in size, extinction, and overall structure. However, VCC 1154 (NGC 4459) shows very regular isophotes, while the isophotes of VCC 1535 (NGC 4526) are highly disturbed: the galaxy becomes extremely boxy at a distance between $10''$ and $20''$ from the center, switches to a diamond shape further out, and becomes very disky at a distance of $70''$. VCC 759 (NGC 4371) and VCC 355 (NGC 4262), two of the galaxies which host a dominant stellar bar, show a small regular dust disk and thin dust filaments respectively, however, no dust is detected in the barred galaxies VCC 2092 (NGC 4754) and VCC 654 (NGC 4340).

Estimating the incidence and strength of disk structures in early-type galaxies is a complex problem owing to the effects of inclination on the measured surface brightness profile, ellipticity and isophotal shape. Rix & White (1990) estimate that for inclinations angles i (with i measured between the plane of the disk and the plane of the sky, so that $i = 90^\circ$ for edge-on systems) larger (i.e., more edge on disks) than $\sim 55^\circ$, a disk containing as little as 10% of the light of the bulge component would cause the isophotes to depart from a pure elliptical shape. At smaller inclinations (more face-on disks), the projected isophotes of even luminous disks are almost perfectly elliptical, and disks can be identified only through the perturbations they impart on the surface brightness profile of the accompanying bulge. Unfortunately, such deviations can be recognized only if the intrinsic profile of the bulge is known *a priori*, an invalid hypothesis given the considerable scatter in the shapes of the profiles displayed by galaxies of comparable magnitude (§4.2). It follows that a morphological analysis would not detect the vast majority of bulge-embedded disks with $i \lesssim 55^\circ$.

Keeping these biases in mind, disks are detected in two basic varieties within the ACSVCS sample: fully embedded, 100-pc scale inner disks hosted in galaxies that are bulge-dominated on large-scales; and kpc-scale outer disks that dominate the light distribution in the galaxy outskirts. In some cases (e.g., VCC 1692=NGC 4570, VCC 685=NGC 4350, see Table 2), the two classes overlap, i.e., a "nested-disk" structure composed of two morphologically distinct inner and outer disks is detected − similar morphologies have been reported in the past by, among others, van den Bosch et al. (1994), Lauer et al. (1995), Scorza et al. (1998) and Erwin et al. (2003). Because the disks are almost always close to edge-on, they impart a characteristic signature to the surface brightness profile. For instance, Figure 6 shows a cut through the photometric major axis of VCC 1692. At large radii, the profile is dominated by the outer, exponential, disk. In the inner region, a blue stellar ring with radius 150 pc, but less than 7 pc wide, surrounds the nucleus; the outer boundary of the ring produces a clear discontinuity in the profile at $1''.8$ from the center. The structure of the inner region of VCC 1692 has been addressed by Van den Bosch & Emsellem (1998) in the context of secular bar evolution.

Outer disks have been detected in 16 of the ACSVCS galaxies; in two additional cases (VCC 798=M85 and VCC 1231=NGC 4473, the 5th and 11th ranked early-type members of Virgo) the presence of a moderately inclined disk is suggested by the positive B4 coefficients. In VCC 1938 (NGC 4638) the outer disk, which is seen edge-on, is rather abruptly truncated approximately 300 pc ($4''.0$) from the center; within this region is nested a boxy, elongated bulge. Figure 7 shows a cut through the photometric major axis for VCC 1938, clearly showing the inner truncation of the disk. In addition, the North-West side of the disk (shown on the left side of the profile, left panel) shows a discontinuity at 1.1 kpc ($14''$) from the center. This discontinuity, which is not immediately apparent in the South-East side of the profile, might correspond to density fluctuations within the disk, as could result from spiral structure. "Inner Truncated Disks" (ITD), such as the one observed in VCC 1938,

have surfaced regularly in the literature since Freeman's (1970) observation that in a significant number of spiral galaxies the inward extrapolation of the exponential surface brightness profile of the outer disk would exceed the observed central surface brightness (Freeman's Type II disks). The incidence of ITDs, detected on the basis of a 1-D or 2-D bulge/disk decomposition of the surface brightness profiles, is of order 25% in spiral galaxies (Baggett, Baggett & Anderson 1998, 1996; Anderson, Baggett & Baggett 2004), and as high as 65% in S0 galaxies (Seifert & Scorza 1996). The general consensus is that ITDs are the result of secular evolution induced when the outer disk becomes bar unstable (Baggett et al. 1996; Emsellem et al. 1996; van den Bosch & Emsellem 1998; Scorza & van den Bosch 1998); indeed, in the case of VCC 1938, an edge-on bar could be disguised as the boxy bulge detected within the inner cutoff of the edge-on outer ITD. In addition, the bar-driven influx of (presumably enriched) gas is identified as the mechanism by which the inner disks seen in nested-disk structures are built (Erwin 2004; Emsellem et al. 1996; Scorza et al. 1998; van den Bosch & Emsellem 1998; Scorza & van den Bosch 1998). The large line strength values detected at the centers of S0 galaxies support this hypothesis (Fisher, Franx & Illingworth 1996; van den Bosch & Emsellem 1998); in VCC 1125 (NGC 4452) the resolved nucleus and the inner stellar disk are bluer than the surrounding bulge, indicating that both might have formed at a later time by accumulation of gas towards the center. The small, nuclear dust disks surrounded by blue stellar disks and rings seen in VCC 685 (NGC 4350) and VCC 1327 (NGC 4486A) could represent earlier stages of the inner, blue stellar disks, when gas and dust driven towards the center by the bar has not yet been completely converted into stars.

The bar-driven accumulation of mass in the center, whether it results in the formation of a disk, bulge or the feeding of a central supermassive black hole, would ultimately have a stabilizing influence through the creating of a strong inner Lindblad resonance, thereby leading to dissolution of the bar (e.g., Norman, Sellwood & Hasan 1996). In the next section, we will argue that VCC 1537 (NGC 4528), in which a bar structure is clearly detected, could represent a transition stage in which an ITD, seen at moderate inclinations, is currently being formed.

VCC 2095 (NGC 4762) and VCC 1125 (NGC 4452) display a morphology intermediate between IDTs and nested-disks. In both galaxies, the edge-on outer disk continues uninterrupted to the center of the galaxy, but its thickness appears variable, giving the impression of a "nested-disk" structure (Figure 8). Cuts along the major axis (Figure 9) show multiple "humps"; a detailed kinematical study is necessary to decide whether the structure is due to nested-disks, a single, warped disk, or a disk plus a "lens" (Freeman 1975; Kormendy 1984). Either a lens or an ITD could be responsible for the morphology of VCC 575 (NGC 4318, left panel of Figure 9), which shows a bright bulge confined within a sharply bounded, low surface brightness region, about $7''$ across (280 pc radius), beyond which a disky component (positive B4, higher ellipticity) sets in.

Finally, we mention in passing the admittedly speculative possibility that the inner "dip" detected in the surface brightness profile of VCC 881 (Figure 10; Carollo et al. 1997; Lauer et al. 2002; Lauer et al. 2005) might be associated with the inner truncation of an outer, almost face-on disk, which would otherwise remain undetected based on the isophotal analysis. VCC881 (NGC 4406) is kinematically peculiar in that the main galaxy exhibits minor axis rotation, while the core is kinematically decoupled (Bender 1988; Wagner et al. 1988). Whether secular evolution of a (now dissolved) bar formed within a disk structure could explain the observed kinematics is a possibility worth investigating; based on its stellar velocity dispersion, the galaxy hosts a $\sim 4 \times 10^8$ $M_\odot$ supermassive black hole at its center (Ferrarese & Ford 2005), the (bar-induced?) growth of which could be partly responsible for the bar dissolution.

Stellar Bars and Rings

Stellar bars have been detected in a few early-type galaxies (Scorza et al. 1998; Emsellem, Goudfrooij & Ferruit 2003; Busarello et al. 1996; Erwin 2004); and indeed they might be connected with the truncated and nested-disk structures discussed in the previous section. Unfortunately, investigating the extent of such a connection is complicated by the fact that bars are most easily detected in face-on configurations which are least conducive to disk detection.

Stellar bars are seen in at least seven, and perhaps as many as nine of the ACSVCS galaxies (Table 2); although the presence of a disk is not immediately apparent in any of them (as noted above, observational biases work against the detection of a disk in these objects), their profiles are not dissimilar from those displayed by galaxies with large-scale stellar disks. With two exceptions (VCC 1537=NGC 4528 and VCC 654=NGC 4340), the bars are, however, of significantly larger size (over 1 kpc) than, and are therefore likely unrelated to, the ones needed to explain the ITDs in VCC 1938 (NGC 4638) and, possibly, VCC 575 (NGC 4318).

VCC 1537 (NGC 4528), however, is a prime candidate for a transition object between regular S0s and ITDs. The isophotal parameters show a dramatic change in ellipticity, A4 and B4 coefficients (and, to a lesser extent, major axis position angle), between 480 and 960 pc ($6''$ and $12''$); inspection of the images clearly reveals the presence of a bar, misaligned by $\sim 60°$ relative to the major axis of the main body of the galaxy. The surface brightness profile outside 470 pc from the center is roughly exponential (Figure 11), the ellipticity is larger compared to the value measured in the inner region, and the B4 coefficient is slightly positive, indicating the presence of a large-scale disk. Immediately inside 470 pc of the center, the surface brightness falls below the extrapolation of the exponential describing the large-scale profile. This morphology is consistent with the presence of an ITD, inclined approximately 60° to the plane of the sky and truncated at an inner radius of 470 pc, corresponding to the outer Lindblad resonance within which the bar is contained.

The other bars detected in the ACSVCS galaxies vary widely in terms of strength, size and the structure of the surrounding region. Beside VCC 1537 (NGC 4528), the most spectacular cases are VCC 654 (NGC 4340) and

VCC 759 (NGC 4371). VCC 654 is listed as a double-barred galaxy in Erwin (2004). The outer (primary) bar extends for 5.5 kpc (68″), displaying sharp edges where the bar meets an outer stellar ring. The latter has major axis approaching 10 kpc (125″), and minor axis misaligned, by approximately 17°, with respect to the bar. The inner (secondary) bar extends for 0.6 kpc (8″), and is responsible for the "stretching" of the isophotes and the dramatic change in the major axis position angle registered beyond a few arcsec. The inner bar is bounded by a nuclear stellar ring, extending for 1.5 kpc (19″) along the major axis. Nuclear and outer rings appear aligned, and the inner bar is roughly aligned with the minor axis of the nuclear ring. Inner and outer bars, however, are slightly misaligned, in other words the outer bar does not appear to be a simple extension of the inner bar.

Like VCC 654, VCC 759 displays a large stellar ring, 13 kpc (160″) across along the major axis, and a large scale bar. The inner region is characterized by at least two kpc-scale stellar rings; however there appears to be no evidence for an inner bar. With VCC 355 (NGC 4262), VCC 759 is one of two barred galaxies to host dust: a small, 120 pc (1.″5), dust disk surrounds the center of the galaxy. Dust disk and stellar rings appear to be concentric, coaxial, and share the same ellipticity. In VCC 2092 (NGC 4754) and VCC 355 only the bar, but no ring, is visible. Weaker bars are likely present in VCC 778 (NGC 4377) and VCC 1883 (NGC 4612); in both cases, the bar is misaligned with respect to the main body of the galaxy. In two more galaxies (VCC 369=NGC 4267, and VCC 1283=NGC 4479), although a bar is not immediately apparent by a simple visual inspection of the images, its presence is inferred from the rapid changes in ellipticity, higher order coefficients and, in particular, major axis position angle exhibited by the isophotes. These are characteristics of the barred galaxies described above (see also Erwin 2004); in particular a radial variation in position angle is unlikely the result of an edge-on disk.

Other Morphological Peculiarities

In the next few paragraphs, we will briefly touch upon a few additional galaxies that display interesting morphologies.

Four of the ACSVCS galaxies project close to bright companions. VCC 1327 and VCC 1297 (NGC 4486A and NGC 4486B respectively) project 7.′5 and 7.′3 respectively from M87, while VCC 1192 (NGC 4469) and VCC 1199 project 4.′2 and 4.′5 respectively from M49. For all except VCC 1327 (NGC 4486A) there is clear evidence that the galaxies have been tidally stripped. Indeed, NGC 4486B has long been held as one of the textbook cases of compact ellipticals which result from tidal truncation (Rood 1965; Faber 1973); the surface brightness profile declines rapidly beyond a few arcseconds. With VCC 1192 and VCC 1199, and compared to galaxies of similar B_T, NGC 4486B has brighter central surface brightness, smaller effective radius, and a surface brightness profiles which is best fit by a larger Sérsic index n (see §3.3.1, §4.2 and Table 3). The case is not as clear-cut for VCC 1327: the surface brightness profile, effective radius and central surface brightness of this galaxy are consistent with those of galaxies of similar magnitude.

We confirm the existence of a face-on spiral pattern in VCC 856 (IC 3328), a galaxy formally classified as a dE1,N. The pattern was first noticed by Jerjen et al. (2000). Since then, evidence of spiral patterns or disk/bar structures have been found in a handful of Virgo, Fornax and Coma dwarf ellipticals (Jerjen et al. 2001; De Rijcke et al. 2003; Graham et al. 2003; Barazza et al. 2002); these objects have been interpreted as late-type galaxies in the process of being transformed to an early-type morphology by harassment within the cluster environment. In addition to VCC 856, for which the pattern is clearly visible both in the g and $z-$band images, tantalizing evidence for spiral structure is found in VCC 1695 (IC 3586, classified as dS0:) and VCC 1199 (classified as E2). Although the structure is not immediately apparent from inspection of the single images, it does appear in the residual images, obtained by subtracting the best isophotal model from the original images. The $g-$band residual images of both galaxies can be found on the ACSVCS webpage (http://www.cadc.hia.nrc.gc.ca/community/ACSVCS/). In the case of VCC 1199, which, as noted above, is a close companion of M49, it is possible that the spiral arms might have been triggered by the interaction between the two galaxies (Toomre 1969; Goldreich & Tremaine 1979)

Finally, four galaxies, VCC 21 (IC 3025), VCC 1779 (IC 3612), VCC 1499 (IC 3492), and VCC 1512, all classified as dS0 galaxies, should instead be reclassified as dwarf irregular/dwarf elliptical transition objects, based on the presence of loose associations of bright blue star clusters, and the irregular isophotal shapes.

4.2. *Surface Brightness Profiles*

Figure 12 shows representative profiles for six 'regular' (i.e., displaying elliptical, regular isophotes, and no obvious stellar disks or bars) galaxies in our survey, ordered from top to bottom according to their total $B-$band magnitude. The diversity in the light distribution is immediately apparent: the extent and slopes of the profiles differ greatly. In addition, some of the profiles are dominated by the presence of a nuclear component (Paper VIII). The profiles for all galaxies, to which the contribution of the nuclear component has been subtracted, are plotted in Figure 13 as a function of r/r_e, with r_e the effective radius. When plotted in this fashion, some common traits between the profiles start to become apparent: in general, as the galaxy becomes fainter, the curvature in the profiles becomes more pronounced and the profile's slope within $\sim 1''$decreases. The brightest ten or so galaxies deviate from this trend and seem to define a class of their own, with extended profiles which flatten towards the center in a manner which is uncharacteristic of the remaining galaxies in the sample. In the following we will quantify these statements in a more rigorous fashion, and discuss the implications in §5.

Sérsic or Core-Sérsic?

To justify the choice of parametrization of the surface brightness profile, for each galaxy we calculated the χ^2 of the best Sérsic and core-Sérsic models, following Equation (15). In an absolute statistical sense, such χ^2 values

are not easily interpretable since realistic error estimates in the surface brightness data are not simply quantifiable because of uncertainties in the sky values, fitting procedures, and, when applicable, correction for dust obscuration. However, comparing χ^2 values for different galaxies allows us to assess the *relative* goodness of fit for the two models. In what follows, we will assign to each galaxy the largest of the g and $z-$band χ^2 (calculated in a radial range which excludes the nuclear star cluster if present), and convert this into a reduced χ^2, χ^2_r, by dividing by the number of fitted data points minus the number of fitted parameters (three and five for the Sérsic and core-Sérsic models respectively).

Figure 14 plots χ^2_r of the best fit Sérsic model against the ratio of the χ^2_r of the best fit Sérsic and core-Sérsic models. The figure is divided in two panels: on the left, we plot all 'regular' galaxies, which appear to be well described by a single morphological component (nucleus not-withstanding), while on the right we plot all galaxies with multiple morphological components (e.g., bulge + stellar disks, bars or spiral structures). Several points are noteworthy:

1. The χ^2_r for a Sérsic model is never significantly lower than for a core-Sérsic model, which is not surprising since a core-Sérsic model can always be reduced to, and hence perform as well as, a pure Sérsic model by choosing the right combination of r_b and γ.

2. Although several of the galaxies with multiple morphological components (nucleus not-withstanding) are, somewhat surprisingly, reasonably well fit by a Sérsic, or core-Sérsic, model (i.e., χ^2_r (Sérsic) $\lesssim$ a few), a larger majority has high χ^2_r, compared to regular galaxies. This is of course due to the fact that the presence of morphologically distinct features creates irregularities in the 1-D profile which the models are not designed to reproduce. In all these cases, it seems sensible to choose the simpler Sérsic over the core-Sérsic model as a first-order description of the profile.

3. While for most regular galaxies a Sérsic fit provides a good description of the data, as demonstrated by the low value of the corresponding χ^2_r, there are a handful of exceptions. In particular, there are galaxies for which both Sérsic and core-Sérsic models perform equally "badly", i.e., the χ^2_r for the two models are large and similar [χ^2_r (Sérsic) $\gg 1$ and χ^2_r (Sérsic)/χ^2_r (core-Sérsic) ≤ 2]. For these cases, the simpler Sérsic model is again chosen over the core-Sérsic model.

4. For a few galaxies, a core-Sérsic model provides a significantly better description of the data than a Sérsic model. This is the case for eight of the 10 brightest Virgo galaxies (in the case of VCC 1535=NGC 4526, the profile is seriously contaminated by dust and a reliable fit cannot be carried out). Examples are VCC 1226 (M49), VCC 1978 (M60) and VCC 881 (M86): for all, the slope of the inner profile is shallower than the one given by a Sérsic model constrained by the profile at large radii. This result is robust against the extent of the radial range to which the model is fit; in particular it is not affected by the inclusion of the ground-based data in the surface brightness profile (§3.2.1). In the left-hand panel of Figure 14, these galaxies are plotted as red triangles and are all found in the right upper half of the diagram, i.e., χ^2_r (Sérsic) / χ^2_r (core-Sérsic) $\gtrsim 10$, and χ^2_r (Sérsic) > 200: their χ^2_r then supports the conclusion that a core-Sérsic model is preferable to a pure Sérsic model.

5. For two additional galaxies, a core-Sérsic fit also seems to provide a better description of the data than a Sérsic fit. These are VCC 1250 (NGC 4476) and VCC 1512. In the left panel of Figure 14, both galaxies (plotted again as red triangles) are found near χ^2_r(Sérsic)/χ^2_r (core-Sérsic) ~ 10 and χ^2_r (Sérsic) ~ 100, and in both cases a Sérsic model fails to reproduce the abrupt transition observed between the outer and inner profile. Nevertheless, the choice of a core-Sérsic model should be considered marginal: VCC 1250 harbors a $22''$ dust disk and a stellar nucleus; although the correction for dust extinction performs well (§3.2), both the effective radius and the break radius of the best fit core-Sérsic model are within the dust-affected area, therefore the fits should be interpreted with caution. VCC 1512 is best classified as a dwarf irregular/dwarf elliptical transition object, therefore its properties cannot be simply related to those of the early-type galaxies in the sample. For the three other dIrr/dE in the sample, VCC 21, VCC 1779 and VCC 1499, a core-Sérsic model is well suited at following the small gradient of the profile towards the center; however the difference between core-Sérsic and Sérsic fits is not as pronounced as in the case of VCC 1512.

In conclusion, the choice of a core-Sérsic model is amply justified only for the eight bright galaxies discussed in 4), and should be considered tentative for VCC 1250 (NGC 4476) and VCC 1512. Figure 15 shows a comparison of the best fit Sérsic index n, effective radius r_e, break radius r_b (for the galaxies best fit by a core-Sérsic model), and inner slope γ measured in the g and $z-$bands. In the case of the 90 galaxies best fit by a Sérsic profile, γ is defined as the logarithmic slope of the model profile at $0''.1$:

$$\gamma_{0.1} = -\frac{\mathrm{d}\log I}{\mathrm{d}\log r} = \frac{b_n}{n}\left[\frac{0.1}{r_e(\mathrm{arcsec})}\right]^{1/n}. \qquad (16)$$

Note that with this definition, γ is not affected by the presence of a nuclear component and represents the inner slope of the profile prior to PSF convolution. The consistency of the parameters recovered by the independent fits in the two bands testifies as to the robustness of the fitting procedure. Finally, g and $z-$band magnitudes are compared to B^0_T from the VCC in Figure 16. Notice that the g and $B-$band are similar but not identical, furthermore, the zero point uncertainty associated with the VCC $B-$band magnitudes is of order 0.25 mag (Binggeli et al. 1985). Both effects can lead to a small systematic

$g - B$ color difference. The tendency of fainter galaxies to be bluer than brighter ones is a known trend (§5.5).

4.3. *Scaling Relations*

The fact that the morphological and kinematical properties of elliptical galaxies, bulges, galaxy nuclei and disks are markedly different is the reflection of the clearly distinct physical mechanisms regulating the formation of these systems. Here we will focus on scaling relations involving only morphological parameters; the study of the fundamental plane and other relations including kinematical properties will be left to future papers.

Figure 17 presents a collection of correlations between fitted parameters in the g (plotted below the diagonal line running from the lower left to the upper right corner) and $z-$band (plotted above the same diagonal line). Along the diagonal are shown histograms for all of the parameters: g and $z-$band data are plotted using a solid and dashed line respectively; in both cases, the value of the parameter is plotted along the x-axis, and the number of galaxies on the y-axis (for which units are not shown). Some particularly relevant correlations, discussed in more detail below, are reproduced in Figure 18, where galaxies are color coded according to the parametrization of the surface brightness profile, and the presence/absence of multiple morphological components and/or a nucleus. The following points are worth noticing:

1. The central surface brightness μ_0 (panels *ae* and *ea* of Figure 17) correlates well with the total galactic magnitude. μ_0 is measured directly from the images as the intensity recorded at the central pixel, and therefore includes the contribution of a nuclear component, as well as PSF smearing. The basic trend, however, is unchanged if μ_0 is substituted with the surface brightness $\mu_{0.05}$ measured at $0''.049$ (1 pixel) from the model best fitting the galaxy surface brightness profile (equations 7 or 10), before PSF convolution and excluding a nuclear contribution, if present (Figure 18). The clear trend of central surface brightness becoming brighter with decreasing magnitude (increasing luminosity) is broken only by the brightest half a dozen galaxies, for which the trend is reversed. The brightest galaxies do not follow the trend defined by the rest of the sample even if to the measured μ_0 one substitutes the value obtained from the inner extrapolation of the Sérsic model best fitting the outer parts of the profile. Substituting μ_0 or $\mu_{0.05}$ with the surface brightness at one effective radius, μ_e, leads to a similar correlation but increases the scatter (panels *af* and *fa* of Figure 17, and Figure 18). This is due to the fact that, both for a Sérsic and core-Sérsic model, μ_e is related to $\mu_{0.05}$ through a term depending on r_e, and the latter shows larger scatter as a function of galaxy magnitude (see point 4, panels *ad* and *da* of Figures 17, and 18).

2. There appears to be a sharp upper limit to the value of the central surface brightness achieved by early-type galaxies, as is apparent from the histogram showing the distribution of μ_0 (panel *ee* of Figure 17). This cutoff occurs at $\mu_0 = 14.0$ mag ($\mu_{0.05} = 13.5$ mag) in the $g-$band, and $\mu_0 = 12.1$ mag ($\mu_{0.05} = 11.9$ mag) in the $z-$band[15]. The brightest galaxies in the sample fall below this upper cutoff.

3. The Sérsic index n (which, in the case of galaxies best fit by a core-Sérsic model, is equal to the index of the Sérsic model that best describes the outer profile) increases monotonically as the galaxies become brighter (panels *ac* and *ca* of Figure 17, and Figure 18). In particular, the shape of the outer profile for the brightest galaxies is consistent with that expected by simply extrapolating the trend defined by the fainter systems: in contrast with the claim of Prugniel & Simien (1997), there is no clear indication in our sample for a leveling off in the value of n at the bright end. Prugniel & Simien (1997), using Sérsic fits to ground-based data for galaxies with $-22 < M_B \leq -16$ mag, found $n \sim$ const ~ 4 for $M_B \leq -20$ mag. The constancy of n for the brightest galaxies is likely a bias introduced by the fact that these galaxies have cores which are shallower than expected based on a Sérsic fit to the outer parts: a Sérsic fit to the entire profile will therefore be forced to have larger curvature (lower n) than it would were the inner region to be excluded from the fit. Indeed, Sérsic fits to the ACSVCS data for the brightest galaxies produce values of n which are approximately constant and clustered around $n \sim 4$.

4. The effective radius r_e, which, with n and μ_0, is one of three independent parameter in a Sérsic fit, shows a weak correlation with M (panels *ad* and *da* of Figure 17, and Figure 18). The brightest galaxies ($M_B \lesssim -20.2$ mag) are distinct from the rest of the sample, producing a clearly bimodal distribution in the r_e histogram (panel *dd* of Figure 17). The mean effective radius for galaxies with $M_B \gtrsim -20.2$ mag is $13''.6 \pm 6''.6$ (1.1 ± 0.5 kpc), while for brighter galaxies r_e(mean) $= 169'' \pm 103''$ (13.5 ± 8.2 kpc) – an abrupt change in the trend of r_e *vs.* magnitude at $M_B \sim -20$ mag was also noted by Binggeli, Sandage & Tarenghi (1984, their Figure 7). Although the ACSVCS sample is complete for $M_B \leq -18.94$ mag, the bimodality observed in the r_e values is likely due to the small number of galaxies straddling the critical magnitude range $-20.5 < M_B < -20$; indeed a discontinuity in r_e was not noted by either Binggeli, Sandage & Tarenghi nor Graham & Guzman (2003), using larger samples of galaxies. We note that the large r_e values measured for the brightest galaxies are not an artifact of the choice of parametrization for the surface brightness profile: while forcing a Sérsic fit to the brightest galaxies (as done by Binggeli et al.) decreases r_e by 30% to 40% relative to the value obtained using a core-Sérsic fit (as a consequence of the bias described in point 3 above),

[15] It should be remembered that while μ_0 is measured directly from the images, $\mu_{0.05}$ is computed from the galaxy model before PSF convolution, therefore $\mu_{0.05}$ can be brighter than μ_0).

this is not enough to bring the brightest galaxies in agreement with the rest of the sample.

5. The logarithmic slope of the inner brightness profile, γ, becomes steeper as the galaxy luminosity increases (panels *ab* and *ba* of Figure 17, and Figure 18 – where γ is defined as the slope of the profile *underlying* a nuclear component, when present, and prior to PSF convolution, see equation 16). The scatter in the relation between γ and M is quite large, with galaxies with steep central cusps ($\gamma \sim 0.6$) found over the entire magnitude range (once the brightest galaxies are removed). Galaxies brighter than $M_B \sim -20.2$ mag (best fit by a core-Sérsic profile), are clearly distinct from the rest of the sample in having inner slopes shallower than expected based on the extrapolation of the trend shown by the fainter systems (in agreement with the correlation between μ_0, $\mu_{0.05}$ and M noted in point 1).

Points 1, 2 and 5 leave no doubt that the brightest galaxies ($M_B \lesssim -20.5$) are set apart from the rest of the sample insofar as innermost regions (a few hundred parsecs) are concerned. However, the clear dichotomy in the distribution of effective radii (see point 4 above) reveals a physical disconnect in the overall structure as well. We will discuss the implications of these findings in the next section. Fits to some of the scaling relations shown in Figure 18 are given below, where "S" and "CS" refer to the samples of Sérsic and Core-Sérsic galaxies respectively.

$$\mu_{0.05}(z) = (1.65 \pm 0.09)(M_B + 18) + (15.7 \pm 0.13) \quad \text{S} \quad (17)$$

$$\mu_{0.05}(z) = -(1.06 \pm 0.38)(M_B + 18) + (11.0 \pm 1.3) \quad \text{CS} \quad (18)$$

$$\mu_{0.05}(g) = (1.51 \pm 0.09)(M_B + 18) + (17.1 \pm 0.13) \quad \text{S} \quad (19)$$

$$\mu_{0.05}(g) = -(0.97 \pm 0.38)(M_B + 18) + (12.8 \pm 1.2) \quad \text{CS} \quad (20)$$

$$\mu_{r_e}(z) = (0.76 \pm 0.10)(M_B + 18) + (20.5 \pm 0.1) \quad \text{S} \quad (21)$$

$$\mu_{r_e}(z) = (0.31 \pm 0.48)(M_B + 18) + (23.2 \pm 1.3) \quad \text{CS} \quad (22)$$

$$\mu_{r_e}(g) = (0.63 \pm 0.10)(M_B + 18) + (21.8 \pm 0.13) \quad \text{S} \quad (23)$$

$$\mu_{r_e}(g) = (0.14 \pm 0.43)(M_B + 18) + (24.1 \pm 1.2) \quad \text{CS} \quad (24)$$

$$\log n(g) = -(0.10 \pm 0.01)(M_B + 18) + (0.39 \pm 0.02) \quad \text{All} \quad (25)$$

$$\log r_e(g) = -(0.055 \pm 0.023)(M_B + 18) + (1.14 \pm 0.03) \quad \text{S} \quad (26)$$

$$\log r_e(g) = -(0.22 \pm 0.13)(M_B + 18) + (1.50 \pm 0.37) \quad \text{CS} \quad (27)$$

5. DISCUSSION AND CONCLUSIONS

5.1. *Are Early-Type Galaxies divided in "Core" and "Power-Law" types?*

Although the first systematic surveys of the cores of elliptical galaxies date back to the late '70s - early '80s (King 1978; Schweizer 1979; Kormendy 1985; Lauer 1985), it was only with HST that core properties could be studied in detail. For instance, in the best ground-based seeing conditions, the cores of a few giant ellipticals appeared isothermal (Kormendy 1985); even before refurbishment, HST revealed this not to be the case (Crane et al. 1993). The first HST studies also seemed to indicate a dichotomy in the core properties of bright elliptical galaxies. Ferrarese et al. (1994) divided a magnitude limited sample of fourteen galaxies in the Virgo cluster into two broad classes: the fainter galaxies appeared to have power-law profiles, which showed no indication of flattening to the smallest radius resolved by the instrument, while the brightest third of the sample showed resolved (non isothermal) cores, producing a clear break in the surface brightness profile. Lauer et al. (1995) strengthened these results using a larger (although not as homogeneous) sample of galaxies. Lauer et al. (1995) and Faber et al. (1997) introduced the currently adopted definition of a "core" galaxy as one for which the logarithmic slope of the surface brightness profile (measured using a Nuker fit) is $\gamma < 0.3$ as one approaches the resolution limit of the instrument ($0''.1$ for their study). In agreement with Crane et al. (1993) and Ferrarese et al. (1994), Lauer et al. also found no cases in which $\gamma = 0$. Furthermore, Lauer et al. found no galaxies for which $0.3 < \gamma < 0.5$, and refer to galaxies for which $\gamma > 0.5$ as "power-law". The separation between core and power-law galaxies in Lauer et al.'s sample is dramatic, with no overlap between the two classes; a more recent study by the same authors (Lauer et al. 2005) confirms this stark bimodality. This conclusion was partly challenged by Rest et al. (2001), who found that 10 galaxies (15% of their sample) had profiles with $0.3 < \gamma < 0.5$, the region devoid of galaxies in Lauer et al. (1995) sample. Rest et al. note that a Nuker model, by virtue of the fact that it approximates the profile with two power-laws, will bias the value of γ if the slope of the surface brightness profile varies smoothly with radius.

Figure 19 shows the γ distribution for the ACSVCS galaxies. The logarithmic slope in the figure is calculated from the best fitting model at $r = 0''.1$; it is equal to the slope of the inner power-law for galaxies best fit by a core-Sérsic profile, and follows equation 16 for Sérsic galaxies. We stress that the definition of γ adopted in this paper is significantly different from that commonly found in the literature. The slope of a Sérsic model changes continuously with radius, therefore it will generally be shallower at the center than the slope obtained if a power-law fit (as

in the Nuker model) is enforced (a point already made by Rest et al. 2001). More importantly, nuclei are excluded in this study, i.e., γ is defined as the slope of the underlying host galaxy, unbiased by the nuclear component, if present. Previous studies often blocked out the nucleus when fitting the galaxy profile, however, unrecognized nuclei (especially in bright galaxies) would have biased γ towards larger values.

The γ distribution for the entire ACSVCS sample (plotted as a thick solid line in Figure 19) is strongly skewed; however, the only hint of bimodality is a modest, and not statistically significant, excess of galaxies with $\gamma \sim 0.5$. Moreover, the physical cause driving the shape of the γ distribution shown in Figure 19 is dramatically different from the one proposed by Lauer et al. (1995) and subsequent papers by the same group. In these earlier works, γ was found to increase going from bright to faint galaxies: the low-γ peak of the distribution was occupied exclusively by the brightest "core" galaxies, while the high-γ tail was defined by the faintest "power-law" galaxies (some of which were as faint as the faintest ACSVCS galaxies). This result was challenged by Graham & Guzman (2003) and is indeed at odds with our findings: *it is the faintest, not the brightest galaxies that have the shallower inner profiles.*

The left-side panel of Figure 19 shows the γ distribution for three samples: all bright galaxies best fit by a core-Sérsic profile, and all galaxies brighter and fainter than $B_T = 13.7$ mag (corresponding to the dividing point between elliptical and dwarf galaxies in the VCC). The high γ peak is populated almost exclusively by bright ($B_T < 13.7$ mag) Sérsic galaxies, although their distribution extends to values of γ as low as 0.1, i.e., the range previously believed to be populated exclusively by core galaxies. Galaxies best fit by a core-Sérsic profile have generally lower values of γ ($\lesssim 0.4$) but their distribution overlaps with that of the previous sample. The histogram bin at the lowest γ value is populated preferentially not by the core galaxies, but by the faintest galaxies in the survey ($B_T > 13.7$). We note that the slight peak at $\gamma \sim 0.5$ disappears, producing a monotonic decrease in the distribution as γ increases, if only "regular" galaxies (i.e., not showing evidence of multiple morphological components - bars, stellar disk, rings) are considered, as shown in the right panel of Figure 19 (dashed line). In other words, the γ distribution for the population of E+dE galaxies is skewed, but most certainly unimodal.

The above results indicate that there is no justification, based on the shape of the γ histogram, for dividing early-type galaxies into "core" and "power-law" types as defined by Lauer et al. (1995). Such a distinction was born from the observation of a clearly bimodal distribution of inner slopes. Our study shows instead that the distribution of the slopes of the inner profiles for E+dE galaxies is unimodal although strongly skewed towards small γ. The addition of galaxies with multiple morphological components (mainly disks) enhances the high-γ end of the histogram, but not enough to produce a clearly bimodal distribution.

In view of the above discussion, the definition of "core" galaxies as in Lauer et al. (1995) appears untenable: according to this definition, most of the ACSVCS dwarfs (e.g., VCC 1886, VCC 1993, VCC 21, etc.) should be classified as core galaxies. Lauer et al. claim that cores are the result of the evolution of binary black holes, a clear impossibility for the dwarf galaxies – insisting on such definition would therefore demand different physical explanations for the formation of "cores" in dwarfs and bright ellipticals. As stressed by Graham et al. (2003) and several papers by the same group, adoption of a Sérsic instead of a Nuker model to characterize the surface brightness profiles (a choice justifiable on the simple ground that certainly on large scales, and often on small scales, profiles are not well approximated by power-laws) allows one to interpret the flattening of the inner profiles in faint systems as a natural extension of the trend seen in brighter counterparts, a trend which is broken only by the very brightest ellipticals with $M_B \lesssim -20.5$. A revision along the lines proposed by Graham et al. (2003), who define a galaxy as having a "core" if the surface brightness in the inner region is lower than the inward extrapolation of the Sérsic profile best fitting the outer parts, is more consistent with our findings. With this definition, the brightest ~ 10 galaxies (those best fit by a core-Sérsic model and which, ironically, are the only ones to have power-law inner profiles) are "core" galaxies, while the faintest galaxies (which follow a Sérsic profile all the way to the center) are not, in spite of having shallower inner profiles.

5.2. *Core Galaxies, Mass Deficit and Supermassive Black Holes*

The brightest ~ 10 galaxies are clearly distinct from the rest of the sample insofar as the properties of the inner 300-400 pc region are concerned. These galaxies lack a distinct stellar nucleus (see also Paper VIII), and have central surface brightness and inner profile slopes which are lower than expected based on the extrapolation of scaling relations defined by fainter systems (upper and lower left panels of Figure 18). Although this is in agreement with previous studies (e.g., Graham & Guzman 2003; Jerjen & Binggeli 1997), such studies also found that if the inner few hundred parsecs are neglected, there is a continuity in the structural properties of bright and faint ellipticals, likely suggesting a common formation scenario. This statement is not entirely supported by the ACSVCS data; i.e., we find that core galaxies can be distinguished from the rest of the sample also on the basis of some large-scale structural properties. In particular, although the Sérsic index n for core galaxies lies along the relation established by the rest of the sample (lower right panel of Figure 18, see also Graham et al. 2003; Graham & Guzman 2003; Jerjen & Binggeli 1997), the effective radii r_e are significantly larger than expected based on the trend displayed by fainter systems (upper right panel of Figure 18 and panel *dd* of Figure 17, *cf.* Figure 7 of Binggeli, Sandage & Tarenghi 1984). The significance of these results will be addressed in a forthcoming paper, in which the ACSVCS sample will be augmented with a similarly defined sample of early-type galaxies in the Fornax cluster. Based on the present study, however, our interim conclusion is that *the distinguishing features of core galaxies are not relegated exclusively to the innermost regions, but extend to include the overall galactic structure.*

Finally, we will comment briefly on the connection be-

tween cores and supermassive black holes. The two have long been linked together (Lauer et al. 1995; Faber et al. 1997; Rest et al. 2001). N-body simulations by Milosavljević & Merritt (2001) followed the evolution of the SBHs binary which forms as a consequence of the merger of two galaxies with inner power-law profiles. They find that the binary decays through the gravitational slingshot of stars in the inner region: in a gas-free environment the process can eject an amount of mass comparable to the combined mass of the two SBHs, with the result that the merger product will form a core. Estimates of the "missing mass" in core galaxies have been carried out by Milosavljević et al. (2002), Ravindranath et al. (2002) and Graham (2004). We follow Graham (2004) by defining the mass deficit within the break radius as the difference between the mass contained within the extrapolation of the Sérsic model which best fits the profiles at larger radii, and the mass enclosed by the power-law which corresponds to the best fitting core-Sérsic model to the actual profile. Figure 20 shows the result of this exercise; SBH masses have been calculated from the $M_{SBH}-\sigma$ relation of Ferrarese & Ford (2005) using published values of σ, the stellar velocity dispersion[16]. Mass deficits have been calculated as in Graham et al. (2004), assuming that the $R-$band mass to light ratio M/L scales with luminosity as in van der Marel (1991), and the R and $z-$band magnitudes and colors for the Sun and giant ellipticals are (Fukugita et al. 1995): $M_{R,\odot} = 4.28$, $M_{z,\odot} = 4.51$, $(R-z)_{gal} = 0.54$[17]. Excluding VCC 798, for which the Sérsic index and mass deficit might be biased by the presence of a large-scale stellar disk, the mean ratio between mass deficit and SBH mass for our sample is 2.4 ± 1.8, in agreement with Graham et al. (2004, 2.1 ± 1.1), implying that the galaxies have undergone no more than a few major mergers since the last event which involved gas dissipation.

5.3. *One Sequence of Early-Types, from Dwarfs to Giants?*

The question of how "regular" and "dwarf" ellipticals are related, if indeed they are, has been discussed in the literature since the mid 1980s. That a distinction might exist was originally prompted by the observation that dwarf, low luminosity ($M_B \gtrsim -18$ mag, Binggeli et al. 1985) ellipticals are not well described by the same de Vaucouleurs $R^{1/4}$ law as brighter ellipticals, their profiles being more closely exponential (Binggeli, Sandage & Tarenghi 1984; Lin & Faber 1983). A structural dichotomy between regular and dwarf ellipticals was further stressed by Kormendy (1985), who claimed a markedly different correlation between core radius, central surface brightness and total magnitude for the two classes. In particular, according to the latter study, while the central surface brightness of dwarf ellipticals becomes brighter as the total luminosity increases, in bright ellipticals the two quantities appear anti-correlated, prompting the conclusion that "dwarf elliptical galaxies are very different from the sequence of giant ellipticals. [...] dwarf spheroidals and ordinary ellipticals were formed in very different ways." Indeed, the term "spheroidal" (rather than elliptical), when referring to elliptical galaxies fainter than $M_B \sim -18$ mag was introduced partly to reinforce the physical distinction between the two classes (e.g., Kormendy 1985; Djorgovski 1992). More moderate views were taken, for instance, by Caldwell (1983), Binggeli, Sandage & Tarenghi (1984) and Binggeli (1994). In particular, a parametric representation of the surface brightness profile carried out in the first two contributions, led to a continuous sequence extending from $M_B \sim -22$ to $M_B \sim -12$, thus uniting "regular" ellipticals and "dwarf" systems under one single $M_B - \mu_0$ scaling relation. Binggeli (1994) cautioned that the striking dichotomy observed by Kormendy (1985) could partly be due to the lack, in Kormendy's sample, of galaxies in the $-20 < M_B < -17$ range, corresponding precisely to the transition region between the two families.

In the past ten years, the view that dwarf ellipticals are, morphologically, the extension of brighter systems has gained further support, and the question has shifted instead to whether the very brightest ellipticals (the core galaxies discussed in §5.1 and §5.2, with $M_B \lesssim -20.5$ mag) are distinguished from the rest of the elliptical population. For instance, Young & Currie (1994) found that when the surface brightness profile of dwarf ellipticals is characterized as a Sérsic model, the Sérsic index n strongly correlates with the total luminosity: the profile evolves from exponential ($n \sim 1$) to an almost de Vaucouleurs profile ($n \sim 4$) as M_B decreases (i.e., the luminosity increases). Jerjen & Binggeli (1997) showed that the trend extends to bright ellipticals, translating into a well defined correlation between n and M_B in the range $M_B \sim -22$ to $M_B \sim -14$. The ensuing correlation between M_B and μ_0 (with μ_0 increasing with luminosity) is violated only by galaxies brighter than $M_B \sim -20.5$ mag (what we defined in §5.2 as core galaxies), but no break is seen corresponding to the "canonical" $M_B = -18$ magnitude which supposedly divides ellipticals from dwarfs. Jerjen & Binggeli conclude that "the diffuse, low-surface brightness dwarf galaxies are the true low-luminosity extension of the classical giant ellipticals". In the most recent contribution to the subject, Graham et al. (2003) and Graham & Guzman (2003) confirm that, from a structural point of view, 1) there is no dichotomy in the $M_B - \mu_0$ scaling relations at $M_B \sim -18$, indeed there is nothing significant altogether associated with this magnitude; 2) dwarf ellipticals are the low-luminosity extension of, and likely share the same formation mechanisms as bright ellipticals; and 3) the "break" in the $M_B - \mu_0$ correlation observed at $M_B \sim -20.5$ mag is the result of the core evolution undergone by the brighter systems after formation.

These studies have established that the structural dichotomy between dwarf and regular ellipticals as advocated by Kormendy (1985) was likely the result of observational biases. Nevertheless, different clues indicate a high degree of complexity within the population of dwarf galaxies. Conselice et al. (2001) and Drinkwater et al. (2001) found that, in dense environments, the spatial and kinematical distribution of dwarf ellipticals is broader than that of giant ellipticals, and more closely re-

[16] References can be found in the HyperLeda database, http://leda.univ-lyon1.fr/hypercat, Prugniel et al. (1997).

[17] Note that R magnitudes are defined in the Vega photometric system, while z magnitudes are defined in the AB system.

sembles that of spirals. Dynamically, dwarfs do not form a homogeneous family, with at least some systems being rotationally supported (Mateo 1998; Pedraz et al. 2002; Geha et al. 2003; van Zee, Skillman & Haynes 2004). Finally, the stellar age and metallicity differ significantly from dwarf to dwarf (Poggianti et al. 2001), suggesting that not all dwarfs share a common origin and evolutionary history. There is some support in our data for dwarfs forming a complex and diverse population. In particular:

1. The fainter galaxies ($-15 \lesssim M_B \lesssim -17$) display – more so than their bright counterparts – a broad variety of surface brightness profiles, from purely exponential (e.g., VCC 1948, $M_B = -16.0$) to almost $R^{1/4}$ law (e.g., VCC 1993, $M_B = -15.8$).

2. Once the nuclear component has been removed, the central surface brightness estimated for the faintest galaxies spans a broad range (a factor ~ 200 at a fixed galaxy magnitude, Figure 18), more so than for the brighter systems.

3. Dwarf galaxies with $M_B > -17.5$ comprise both nucleated and non-nucleated varieties (Figure 18). The brightest galaxies ($M_B < -20$ mag) do not show any evidence of stellar nuclei. Some of the galaxies with intermediate luminosity are nucleated, although they all are consistent with a nucleus being present, but falling below the level of detectability due to the high central surface brightness of these galaxies (Paper VIII). The dwarf class is therefore heterogeneous insofar as the presence of a nuclear component. Brighter galaxies might not be (they could all be nucleated), although the very brightest certainly are not (none has a stellar nucleus).

4. Morphologically, dwarf ellipticals form a rather heterogeneous class, with some systems showing evidence of spiral structures, disks and recent star formation.

5. Although dwarf and giant ellipticals show comparable amount of scatter in a color-magnitude diagram (§5.5), Mei et al. (2005) noted that dwarf ellipticals show larger scatter in the $z-$band Surface Brightness Fluctuation (SBF) magnitudes $\bar{m}_{850}$. This may indicate a larger spread in ages/metallicity for the dwarfs compared to bright ellipticals, in agreement with Poggianti et al. (2001).

The origin of dwarf galaxies is still highly controversial, and a detailed review is beyond the scope of this paper. Briefly, dwarfs could have formed early during the life of a protocluster (e.g., White & Frenk 1991; Dekel & Silk 1986); they could be the result of passive evolution of compact blue galaxies (e.g., Babul & Rees 1992); or they could be the remnants of stripped dwarf spirals which are accreted onto a cluster (e.g., Moore, Lake & Katz 1998; Conselice et al. 2001; Mastropietro et al. 2005). Here, we will comment briefly on the latter scenario. Figure 21 shows the Sérsic index n plotted against $g-$band central surface brightness and total $B-$band magnitude for the ACSVCS galaxies and the sample of spiral bulges analyzed by Graham (2001). The latter study presented Sérsic fits to the bulge components of 86 undisturbed face-on spiral galaxies, originally observed by de Jong & van der Kruit (1994). Low luminosity ellipticals and bulges are clearly distinct: at a given profile shape (n), bulges are brighter than ellipticals by at least two B-band magnitudes, and have brighter central surface brightness. A least square fit to the bulge population shown in Figure 21 gives:

$$\log n(z) = -(0.073 \pm 0.01)(M_B + 18) + (0.021 \pm 0.03) \quad (28)$$

$$\log n(z) = -(0.10 \pm 0.01)(\mu_0 - 18) + (0.052 \pm 0.022) \quad (29)$$

For comparison, the equivalent equations for early-type galaxies best described by Sérsic profiles are as given by equation 25 and:

$$\log n(z) = -(0.070 \pm 0.066)(\mu_0 - 18) + (0.35 \pm 0.01) \quad (30)$$

Figure 21 can provide some observational constraints on galaxy harassment theories, if indeed dwarf ellipticals are the result of tidal stripping of spirals accreted onto clusters (e.g., Conselice et al. 2001 and references therein). For instance, Moore et al. (1998) predict that the surface brightness profile of harassed spirals should steepen (their Figure 4), i.e., the harassed bulge should move up (larger n) and to the right (brighter μ_0) in the left panel of Figure 21, i.e., towards the general area occupied by the ACSVCS galaxies (this argument assumes, of course, that present day bulges are representative of bulges at $z \sim 0.4$, i.e., at the epoch when stripping has yet to take place). An additional possibility to reconcile the early-type and bulge populations in Figure 21 is to invoke merging: unequal mass mergers would only slightly impact the magnitude of the product, but could have profound effects on its density profile. For instance, N-body simulations by Eliche-Moral et al. (2005) show that unequal mass mergers of spiral galaxies would lead to a merger product with structural parameters which might resemble those of the dwarfs in the ACSVCS sample. The arrow in the right panel of Figure 21 shows where the exponential ($n = 1$) bulge of a spiral would "move" after merging with a satellite of half its mass (and, we assume, luminosity), according to these simulations. Dissipation during merging would also move bulges in the same general direction: by steepening the density profile it would lead to an increase in luminosity, n, and central density.

5.4. *Isophotal Shapes*

It has long been known that the shapes of ellipticals show good correlations with a variety of other properties, such as optical luminosity (Nieto & Bender 1989; Nieto et al. 1991), optical central surface brightness (Nieto et al. 1991), X-ray and radio fluxes (Bender et al. 1987, 1989), and stellar kinematics (Bender 1988). The extent of these correlations, which apply to the core properties as well (Ferrarese et al. 1994; van den Bosch et al. 1994; Lauer et al. 1995; Rest et al. 2001; Lauer et al. 2005),

has prompted the use of the term "dichotomy", with optically bright ellipticals being preferentially round, boxy, pressure supported and often showing nuclear activity, while fainter systems are more elongated, disky, rotationally supported and show little or no radio and X-ray emission.

Figure 22 shows the intensity weighted mean B4 coefficient and ellipticity for the ACSVCS galaxies, calculated in two radial ranges: $r < 0.1r_e$ (left panels) and $0.1r_e < r < r_e$ (right panels). While on large scales all galaxies are consistent with having regular isophotes ($B4 \sim 0$), in the innermost regions there is a trend for $B4$ to increase as galaxies get fainter. In agreement with previous works, this trend is a result of the fact that the core galaxies (i.e., the brightest galaxies in the sample) are preferentially boxy, while galaxies immediately following in the luminosity function often display stellar disks, producing elongated isophotes. Dwarf systems have isophotes which are consistent, within the errors, with being elliptical. With the exception that no high ellipticity objects are found in core galaxies, there is, however, no clear trend of ellipticity with luminosity: galaxies with $M_B > -20$ span the entire ellipticity range, regardless of luminosity.

The issue of the intrinsic shape of elliptical galaxies has been addressed in many works (Sandage, Freeman & Stokes 1970; Lambas, Maddox & Loveday 1992; van den Bergh 1994; Rix & White 1990, 1992; Jørgensen & Franx 1994; Michard 1994). Figure 23 shows the distribution of minor to major axes ratios, b/a, for the entire sample of ACSVCS galaxies, and for samples divided according to magnitude, Sérsic index n, and morphological classification. The thick solid line in the upper right panel of the Figure shows the distribution expected for a population of oblate galaxies with intrinsic axial ratio $b/a = 0.2$ – selecting a different intrinsic b/a has the effect of truncating the distribution at the new b/a, without changing the overall shape. The observed distribution is in excellent qualitative agreement with the distribution derived by Lambas, Maddox & Loveday (1992) for a sample of over 2000 ellipticals (upper panel of their Figure 2). Lambas et al. note that a pure oblate or prolate population cannot account for the observed distribution, and conclude that a population of mildly triaxial galaxies (with major to intermediate axial ratio of 0.8) matches the observations best.

Different axial ratio distributions are expected if galaxies belonging to different sub-samples (giant and dwarf ellipticals, or galaxies described by de Vaucouleurs and exponential profiles) have different distributions of intrinsic shapes. Although larger samples would be desirable, statistically different distributions are seen only when the sample is divided between E+dE and S0+dS0 galaxies. In this case, a Kolmogorov-Smirnov test shows that the ellipticity distributions differ at the 1.5σ level, with a deficiency of round S0+dS0 galaxies. This is a likely an observational bias due to the fact that bulge-dominated face-on bulge+disk systems are not easily recognizable (e.g. Jørgensen & Franx 1994). The ellipticity distribution for samples divided between bright ($M_B < -18.5$) and faint ($M_B > -17.5$) galaxies, E and dE and galaxies with nearly de Vaucouleurs profiles ($n > 3$) and those with nearly exponential profiles ($n < 2$) are consistent well within the 1σ level.

5.5. *The Color-Magnitude and Color-Color Relations of Early-Type Galaxies in Virgo*

Because the colors and magnitudes of a stellar population are affected by its age, metallicity, as well as its mass, these can be constrained by a study of color-magnitude diagrams. The $(g-z)-g$ color magnitude relation for the ACSVCS galaxies is shown in Figure 24. Magnitudes in the g and $z-$bands (Table 4) are calculated by integrating to infinity the best fitting Sérsic or core-Sérsic models (thus excluding a nuclear component, if present); while $g-z$ colors (last column of Table 4) are calculated directly from the images, by integrating the azimuthally averaged profiles between $1''$ (to avoid a nuclear component) and either one effective radius, or the radius at which the surface brightness profile, in either band, is less than one magnitude above the sky, whichever radius is the smallest. The error associated to the $g-z$ color accounts only for the error in the sky background values, added in quadrature. The left panel of Figure 24 shows the data with error-bars, while in the right panel are over-plotted single burst stellar population models from Bruzual & Charlot (2003), assuming a Salpeter IMF and lower/upper mass cutoffs of $0.1/100 M_\odot$. The models are calculated for metallicities between [Fe/H] $= -2.25$ (yellow) and [Fe/H] $= +0.56$ (red), ages between 1 and 15 Gyr (shown as solid dots along each iso-metallicity track, with older galaxies becoming redder), and mass between 10^8 and 10^{12} $M_\odot$ (with the least massive models having fainter total magnitude). The well defined relation seen in the Figure, with fainter galaxies becoming progressively bluer than brighter ones, has been discussed widely in the literature (e.g., Baum 1959; Bower, Lucey & Ellis 1992; Blakeslee et al. 2003; Bernardi et al. 2005; Hilker et al. 1999; Secker et al. 1997). It is immediately apparent from Figure 24 that the relation is non-linear: dwarf galaxies are bluer than expected based on a linear extrapolation of the relation defined by the bright systems. Error-weighted least square fits to galaxies brighter and fainter that $M_g = -18$ give, respectively:

$$(g-z) = (1.41 \pm 0.02) - (0.045 \pm 0.005)(M_g + 18) \quad (31)$$

and

$$(g-z) = (1.30 \pm 0.03) - (0.070 \pm 0.020)(M_g + 18) \quad (32)$$

These results do not change significantly if galaxies with multiple morphological components (shown as blue points) are removed from the sample. The two relations given in equations 31 and 32 are shown in Figure 24 as dashed and dotted lines, respectively. A satisfactory fit to the entire sample requires the use of a quadratic relation:

$$(g-z) = (1.373 \pm 0.003) - (0.086 \pm 0.003)(M_g + 18) - \\ - (0.0077 \pm 0.0011)(M_g + 18)^2 \quad (33)$$

(see Jordán et al. 2005); this is shown as a solid line in Figure 24. A more subtle point is whether the intrinsic scatter in the relation increases as one moves from brighter to fainter systems, as one would expect if, for instance, dwarf galaxies span a wider range in ages and/or metallicities than brighter galaxies. The reduced χ^2 of the quadratic fit given in equation 33 is $\chi^2_r = 3.7$, indicating that part of the observed scatter is indeed intrinsic. However, the χ^2_r is virtually identical whether the sample is restricted to faint ($M_g > -18$) or bright ($M_g < -18$) systems; in other words, the apparently larger scatter shown by faint galaxies in Figure 24 is consistent with being due to the larger measurement errors in the $g-z$ colors for these systems. The same conclusion applies if χ^2_r is measured from the linear fits given in equations 31 and 32.

Six galaxies stand out as being significant outliers in Figure 24 and were excluded from the fits discussed above. In particular, four galaxies are located above the color distribution shown in Figure 24, i.e., they have significantly redder colors than expected given their magnitude. In order of decreasing luminosity, these galaxies are VCC 1327 (NGC 4486A), VCC 1297 (NGC 4486B), VCC 1192 (NGC 4467), and VCC 1199. VCC 1327 projects close to a bright foreground star and hosts a nuclear dust disk; its color and magnitude are more uncertain than is the case for other galaxies. In addition, the galaxy lies just over 7′ to the North-West of M87, and might be tidally truncated. The other three galaxies are also found in close proximity of brighter companions (see Appendix and §4.1.4), and were indeed flagged as being tidally stripped from inspection of the images and brightness profiles. It is therefore likely that for all four galaxies, the red colors are consistent with the magnitude of the galaxy before tidal stripping took place. On the blue side of the main relation there are two significant outliers, VCC 1499 ($g-z = 0.51$; $M_g = -16.16$), and VCC 798 (M85, $g-z = 1.38$; $M_g = -22.03$). VCC 1499 is classified as a dIrr/dE transition object from inspection of the images[18]. VCC 798 likely hosts a large-scale stellar disk, and is peculiar in having a significant excess of diffuse star clusters, relative to other galaxies in the sample (Peng et al. 2005b); it also displays strong isophotal twists.

The brightest core galaxies are well characterized as 12 Gyr old stellar systems with baryonic mass $\sim 10^{12}$ $M_\odot$ and solar metallicity ([Fe/H] $\sim +0.09$). As expected, the faintest galaxies are less massive, in the neighborhood of 10^9 $M_\odot$; their bluer colors can be interpreted as either (or both) a consequence of younger age or lower metallicity. Figure 25 shows an optical-NIR color-color diagram; although the scatter is large, most systems are consistent with stellar ages between 8 and 15 Gyrs, and metallicities in the range $-0.64 <$ [Fe/H] < 0.09, with metallicity being the primary driver for the colors becoming bluer with decreasing galaxy luminosity. This conclusion is consistent with the observed lack of redshift evolution of the slope of the color-magnitude relation for early-type galaxies (Kodama & Arimoto 1997; Kodama et al. 1998; Blakeslee et al. 2003)

[18] Four more galaxies – VCC 21, VCC 1488, VCC 1857 and VCC 1779 – which also closely resemble VCC 1499 (low surface brightness, elongated system with a small gradient in the surface brightness profile) are also found to lie in a group at $g-z \sim 0.85$, $M_g \sim -16.3$.

Appendix A: Notes on Individual Galaxies

This appendix presents a collection of notes on individual galaxies. Some of the features discussed, especially for the brightest galaxies, had already been known based on previous studies (see for instance, studies by and references in Crane et al. 1993; Jaffe et al. 1994; Lauer et al. 1995, 2002, 2005; Verdoes Kleijn et al. 2005; Carollo et al. 1997; van den Bosch & Emsellem 1998). The purpose of this section is simply meant to highlight features which are immediately apparent by visually inspecting the g, z and $g-z$ images, as well as the isophotal parameters.

1. VCC 1226 (M49, NGC 4472). A thin, boomerang-shaped dust lane crosses the galaxy's center at a position angle of roughly –45°, extending $\approx 1\farcs5$ on either side. Faint dust patches are seen within $3\farcs5$ of the center. There is no indication of a nucleus from the dust-corrected images. The isophotes show no significant deviations from ellipses.

2. VCC 1316 (M87, NGC 4486). The inner $0\farcs25$ of the $g-$band image is saturated. The optical synchrotron jet emanating from the unresolved, non-thermal nucleus, is clearly visible and was masked prior to the isophotal analysis. Dust filaments radiate from the center outwards, extending out to 13″ from the nucleus. There are two very red objects close to the galaxy center: one directly south of the nucleus, at a distance of $\approx 6''$, the other southeast of the nucleus at a distance of $11\farcs5$. The former appears to be a globular cluster, and the latter a faint background galaxy. The isophotes appear very regular.

3. VCC 1978 (M60, NGC 4649). This galaxy shows very regular isophotes, with no evidence of a morphologically distinct nuclear component.

4. VCC 881 (M86, NGC 4406). NGC 4406 is a well known example of a galaxy moving through a cluster at supersonic velocity (e.g., White et al. 1991; Rangarajan et al. 1995; Stickel et al. 2003; Elmegreen et al. 2000); on-going dust stripping is believed to be taking place as a consequence. The ACSVCS residual images indeed show several dust filaments radiating from the center, mainly in the South-East quadrant, all the way to the edge of the chip. The isophotes are regular, a fact reflected in the constancy of the ellipticity and position angle, and in the fact that all higher order coefficients are consistent with zero. However, in the inner $0\farcs4$, the surface brightness profile decreases inward, a fact first noticed by Carollo et al. (1997). At first sight, this behavior is consistent with what is expected from a small dust disk, however, the color image shows no color difference between this region and the surrounding areas. The other explanation is that the stellar density actually decreases within this region. However, the "depleted" area appears, in projection, quite round, rounder than the galaxy isophotes, and might even be slightly mis-centered (extending more to the South-East).

5. VCC 798 (M85, NGC 4382). The isophotes are very boxy within 1″; the boxiness persists all the way to the center, where there almost seems to be a "butterfly"

pattern, extending about 0″.3 on either side and aligned with the major axis of the galaxy. The isophotes become distorted beyond $\sim 50''$. The residual image shows the possible presence of two small dust patches about 4″ South-West of the center. There is no evidence of a nucleus.

6. VCC 763 (M84, NGC 4374). Like M87 (=3C 374), M84 (=3C 272.1) is a well known radio source. Two parallel dust lanes, one crossing (but not centered on) the galaxy's center, the other just North of the first, run in the East-West direction. The larger (northern) dust lane extends for approximately 14″, while the lane crossing the center extends for about 5″. Both lanes are surrounded by fainter dust wisps and filaments. The isophotes are very regular.

7. VCC 731 (NGC 4365). The galaxy is a member of the W-cloud, at a distance of ~ 23 Mpc (Mei et al. in preparation). A resolved, slightly elongated nucleus is clearly visible in the color image, as well as in the individual frames. The nucleus is bluer than the surrounding galaxy and clearly affects the surface brightness profiles, in particular in the $g-$band. The isophotes appear quite regular.

8. VCC 1535 (NGC 4526). This galaxy hosts a large dust disk, very reminiscent of the one seen, at lower inclination, in VCC 1154. The disk extends 15″.6 on either side of the galaxy's center, and is aligned with the major axis of the galaxy (in the East-SouthEast direction). The plane of the disk makes an angle of approximately 15° to the line of sight, the Northern side being the closest. There are several blue knots within the disk, probably indicative of star formation. Because the underlying stellar population within the disk is likely different from that characterizing the main body of the galaxy, the dust-correction for this galaxy fails, and the isophotes can only be recovered outside a semi-major axis of 7″. At a radius of approximately 10″ the isophotes become visibly boxy; the boxiness is rather extreme at a radius of 20″. Beyond, the isophotes assume a diamond shape appearance (as a consequence the A4 coefficient becomes non-zero), and finally become disky at a radius of approximately 70″.

9. VCC 1903 (M59, NGC 4621). The $g-$band images are saturated within the inner 0″.25. Based on the $z-$band image alone, it is hard to judge the presence of a morphologically distinct nucleus; however, an edge-on, thin, faint stellar disk, extending at least 10″ from the center is clearly present. The presence of the disk is reflected in the B4 coefficient.

10. VCC 1632 (M89, NGC 4552). Two thin dust filaments radiate from the center in the West-NorthWest direction, out to a distance of about 6″. Small dust patches are visible within 11″. A small dust patch, less than 1″ across, surrounds (but it is not centered on) the center of the galaxy. There is a very red object to the South-West of the center, at a distance of about 10″. The isophotes are very regular, there is no indication of a nucleus.

11. VCC 1231 (NGC 4473). Rather elongated system; the color image shows no evidence of dust, however, there is a small (less than 1″) thin rectangular feature crossing the center of the galaxy. This feature is aligned with the major axis and bluer than the surrounding regions; it is probably responsible for the negative B4 coefficient in the very innermost region. Further out, the galaxy becomes disky, and remains so out to about 10″. There doesn't appear to be a morphologically distinct nucleus.

12. VCC 2095 (NGC 4762). This galaxy has a very thin, edge-on disk, extending all the way to the edge of the CCDs. Within the inner 15″ on either side of the nucleus, the disk appears to become thinner and fainter as the radius decreases; it reaches maximum surface brightness between 15″ and 40″ from the center, and it is bluer than the surrounding galaxy.

13. VCC 1154 (NGC 4459). This galaxy harbors a spectacular dust disk, similar to the one seen, at higher inclination, in VCC 1535. The disk is about 17″ across, and its plane is inclined by $\sim 45°$ to the line of sight. There are several blue clumps in the disk, probably indicative of star formation. Several wisps and filaments extend beyond the edge of the disk. As for the case of VCC 1535, the correction for dust fails, and the profile can only be recovered beyond 7″.5 from the center. Unlike the case of VCC 1535, the isophotes look regular.

14. VCC 1062 (NGC 4442). This galaxy appears quite regular within the inner 15″. Beyond, the isophotes become boxy, and a faint elongated outer envelope dominates the galaxy's appearance. This is slightly tilted (towards South) relative to the inner regions, causing the isophotes to twist slightly. The images show no strong evidence of a morphologically distinct nucleus.

15. VCC 2092 (NGC 4754). This galaxy has two morphologically distinct components: the main body, which appears quite regular, and a misaligned (by about 45°) bar, extending out to 25″ from the center. A faint nucleus is likely present.

16. VCC 369 (NGC 4267). This galaxy is quite round in the innermost 6″; beyond it becomes more elongated, with perhaps a slight twist in the major axis position angle, to revert to round again beyond 50″. It is possible that the change in the isophotal shape is due to a stellar bar similar (but much fainter) to the one seen in VCC 2092. A faint nucleus is likely present.

17. VCC 759 (NGC 4371). This galaxy has a small dust disk at the center, only about 1″.6 across. The disk is inclined by about 26° to the line of sight, and its major axis seems to coincide with the major axis of the galaxy (which is aligned in the East-West direction). The structure beyond is not easily interpretable. There seems to be a thin (less than 1″ across) blue nuclear stellar ring centered on the galaxy's center, with a radius just below 11″. The inclination and orientation of the stellar ring are the same as those of the nuclear dust disk. Within this ring, there seems to be at least one additional blue arc. Just beyond the stellar ring, there seems to be a second, this time redder, stellar ring, about 6″ across. Farther out, at a distance of about 34″, a ring rests at the end of a kpc-scale bar. The presence of the rings makes the A4 and B4 coefficients non zero. The position angle, ellipticity and the surface brightness profile are also irregular. There doesn't appear to be a stellar nucleus, although the presence of the dust makes this statement hard to quantify.

18. VCC 1692 (NGC 4570). This galaxy shows a thin, circum-nuclear stellar ring, centered on the nucleus (which appears resolved), extending just less than 2″ on either side and aligned with the main body of the galaxy. Although almost edge-on, the structure indeed appears to be a ring rather than a disk; an inner gap is apparent from the images. The ring is bluer than the surrounding galaxy. The galaxy is very elongated, with a thin, edge-on disk which appears to become slightly thicker towards the center, where it joins the main bulge.

19. VCC 1030 (NGC 4435). There is a small dust disk, about 8″ across, centered on the galaxy's center. The disk is inclined $\sim 16^\circ$ to the line of sight. Although similar, this disk is smaller and less structured than those in VCC 1154 and VCC 1532. Several regions within the disk are quite blue, probably due to star formation. This prevents an accurate dust correction, and the isophotes are not recovered within the inner 2″. Because of the dust, it is also impossible to assess the presence of a nucleus. The isophotes are visibly boxy in the inner ∼10″, switching to disky further out.

20. VCC 2000 (NGC 4660). The center is saturated in the $g-$band image. The galaxy is very elongated, but becomes boxy at a distance of about 6″ (along the major axis) from the center. At the corresponding distance along the minor axis (4″.5), to the South, there is a small, faint, very blue structure, resembling a nucleus with two spiral arms. The "arm" facing the nucleus of VCC 2000 is more extended and looser than the arm facing away. The entire structure is about 2″.5 across.

21. VCC 685 (NGC 4350). This is a very elongated system, with a large-scale edge-on stellar disk typical of S0 galaxies. The presence of the disk affects the B4 coefficient, which becomes positive beyond a few arcsec. There is a nuclear, nearly edge-on dust disk, about 4″ in diameter. The dust disk is surrounded by a blue stellar disk, extending perhaps 1″.5 beyond the edge of the dust disk. Dust, stellar, and outer disks are all aligned. In correcting for dust absorption, the color of the region underlying the dust disk has been assumed equal to the color of the surrounding stellar disk, although the correction is still not entirely successful. There is no obvious evidence for the presence of a nucleus from the color images or the surface brightness profiles (although this is not a secure conclusion, because of the presence of the dust). The vast majority of globular clusters are found in the equatorial plane of the galaxy, and are therefore likely associated with the large-scale disk.

22. VCC 1664 (NGC 4564). There appears to be a faint nucleus in the color image, although its presence is not obvious in the individual images. The galaxy becomes quite disky beyond 10″.

23. VCC 654 (NGC 4340). The galaxy is quite round within the inner 1″.7, beyond which it becomes stretched in the NortEast-SouthWest direction, due to the presence of an inner bar surrounded by a nuclear stellar ring. Beyond 6″, the galaxy is elongated in the East-West direction. The very innermost region (within 0″.5) is also elongated, in the same direction as the outer parts. From the color image, the innermost structure appears bluer than the main body of the galaxy. An outer stellar ring with semi-major axis of about 56″ bounds an outer bar; a small irregular galaxy lies along this ring about 40″ to the North-East of the center; it is possible that this is a disrupted satellite.

24. VCC 944 (NGC 4417). This galaxy has a thin edge-on blue stellar disk, aligned with the main body. There appears to be a faint nucleus, both from the color image and from the $g-$band surface brightness profile.

25. VCC 1938 (NGC 4638). The galaxy is visibly disky beyond a few arcsec. A thin, edge-on stellar disk seems to be embedded in the outer, thick disk of the galaxy. The latter does not extend all the way in, stopping at a distance of about 4″.5 from the center. There is a faint indication of two tightly wound dust spiral arms extending from the the disk, at a distance of 13″ from the center, although there is no feature associated with these structures in the color image. The latter do show, however, an inner, red disk about 12″ in radius. There is no obvious dust absorption associated with this disk in the individual images, and therefore this is probably a stellar feature. The color images also indicate the presence of a compact nucleus. In the isophotal analysis, the center seems to wonder, and was therefore held fixed. A fainter galaxy (possibly a nucleated dwarf elliptical) is seen about 100″ to the east, while a very red object is present about 17″ East of the nucleus.

26. VCC 1279 (NGC 4478). This galaxy is generally well behaved on large scales. There is no hint of the existence of a large-scale disk, but the isophotes become more elongated in the very innermost region. The color image betrays the existence of a small (less than 1″ in radius) blue stellar disk, which is seen almost edge-on and oriented along the major axis of the galaxy. The presence of a disk is also reflected in the B4 coefficient. From the surface brightness profile, it is possible that a compact nucleus exists, affecting the profile within the inner 1″or so, although the feature seen could also be attributable to the disk.

27. VCC 1720 (NGC 4578). Well behaved elliptical, with regular isophotes. Both the color image and the surface brightness profiles show evidence of a stellar nucleus.

28. VCC 355 (NGC 4262). Two dust filaments radiate away from the center in a spiral pattern, reaching out to a distance of about 4″. Other than that, the galaxy appears regular within this region. Beyond, the isophotes twist (from a position angle of about -30° to approximately +20°), and the isophotes become quite disky. Inspection of the images reveal the presence of a bar, aligned at a position angle of +10°and extending about 27″ from side to side. The bar appears slightly misaligned with respect to the main body of the galaxy at the same radius. The end of the bar has a "flattened" appearance, resembling a hammer, although there is no obvious indication of a ring spiral arms protruding from it. There is no obvious color feature associated with the bar. There might be a hint of a compact stellar nucleus from the surface brightness profiles.

29. VCC 1619 (NGC 4550). This galaxy is intermediate, as far as dust morphology is concerned, between the "dust filaments" types (e.g., M87 and NGC 4472) and the "large-scale dust disk" types (e.g., VCC 1154). Dust filaments radiate outwards from the center, but they have

larger optical depth compared to the ones seen in M87 or VCC 355, for instance. Although the filaments form a disk structure, this is not quite as organized as the disks seen in VCC 1154 or VCC 1532. The main dust filaments/lanes are confined within a 10″ from the center, but dust patches can be seen further out, up to a distance of 25″. The dust correction performs well, indicating that the galaxy's color within the dust region is similar to that of the neighboring areas. The surface brightness profile indicates the presence of a large nucleus.

30. VCC 1883 (NGC 4612). This galaxy resembles VCC 355, in that is shows a dramatic isophotal twist. In this case, however, there is no evidence of dust. The presence of a bar is not quite as obvious as it is in the case of VCC 355, but the galaxy isophotes become "stretched" at a distance of about 17″ from the center, as would be expected if a boxy, elongated component were superimposed to the main body of the galaxy. The "ends" of the bar are visible, albeit barely, in the individual images. The bar is misaligned with the main body of the galaxy, producing a 40° change in the position angle of the major axis. A stellar nucleus causes an inflection in the innermost 0″.2 of the surface brightness profile.

31. VCC 1242 (NGC 4474). This galaxy resembles VCC 685 but for the presence of dust. Very elongated system, with a large-scale edge-on stellar disk typical of S0 galaxies. The presence of the disk affects the B4 coefficient, which becomes positive beyond a few arcsec, and the galaxy appears bluer in the equatorial plane. A nucleus is visible in both of the individual images, and is reflected in the shape of the surface brightness profiles in the inner 0″.3. The galaxy has a significantly larger Globular Cluster (GC) system compared to galaxies in the same magnitude range.

32. VCC 784 (NGC 4379). The isophotes become slightly disky at a distance of approximately 10″ from the center, as shown by the B4 coefficient and ellipticity change between 10 and 20″. Unlike the case of VCC 1883 and VCC 355, there is no convincing evidence that a bar might be present, although the fact that the position angle changes (just as it does for VCC 1883 and VCC 355 where the bar sets in) is suggestive. The images and surface brightness profile are clearly affected by the presence of a nucleus in the inner 0″.2.

33. VCC 1537 (NGC 4528). This galaxy is in the same class as VCC 1883 and VCC 355 (and perhaps VCC 784 and VCC 778), but shows even more extreme properties. The bar is very prominent, and is misaligned relative to the major axis of the main body of the galaxy by about of 60°, with the bar almost aligned in the East-West direction. Ellipticity, position angle, A4 and B4 coefficients change abruptly where the bar sets in. The surface brightness in the main body of the galaxy changes abruptly at the radius corresponding to the edge of the bar; being fainter within the region swept by the bar than outside. There is no clear evidence for a nucleus, although the surface brightness profile is quite steep.

34. VCC 778 (NGC 4377). There are three small spiral galaxies at approximately 17″, 19″ and 31″ from the center of VCC 788; the largest galaxy is approximately 11″ across. The three galaxies are aligned approximately in the East-West direction; there is no obvious isophotal disturbance in VCC 778 at the radius where these galaxies are, and therefore the three spirals are probably part of a background group. All three galaxies were masked in fitting the isophotal parameters. This galaxy shows the same features seen in VCC 784: at radii between approximately 3″.5 and 8″, the isophotes twist, the ellipticity, the B4 and, especially, the A4 coefficients jump, as due to the presence of a misaligned bar (the misalignment here is about 20°), producing "diamond" shaped isophotes. The bar is not directly visible in the individual frames, but produces a discontinuity in the surface brightness profile.

35. VCC 1321 (NGC 4489). This galaxy shows a dramatic (almost 90°) isophotal twist which takes place abruptly at approximately 5″ from the center. However, unlike the case of VCC 1537, the twist is not accompanied by a change in the higher order coefficients, in fact the isophotes remain very regular all the way out. There is therefore no evidence that this twist is due to a bar.

36. VCC 828 (NGC 4387). The galaxy is visibly boxy beyond 1″, but otherwise it doesn't show evidence of structure. A nucleus is clearly visible from the individual frames and the surface brightness profiles.

37. VCC 1250 (NGC 4476). This galaxy harbors a nuclear, clumpy, dust disk, about 11″ in radius. The clumps are clearly organized in a spiral structure. The plane of the disk is inclined by about 20° to the line of sight; the North-West side of the disk is the closest. This disk is similar, but clumpier and smaller than the ones seen VCC 1154 or VCC 1532. The correction for dust performs better than in the case of VCC 1154 or VCC 1532, indicating that the change in the stellar population embedded in the disk (relative to the one surrounding it), is not as extreme as in those galaxies. Several blue clumps, organized in an almost complete arc structure, are however clearly visible within the disk, and the isophotal parameter within the inner 10″ should be interpreted with caution. There is clear indication of the presence of a nucleus from both the individual and the color image, and from the surface brightness profiles. The color of the nucleus cannot be assessed because of the presence of dust. The nucleus appears to be offset by just over 1″ in the North direction relative to the center of the dust disk (the disk's major axis is aligned in the North-NorthEast direction). The isophotal center is not very stable even in the outer regions, varying by as much as 0″.1 between subsequent isophotes; but it does seem to be consistent with the location of the nucleus. The isophotes seem quite regular, at least in the outer region.

38. VCC 1630 (NGC 4551). From the individual images, in the very innermost region, it is barely possible to make out the presence of a faint stellar disk, possibly flaring out at the edges. This is reflected in the abrupt change of the A4, B4 coefficients in the inner 0″.1. There is a clear resolved nucleus.

39. VCC 1146 (NGC 4458). The innermost isophotes appear quite disky, as reflected in the negative B4 coefficient in the inner 0″.2. The ellipticity increases steadily towards the center. The galaxies hosts a large, bright nucleus.

40. VCC 1025 (NGC 4434). This galaxy is quite

round, although it becomes visibly more elongated in a narrow radial range around $\sim 8''$. There are no features seen in the color image. There is a hint of the presence of a large nucleus from a "break" in the surface brightness profiles around $1''$.

41. VCC 1303 (NGC 4483). This galaxy appears to have two smooth spiral arms, first noticeable extending from the central bulge at a distance of approximately $7''$ from the galaxy's center. The arms extend in the East-West direction at first (the major axis of the galaxy is at a position angle of 60°), then bend towards North in a clockwise fashion. The position angle, B4 and A4 coefficients all change outwards of $10''$ because of the arms. There are no features visible in the color image.

42. VCC 1913 (NGC 4623). This galaxy is somewhat similar to VCC 1630 in that it shows (more clearly in this case) the presence of a thick, edge-on nuclear stellar disk, about $1''$ in radius. From the color image, the disk appears slightly bluer than the host galaxy. A nucleus is quite apparent in the individual images, and seems to affect the surface brightness profile in the inner $0''.3$. At larger scales, the galaxy appears to have a "structure within the structure" morphology: within the inner $7''$, the light is dominated by a boxy bulge. Beyond, there appears to be a disky (or at least highly elongated) "halo" or disk. The transition between the two structures is quite abrupt and can be seen as a discontinuity in the surface brightness profile in the individual images. All of the structures share the same major axis.

43. VCC 1327 (NGC 4486A). The galaxy is tidally truncated due to interactions with M87, which projects only $7'.5$ away. Small, faint galaxy with a bright foreground star nearby. An edge-one dust disk is clearly visible.

44. VCC 1125 (NGC 4452). This galaxy is an edge-on S0. There seem to be four separate components: a resolved nucleus, an inner, thin stellar disk, confined within $2''$ from the center, a "middle" thicker, stellar disk, extending out to distances of about $17''$ from the center, and an outer, thinner stellar disk, which is highly flattened. An inner bulge seems to be almost an extension of the middle disk. The smaller inner disk is bluer in color than the outer disks; there is no appreciable color difference between the middle and the outer disk and the bulge of the galaxy. The presence of the nucleus is very clear from the surface brightness profile.

45. VCC 1475 (NGC 4515). The galaxy shows a nucleus, surrounded by an edge-on blue disk, which flares out slightly at the end. The disk extends for a total of about $4''$. The nucleus is visible in the surface brightness profile as well.

46. VCC 1178 (NGC 4464). A compact nucleus is clearly visible in the color image, but barely discernible in the surface brightness profiles. The isophotes appear regular.

47. VCC 1283 (NGC 4479). A clear nucleus is visible from the color image and the surface brightness profile. The isophotes appear quite regular, although there seems to be a faint bar extending out to about $30''$.

48. VCC 1261 (NGC 4482). This galaxy hosts a resolved nucleus. The isophotes appear regular. Several faint background galaxies are seen within $50''$.

49. VCC 698 (NGC 4352). The galaxy is quite disky within $1''$, becoming boxy further out, and then disky again outside $10''$. The inner disk (which is blue) and a resolved nucleus are visible in the color image; the nucleus is noticeable in the surface brightness profile as well.

50. VCC 1422. This galaxy has a bright, resolved nucleus, clearly dominating the surface brightness profile. The isophotes appear regular. The color image shows possible evidence of a large filamentary dust structure about $26''$ South-West of the nucleus, distributed azimuthally within a 90° radius.

51. VCC 2048. This galaxy has a bright nucleus, dominating the surface brightness profile and clearly visible in the color image. The nucleus is surrounded by a thin edge-on stellar disk, as a consequence of which the isophotes are very disky.

52. VCC 1871. Unlike other galaxies in the same magnitude range, this is quite round, perhaps because of inclination effects. The isophotes are regular. A bright resolved nucleus is clearly visible in the surface brightness profiles and color image.

53. VCC 9. This galaxy has fainter surface brightness than galaxies in the same magnitude range, and a flat core. There are two bright clusters within $2''$ from the center, but nothing at the center of the isophotes.

54. VCC 575 (NGC 4318). This galaxy shows a clear structure in the stellar population. At a distance of about $4''$ from the center, a stellar disk or wide ring sets in; the ring is brighter than the region within it, causing a kink in the surface brightness profile. It is possible that the ring is actually the result of a spiral structure, although the spiral "arms" do not appear to extend all the way to the center of the galaxy. The ring might be similar to the structure seen edge-on in other galaxies, for instance VCC 1938, where an outer "disk" is present but does not extend all the way to the center. Although there is no structure associated with the ring/truncated disk in the color image, this does show a thin, edge-on red disk extending approximately $2''.5$ across the nucleus.

55. VCC 1910. The surface brightness profile is dominated by the stellar nucleus, which is brighter than any globular cluster within the field. The isophotes are regular. There is a very red globular cluster just over $2''$ West of the nucleus.

56. VCC 1049. From the brightness profile there doesn't seem to be evidence of a separate nuclear component, although the profile is quite steep and the galaxy becomes significantly bluer towards the center. The isophotes are fairly regular. There are two small, faint irregular/spiral galaxies, one $20''$ to the South-East, the other $19''$ to the North, probably both in the background.

57. VCC 856. This galaxy shows a clear face-on spiral pattern. The arms are quite wide, smooth and regular. The center of the galaxy has a bright, resolved nucleus. There is no evidence of a bulge component. This galaxy would be better classified as a dwarf spiral.

58. VCC 140. A nucleus is clearly visible both in the color image and in the surface brightness profiles. The isophotes are regular. Several faint background galaxies

are seen within the field.

59. VCC 1355. The galaxy has a bright, resolved nucleus. The isophotes are quite round and regular.

60. VCC 1087. The nucleus is marginally resolved, the isophotes appear regular.

61. VCC 1297 (NGC 4486B). Lauer et al. 1996 identified a double nucleus, separated by 12 pc (0.″15), based on deconvolved WFPC2 images of this galaxy. The two nuclei are not immediately apparent in the ACS images, although the galaxy is quite disky within the inner 100 pc, with this trend persisting all the way to the center, and the profile is slightly asymmetric in the inner 40 pc. Beyond about 10″, the surface brightness profile is clearly truncated by interaction with M87, which projects only 7.′3 away.

62. VCC 1861. Like other galaxies in this magnitude range (with the exception of VCC 1297) this galaxy has a bright, resolved nucleus superimposed to a flat core. The isophotes are quite round and regular.

63. VCC 543. A resolved nucleus dominates the surface brightness profile. This galaxy is quite elongated, but the isophotes are regular.

64. VCC 1431. Round galaxy with a resolved nucleus. There are three red, faint irregular galaxies between 9″ and 12″ to the North-East; probably background. The isophotes are regular.

65. VCC 1528. This galaxy has a bright, very compact nucleus. The isophotes are regular.

66. VCC 1695. This galaxy has a bright nucleus. The isophotes are regular, there is no evidence of dust, although the residual images show evidence of a large-scale spiral structure. In the color image, there seems to be an elongated, large, red, faint feature about 20″ to the East, although this is not visible in the single images.

67. VCC 1833. Unlike galaxies in a similar magnitude range, this galaxy does not appear to have a distinct nucleus. The isophotes are regular.

68. VCC 437. This galaxy has a bright, resolved nucleus. The isophotes are regular. A background galaxy cluster is visible in the frame.

69. VCC 2019. This galaxy has a bright nucleus, and low surface brightness. Several bright clusters are seen, and a small but resolved object is detected about 12″ to the North.

70. VCC 33. This galaxy has a bright nucleus dominating the surface brightness profile. The globular cluster population is small. An extremely red object (not obviously extended) is seen about 4″ East of the nucleus.

71. VCC 200. This galaxy has a bright nucleus dominating the surface brightness profile.

72. VCC 571. The center of this galaxy is crossed by a dust lane running in the North-West direction (approximately along the major axis of the galaxy). The dust lane extends out to about 8″ (becoming wider and more diffuse with increasing distance from the center) in the South-East direction, and just over 1″ in the North-West direction. More wisps are seem further out, especially on the North-West side. The correction for dust performs well. Several blue star clusters are seen near the center (although not along the dust lane itself), probably indicative of recent star formation.

73. VCC 21. Elongated system, may be better classified as a dwarf irregular/dwarf elliptical transition object. There are several bright clusters near, but none exactly at, the center.

74. VCC 1488. Elongated system. There is a small spiral galaxy, about 6″ across, 8″ to the South; this galaxy has been masked in fitting the isophotes. An unconstrained fit to the isophotes runs into problems because of the low gradient in the surface brightness profile, but between 0.″5 and 5″ the isophotes are centered very accurately on the nucleus. ELLIPSE was therefore run over a more extended radial range by fixing the position of the center to that of the nucleus.

75. VCC 1779. This galaxy might be best classified as a dIrr/dE transition object. Dust filaments are seen radiating from the center outwards within the inner 6″. From a visual inspection of the image, there appears to be very few objects which could be identified as GCs; three of these are near the center, although none is at the nuclear position. A small spiral galaxy is seen about 17″ to the South-West.

76. VCC 1895. Highly elongated, faint elliptical. The nucleus is clearly visible and may be slightly elongated in the same direction as the major axis of the galaxy.

77. VCC 1499. This galaxy should be classified as a dIrr/dE. There are several bright clusters and blue associations close to the center, although there doesn't appear to be a proper nucleus, and there is no convincing evidence of dust. The center of the isophotes drifts to the East as the radius is increased.

78. VCC 1545. This galaxy has a bright, resolved nucleus. The galaxy is fairly round, the isophotes are regular. The galaxy has a fairly substantial population of bright globular clusters.

79. VCC 1192 (NGC 4467). This galaxy is a close companion of M49, which lies 4.′2 away, outside the WFC frame to the East; the outer surface brightness profile is tidally truncated, the ellipticity is also affected. The surface brightness profile in the center is brighter (by one to two magnitudes) than that of galaxies in the same magnitude range. A resolved nucleus is clearly present in the color images, as well as in the surface brightness profiles. There is a small blue cluster within 0.″1 from the nucleus, a second about 0.″9 to the South-East.

80. VCC 1857. Very low surface brightness, elongated system. There are several faint clusters in the frame, and a very bright one about 6″ West of the center. The position of the center was determined by block averaging and then contouring the images, and was held fixed in fitting the isophotes.

81. VCC 1075. The isophotal center is consistent with the location of a bright cluster, which is therefore identified as the nucleus. The central position is held fixed at the nuclear location in the fitting the isophotes.

82. VCC 1948. Elongated system. Although there are some faint clusters around the center, none appears to be at the isophotal center.

83. VCC 1627. This galaxy has brighter surface brightness than galaxies in the same magnitude range. As a consequence, the nucleus is not as prominent in the sur-

face brightness profile, although it is clearly visible in the color image. The galaxy is quite round; there are no signs of disturbance in the isophotes. A very red cluster is seen about 6″ West of the nucleus; otherwise the galaxy has a small GC system compared to galaxies in the same magnitude range.

84. VCC 1440. This galaxy has brighter surface brightness than galaxies with comparable B_T, and a large number of bright globular clusters for a galaxy of this magnitude. A bright, resolved nucleus is clearly present.

85. VCC 230. This galaxy has a bright nucleus. The galaxy is quite round, and has what appears to be a significant globular cluster population. The isophotes are regular.

86. VCC 2050. Very elongated system with a central, faint nucleus. The galaxy appears regular. A very red cluster is seen just over 7″ South of the nucleus.

87. VCC 1993. The g and $z-$band images show a faint nucleus, which does not affect significantly the surface brightness profile. From a visual inspection of the image, there are very few objects which could be identified as globular clusters.

88. VCC 751. Fairly elongated galaxy with a bright nucleus. The isophotes appear regular. There is a very red background galaxy about 12″ East of the nucleus.

89. VCC 1828. The nucleus is quite prominent.

90. VCC 538 (NGC 4309A). Round system, with a bright, resolved nucleus. There is a bright spiral galaxy about 90″ to the South.

91. VCC 1407. This galaxy has a bright nucleus; the galaxy has regular isophotes. There seems to be a large population of globular clusters. A very blue and small (less than 0″.2 across) elongated feature is seen about 1″.5 East of the nucleus.

92. VCC 1886. The brightest cluster/nucleus in the frame appears to be at the location of the isophotal center; a second, almost as bright cluster is 4″.7 to the North-East.

93. VCC 1199. The galaxy is a close companion of M49, which lies only 4′.5 away, and is a prime candidate for galaxy harassment. Its surface brightness is brighter than galaxies in the same magnitude range, and is tidally truncated in the outer regions. The nucleus looks elongated (along the major axis of the galaxy), furthermore, there seems to be, from the g and $z-$band images, a very thin edge-on disk also aligned with the galaxy major axis, extending less than 1″ on either side of the center. The residual images also show evidence of a large-scale spiral pattern.

94. VCC 1743. Very low surface brightness elongated galaxy, with a very faint nucleus. The nucleus seems to have the same color as the surrounding galaxy.

95. VCC 1539. This galaxy has a large number of bright globular clusters for a galaxy of this magnitude. The galaxy is very round, has a bright nucleus, and becomes increasingly bluer towards the center.

96. VCC 1185. Small, round system, with a bright nucleus. The isophotes are regular.

97. VCC 1826. This galaxy has a very sparse cluster system. The nucleus is quite prominent.

98. VCC 1512. This is a dIrr/dE transition object. There is a loose association of blue stars at the center. It is not clear whether this galaxy has dust or whether the darker areas seen towards the center are simply an illusion created by the presence of the bright blue associations. There doesn't seem to be a proper nucleus.

99. VCC 1489. The light is dominated by a bright, resolved nucleus.

100. VCC 1661. This galaxy has a bright, resolved nucleus. The galaxy appears quite round. The isophotes are regular.

It is a pleasure and a privilege to thank Dr. Sidney van den Bergh for sharing his knowledge and expertise. We are indebted to Dr. Peter Stetson for help in generating the ACS/WFC PSFs used in this paper. Special thanks go to Dr. Alister Graham and the anonymous referee for the helpful comments and suggestions. Support for program GO-9401 was provided through a grant from the Space Telescope Science Institute, which is operated by the Association of Universities for Research in Astronomy, Inc., under NASA contract NAS5-26555. P.C. acknowledges additional support provided by NASA LTSA grant NAG5-11714. M.M. acknowledges additional financial support provided by the Sherman M.Fairchild foundation. D.M. is supported by NSF grant AST-020631, NASA grant NAG5-9046, and grant HST-AR-09519.01-A from STScI. M.J.W. acknowledges support through NSF grant AST-0205960. This research has made use of the NASA/IPAC Extragalactic Database (NED) which is operated by the Jet Propulsion Laboratory, California Institute of Technology, under contract with the National Aeronautics and Space Administration, and the HyperLeda database, http://www-obs.univ-lyon1.fr/hypercat/.

REFERENCES

Anderson, K.S.J., Baggett, S.M., & Baggett, W.E. 2004, AJ, 127, 2085
Babul, A., & Rees, M.J. 1992, MNRAS, 255, 346
Baggett W.E., Baggett S.M., Anderson K.S.J. 1996, in ASP Conf. Ser. 91, Barred Galaxies, eds Buta R., Crocker D.A., Elmegreen B.G., (San Francisco: ASP), 91
Baggett W.E., Baggett S.M., Anderson K.S.J. 1998, AJ, 116, 1626
Barazza, F.D., Binggeli, B., & Jerjen, H. 2002, A&A, 391, 823
Baum, W.A. 1959, PASP, 71, 106
Bender, R., Doebereiner,S., & Moellenhoff, C. 1987, A&A, 177, 53
Bender, R. 1988, A&A, 202, 5
Bender, R., Surma, P., Doebereiner, S., Moellenhoff, C., & Madejsky, R. 1989, A&A, 217, 35
Bernardi, M., Sheth, R.K., Nichol, R.C., Schneider, D.P., & Brinkmann, J. 2005, AJ, 129, 61
Binggeli, B., Sandage, A., & Tarenghi, M. 1984, AJ, 89, 64
Binggeli, B. 1994, in Panchromatic View of Galaxies, ed. G. Hensler, C. Theis, & J. Gallagher (Gif-sur-Yvette: Ed. Frontires), 173
Binggeli, B., Sandage, A., & Tammann, G.A. 1985, AJ, 90, 1681
Blakeslee, J.P, Lucey, J.R., Tonry, J.L., Hudson, M.J., Narayanan, V.K., & Barris, B.J. 2002, MNRAS, 330, 443
Blakeslee, J.P., et al. 2003, ApJ, 589, 693
Bower, R.G., Lucey, J.R., & Ellis, R.S. 1992, MNRAS, 254, 601
Bruzual, G., & Charlot, S. 2003, MNRAS, 344, 1000

Busarello G., Capaccioli M., D'Onofrio M., Longo G., Richter G., Zaggia S. 1996, A&A, 314, 32
Byun, Y.I., et al. 1996, AJ, 111, 1889
Caon, N., Capaccioli, M., & Rampazzo, R. 1990, A&AS, 86, 429
Caon, N., Capaccioli, M., & D'Onofrio, M. 1994, A&AS, 106, 199
Capaccioli, M., 1989, in The world of galaxies; New York, Springer-Verlag, p. 208
Cardelli, J.A., Clayton, G.C., & Mathis, J.S. 1989, ApJ, 345, 245
Carollo, C.M., Franx, M., Illingworth, G.D., & Forbes, D. 1997, ApJ, 481, 710
Conselice, C.J., Gallagher, J.S., III, & Wyse, R.F.G. 2001, ApJ, 559, 791
Côté, P., Blakeslee, J.P., Ferrarese, L., Jordán, A., Mei, S., Merritt, D., Milosavljević, M., Peng, E.W., Tonry, J.L., & West, M.J. 2004, ApJS, 153, 223 (Paper I)
Côté, P., Piatek, S., Ferrarese, L., Jordán, A., Merritt, D., Peng, E.W., Haşegan, M., Blakeslee, J.P., Mei, S., West, M.J., Milosavljević, M., & Tonry, J.L. 2005, ApJ, submitted (Paper VIII).
Crane, P., et al. 1993, AJ, 106, 1371
de Jong, R.S., & van der Kruit, P.C. 1994, A&AS, 106, 451
Dekel, A., & Silk, J. 1986, ApJ, 303, 39
de Koff, S., et al. 2000, ApJS, 129, 33
De Rijcke, S., Dejonghe, H., Zeilinger, W.W., & Hau, G.K.T. 2003, A&A, 400, 119
de Vaucouleurs, G. 1948, Ann. d'Astrophys., 11, 247
Djorgovski, S. 1992, in Morphological and Physical Classification of Galaxies, ed. G. Longo et al. , Kluwer, Dordrecht, p.337
Eliche-Moral, M.C., Balcells, M., Aguerri, J.A.L. ,Gonzalez-Garcia, A.C. 2005, The Many Scales in the Universe, in press (astro-ph/0501376)
Drinkwater, M.J., Gregg, M.D., & Colless, M. 2001, ApJ, 548, 139
Elmegreen, D.M., Elmegreen, B.G., Chromey, F.R., & Fine, M.S. 2000, AJ, 120, 733
Emsellem, E., Bacon, R., Monnet, G., Poulain, P. 1996, A&A, 312, 777
Emsellem, E., Goudfrooij, P., & Ferruit, P. 2003, MNRAS, 345, 1297
Erwin, P., Beltran, J.C.V., Graham, A.W., & Beckman, J.E. 2003, ApJ, 597, 929
Erwin, P. 2004, å, 415, 941
Faber, S.M. 1973, ApJ, 179 423
Faber, S.M., et al. 1997, AJ, 114, 1771
Ferrarese, L., van den Bosch, F.C., Ford, H.C., Jaffe, W., & O Connell, R.W. 1994, AJ, 108, 1598
Ferrarese, L., Ford, H.C., & Jaffe, W. 1996, ApJ, 470, 444
Ferrarese, L., & Ford, H.C. 2005, Space Science Rev., 116, 523
Fisher, D., Franx, M., & Illingworth, G. 1996, ApJ, 459, 110
Forbes, D., Franx, M., & Illingworth, G. 1995, AJ, 109, 1988
Freedman, W.L. et al. 2001, ApJ, 553, 47
Freeman, K.C. 1970, ApJ, 160, 811
Freeman, K.C. 1975, In "Dynamics of Stellar Systems", Proceedings from IAU Symposium no. 69, editor Avram Hayli. Dordrecht; Boston: D. Reidel Pub. Co., p.367
Fukugita, M., Shimasaku, K., & Ichikawa, T. 1995, PASP, 107, 945
Gebhardt, K., et al. 1996, AJ, 112, 105
Geha, M., Guhathakurta, P., & van der Marel, R.P. 2003, AJ, 126, 1794
Goldreich, P., & Tremaine, S. 1979, ApJ, 233, 857
Goudfrooij, P., Hansen, L., Jørgensen, H.E., & Norgaard-Nielsen, H.U. 1994, A&AS, 105, 341
Graham, A.W. 2001, AJ, 121, 820
Graham, A.W., Erwin, P., Trujillo, I, & Asensio, R.A. 2003, AJ, 125, 2951
Graham, A.W., & Guzmán, R. 2003, AJ, 125, 2936
Graham, A.W. 2004, ApJ, 613, 33
Graham, A.W., & Driver, S.P. 2005, PASA, 22, 118
Harms, R.J., et al. 1994, ApJ, 435, L35.
Haşegan, M., Jordán, A., Côté, P., Djorgovski, S.G., McLaughlin, D.E., Blakeslee, J.P., Mei, S., West, M.J., Peng, E.W., Ferrarese, L., Milosavljević, M., Tonry, J.L., & Merritt, D. 2005, ApJ, 627, 203
Hernquist, L. 1990, ApJ, 356, 359
Hilker, M., Kissler-Patig, M., Richtler, T., Infante, L., Quintana, H. 1999, A&AS, 134,59
Hyorth, J., & Madsen J. 1995, ApJ, 445, 55
Jaffe, W. 1983, MNRAS, 202, 995
Jaffe, W., Ford, H.C., O Connell, R.W., van den Bosch, F.C., & Ferrarese, L. 1994, AJ, 108, 1567
Jarrett, T. H., Chester, T., Cutri, R., Schneider, S. E., & Huchra, J. P. 2003, AJ, 125, 525
Jedrzejewski, R.I. 1987, MNRAS, 226, 747
Jerjen, H., & Binggeli, B. 1997, in ASP Conf. Ser. 116, The Nature of Elliptical Galaxies, ed. M. Arnaboldi, G.S. Da Costa, & P. Saha (San Francisco: ASP), 239
Jerjen, H., Kalnajs, A., & Binggeli, B. 2000, A&A, 358, 845
Jerjen, H., Kalnajs, A., & Binggeli, B. 2001, in ASP Conf. Ser. 230, Galaxy Disks and Disk Galaxies, ed. J.G. Funes, & E.M. Corsini (San Francisco: ASP), 239
Jordán, A., Blakeslee, J.P., Peng, E., Côté, P., Ferrarese, L., Mei, S., Merritt, D., Milosavljević, M., Tonry, J.L., & West, M.J. 2004a, ApJS, 154, 509 (Paper II)
Jordán, A., Côté, P., Ferrarese, L., Blakeslee, J.P., Mei, S., Merritt, D., Milosavljević, M., Peng, E., Tonry, J.L., & West, M.J. 2004b, ApJ, 613, 279
Jordán, A., Côté, P., Blakeslee, J.P., Ferrarese, L., McLaughlin, D.E., Mei, S., Peng, E.W., Tonry, J.L., Merritt, D., Milosavljević, M., Sarazin, C.L., Sivakoff, G.R., West, M.J. 2005, ApJ, 634, 1002
Jørgensen, I., & Franx, M. 1994, ApJ, 433, 553
King, I.R. 1966, AJ, 71, 64
King, I.R. 1978, ApJ, 222, 1
Kodama, T., & Arimoto, N. 1997, AJ, 320, 41
Kodama, T., Arimoto, N., Barger, A.J., Aragón-Salamanca, A. 1998, A&A, 334, 99
Kormendy, J. 1984, ApJ, 286, 116
Kormendy, J. 1985, ApJ, 295, 73
Lambas, D.G., Maddox, S.J., & Loveday, J. 1992, MNRAS, 258, 404
Laine, S., van der Marel, R.P., Rossa, J., Hibbard, J.E., Mihos, J.C., Böker, T., & Zabludoff, A.I.B. 2003, AJ, 126, 2717
Lauer, T.R. 1985, ApJ, 292, 104
Lauer, T.R., et al. 1995, AJ, 110, 2622
Lauer, T.R., et al. 1996, AJ, 471, L79
Lauer, T.R., et al. 2002, AJ, 124, 1975
Lauer, T.R., et al. 2005, AJ, 129, 2138
Lin, D.N.C., & Faber, S.M. 1983, ApJ, 266, L21
Mastropietro, C., Moore, B., Mayer, L., Debattista, V.P., Piffaretti, R., & Stadel, J. 2005, MNRAS, in press
Mateo, M. 1998, ARA&A, 36, 435
McLaughlin, D.E. 2000, ApJ, 539, 618
Mei, S., Blakeslee, J.P., Tonry, J.L., Jordán, A., Peng, E.W., Côté, P., Ferrarese, L., Merritt, D., Milosavljević, M., & West, M.J 2005, ApJS, 156, 113
Mei, S., Blakeslee, J.P., Tonry, J.L., Jordán, A., Peng, E.W., Côté, P., Ferrarese, L., West, M.J., Merritt, D., & Milosavljević, M. 2005, ApJ, 625, 121
Merritt, D., Navarro, J.F., Ludlow, A., & Jenkins, A. 2005a, ApJ, 624, L85
Michard, R. 1985, A&AS, 59, 205
Michard, R. 1994, A&A, 288, 401
Michie, R.W. 1963, MNRAS, 125, 127
Milosavljević, M., & Merritt, D. 2001, ApJ, 563, 34
Milosavljević, M., Merritt, D., Rest, A., & van den Bosch, F.C. 2002, MNRAS, 331, 51
Moore, B., Lake, G., & Katz, N. 1998, ApJ, 495, 139
Nelder, J.A., & Mead, R. 1965, Comput.J., 7, 308
Nieto J.-L., Poulain P., Davoust E., Rosenblatt P. 1991, A&AS88, 559
Nieto, J.-P., & Bender, R. 1989, A&A, 215, 266
Nieto, J.-L., Poulain, P., Davoust, E., & Rosenblatt, P. 1991, A&AS, 88, 559
Norman, C., Sellwood, J.A., & Hasan, H. 1996 ApJ, 462, 114
Pavlovsky, C., et al. 2004, ACS Instrument Handbook, Version 5.0, (Baltimore: STScI)
Pedraz, S., Gorgas, J., Cardiel, N., Sanchez-Blazquez, P., & Guzman, R. 2002, MNRAS, 332, L59
Peng, C.Y., Ho, L.C., Impey, C.D., Rix, H.-W. 2002, AJ, 124, 266
Peng, E.W., Jordán, A., Côté, P., Blakeslee, J.P., Ferrarese, L., Mei, S., West, M.J., Merritt, D., Milosavljević, M., & Tonry, J.L. 2005a, ApJ, in press
Peng, E.W., Jordán, A., Côté, P., Blakeslee, J.P., Ferrarese, L., Mei, S., West, M.J., Merritt, D., Milosavljević, M., & Tonry, J.L. 2005b, ApJ, in press
Poggianti, B.M., et al. 2001, ApJ, 562, 689

Prugniel, P., Zasov, A., Busarello, G., & Simien F. 1997, A&AS127, 117
Prugniel, P., & Simien, F. 1997, A&A, 321, 111
Quillen, A.C., Bower, G.A., & Stritzinger M. 2000 ApJS, 128, 85
Rangarajan, F.V.N., White, D.A., Ebeling, H., Fabian, A.C. 1995, MNRAS, 277, 1047
Ravindranath, S., Ho, L.C., Peng, C.Y., Filippenko, A.V., & Sargent, W.L.W. 2001, AJ, 122, 653
Rest, A., van den Bosch, F.C., Jaffe, W., Tran, H., Tsvetanov, Z., Ford, H.C., Davies, J., & Schafer, J. 2001, AJ, 121, 2431
Rix, H.-W., & White, S.D.M. 1990, ApJ, 362, 52
Rix, H.-W., & White, S.D.M. 1992, MNRAS, 254, 389
Rood, H.J. 1965, AJ, 70, 689
Sandage, A., Freeman, K.C., & Stokes, N.R. 1970, ApJ, 160, 831
Sandage, A., Binggeli, B., & Tammann, G.A. 1985, AJ, 90, 1759
Sandage, A., & Bedke, J. 1994, The Carnegie Atlas of Galaxies, Vol. 1
Schlegel, D.J., Finkbeiner, D.P., & Davis, M. 1998, ApJ, 500, 525
Schweizer, F. 1979, ApJ, 233, 23
Scorza C., Bender R., Winkelmann C., Capaccioli M., & Macchetto F.D. 1998, A&AS, 131, 265
Scorza, C., & van den Bosch, F.C. 1998, MNRAS, 300, 469
Secker, J., Harris, W.E., & Plummer, J.D. 1997, PASP, 109, 1377
Seifert W., Scorza C. 1996, A&A, 310, 75
Sérsic, J.-L. 1968, Atlas de Galaxias Australes (Córdoba: Obs. Astron., Univ. Nac. Córdova)
Sirianni et al. 2005, PASP, in press
Stickel, M., Bregman, J.N., Fabian, A.C., White, D.A., Elmegreen, D.M. 2003, A&A, 397, 503
Tan, J.C., & Blackman, E.G. 2005, MNRAS, in press (astro-ph/0409413)
Temi, P., Brighenti, F., Mathews, W.G., & Bregman, J.D. 2004, ApJS, 151, 237
Toomre, A. 1969, ApJ, 158, 899
Tonry, J.L., Dressler, A., Blakeslee, J.P., Ajhar, E.A., Fletcher, A.B., Luppino, G.A., Metzger, M.R., & Moore, C.B. 2001, ApJ, 546, 681
Tran, H.D., Tsvetanov, Z., Ford, H.C., Davies, J., Jaffe,W., van den Bosch, F.C., & Rest, A. 2001, AJ, 121, 2928
Trujillo, I., Erwin, P., Asensio Ramos, A., & Graham, A.W. 2004, AJ, 127
van den Bergh, S. 1994, AJ, 107, 153
van den Bosch, F.C., Ferrarese, L., Jaffe, W., Ford, H.C., & O Connell, R.W. 1994, AJ, 108, 1579
van den Bosch, F.C., & Emsellem, E. 1998, MNRAS, 298, 267
van der Marel, R. 1991, MNRAS, 253, 710
van der Marel, R.P., & van den Bosch, F.C. 1998, AJ116, 2220
van Dokkum, P.G., & Franx, M. 1995, AJ, 110, 2027
van Zee, L., Skillman, E.D., & Haynes, M.P. 2004, AJ, 128, 121
Verdoes Kleijn, G.A., Baum, S.A., de Zeeuw, P.T., O'Dea, C.P. 1999, AJ, 118, 2592
White, D.A., Fabian, A.C., Forman, W., Jones, C., & Stern, C. 1991, ApJ, 375, 35
White, S.D.M., & Frenk, C.S. 1991, ApJ, 379, 52
Young, C.K., & Currie, M.J. 1994, MNRAS, 268, L11

Table 1. Global Morphological Properties of Program Galaxies.

ID	VCC	RA (J2000) (NED)	Dec (J2000) (NED)	B_T (mag)	J (mag)	H (mag)	K_s (mag)	$E(B-V)$ (mag)	v_{sys} (km s^{-1})	Type (NED)	Other Names
1	1226	12:29:46.79	+08:00:01.5	9.31	6.39 ± 0.02	5.75 ± 0.02	5.51 ± 0.02	0.022	997±7	E2/S0$_1$(2)	M49, N4472
2	1316	12:30:49.42	+12:23:28.0	9.58	6.83 ± 0.02	6.16 ± 0.02	5.90 ± 0.02	0.023	1307±7	E0	M87, N4486
3	1978	12:43:39.66	+11:33:09.4	9.81	6.76 ± 0.02	6.08 ± 0.02	5.83 ± 0.02	0.026	1117±6	S0$_1$(2)	M60, N4649
4	881	12:26:11.74	+12:56:46.4	10.06	7.19 ± 0.02	6.51 ± 0.02	6.28 ± 0.02	0.029	-244±5	S0$_1$(3)/E3	M86, N4406
5	798	12:25:24.04	+18:11:25.9	10.09	7.17 ± 0.02	6.51 ± 0.02	6.26 ± 0.02	0.030	729±2	S0$_1$(3) pec	M85, N4382
6	763	12:25:03.72	+12:53:13.2	10.26	7.26 ± 0.02	6.59 ± 0.02	6.35 ± 0.02	0.041	1060±6	E1	M84, N4374
7	731	12:24:28.20	+07:19:03.0	10.51	7.71 ± 0.02	7.03 ± 0.02	6.80 ± 0.02	0.021	1243±6	E3	N4365
8	1535	12:34:03.10	+07:41:59.0	10.61	7.55 ± 0.02	6.79 ± 0.02	6.55 ± 0.02	0.021	448±8	S0$_3$(6)	N4526
9	1903	12:42:02.40	+11:38:48.0	10.76	7.77 ± 0.02	7.09 ± 0.02	6.87 ± 0.02	0.032	410±6	E4	M59, N4621
10	1632	12:35:39.82	+12:33:22.6	10.78	7.78 ± 0.02	7.09 ± 0.02	6.86 ± 0.02	0.041	340±4	S0$_1$(0)	M89, N4552
11	1231	12:29:48.87	+13:25:45.7	11.10	8.18 ± 0.02	7.51 ± 0.02	7.27 ± 0.02	0.028	2244±2	E5	N4473
12	2095	12:52:56.00	+11:13:53.0	11.18	8.36 ± 0.02	7.63 ± 0.02	7.45 ± 0.02	0.022	984±41	S0$_1$(9)	N4762
13	1154	12:29:00.03	+13:58:42.9	11.37	8.19 ± 0.01	7.49 ± 0.01	7.21 ± 0.01	0.045	1210±16	S0$_3$(2)	N4459
14	1062	12:28:03.90	+09:48:14.0	11.40	8.32 ± 0.02	7.59 ± 0.02	7.38 ± 0.02	0.022	532±8	SB0$_1$(6)	N4442
15	2092	12:52:17.50	+11:18:50.0	11.51	8.48 ± 0.02	7.80 ± 0.02	7.58 ± 0.02	0.032	1377±15	SB0$_1$(5)	N4754
16	369	12:19:45.42	+12:47:54.3	11.80	8.86 ± 0.01	8.16 ± 0.02	7.94 ± 0.02	0.047	1009±13	SB0$_1$	N4267
17	759	12:24:55.50	+11:42:15.0	11.80	8.71 ± 0.01	8.03 ± 0.02	7.81 ± 0.02	0.036	943±19	SB0$_2$(r)(3)	N4371
18	1692	12:36:53.40	+07:14:47.0	11.82	8.68 ± 0.01	8.00 ± 0.01	7.76 ± 0.01	0.022	1730±13	S0$_1$(7)/E7	N4570
19	1030	12:27:40.49	+13:04:44.2	11.84	8.45 ± 0.01	7.28 ± 0.01	7.39 ± 0.02	0.022	801±10	SB0$_1$(6)	N4435
20	2000	12:44:31.95	+11:11:25.1	11.94	9.14 ± 0.01	8.47 ± 0.01	8.25 ± 0.01	0.034	1083±4	E3/S0$_1$(3)	N4660
21	685	12:23:57.90	+16:41:37.0	11.99	8.80 ± 0.01	8.07 ± 0.01	7.86 ± 0.01	0.028	1241±19	S0$_1$(8)	N4350
22	1664	12:36:26.86	+11:26:20.6	12.02	8.93 ± 0.01	8.16 ± 0.01	8.00 ± 0.02	0.033	1142±2	E6	N4564
23	654	12:23:35.28	+16:43:22.3	12.03	9.34 ± 0.01	8.66 ± 0.02	8.43 ± 0.02	0.026	950±9	RSB0$_2$(5)	N4340
24	944	12:26:50.53	+09:35:02.0	12.08	9.11 ± 0.01	8.48 ± 0.01	8.24 ± 0.02	0.025	843±15	S0$_1$(7)	N4417
25	1938	12:42:47.40	+11:26:33.0	12.11	9.17 ± 0.01	8.50 ± 0.01	8.25 ± 0.02	0.026	1164±10	S0$_1$(7)	N4638
26	1279	12:30:17.39	+12:19:43.9	12.15	9.31 ± 0.01	8.62 ± 0.01	8.40 ± 0.01	0.024	1349±3	E2	N4478
27	1720	12:37:30.61	+09:33:18.8	12.29	9.46 ± 0.02	8.74 ± 0.02	8.52 ± 0.04	0.021	2273±12	S0$_{1/2}$(4)	N4578
28	355	12:19:30.61	+14:52:41.4	12.41	9.34 ± 0.01	8.65 ± 0.01	8.42 ± 0.02	0.036	1359±4	SB0$_{2/3}$	N4262
29	1619	12:35:30.61	+12:13:15.4	12.50	9.61 ± 0.01	8.93 ± 0.01	8.75 ± 0.01	0.040	381±9	E7/S0$_1$(7)	N4550
30	1883	12:41:32.70	+07:18:53.0	12.57	9.54 ± 0.02	8.92 ± 0.02	8.67 ± 0.03	0.025	1875±22	RSB0$_{1/2}$	N4612
31	1242	12:29:53.49	+14:04:07.0	12.60	9.70 ± 0.01	9.04 ± 0.01	8.79 ± 0.02	0.042	1609±11	S0$_1$(8)	N4474
32	784	12:25:14.75	+15:36:27.2	12.67	9.74 ± 0.01	9.06 ± 0.02	8.87 ± 0.02	0.024	1069±10	S0$_1$(2)	N4379
33	1537	12:34:06.10	+11:19:17.0	12.70	9.94 ± 0.01	9.22 ± 0.02	9.04 ± 0.02	0.046	1374±10	SB0$_2$(5)	N4528
34	778	12:25:12.27	+14:45:43.8	12.72	9.80 ± 0.01	9.12 ± 0.01	8.89 ± 0.02	0.038	1375±11	S0$_1$(3)	N4377
35	1321	12:30:52.21	+16:45:32.6	12.84	10.42 ± 0.02	9.77 ± 0.03	9.54 ± 0.03	0.028	967±6	S0$_1$(1)	N4489
36	828	12:25:41.70	+12:48:38.0	12.84	10.13 ± 0.01	9.44 ± 0.02	9.23 ± 0.02	0.033	561±15	E5	N4387
37	1250	12:29:59.10	+12:20:55.0	12.91	10.49 ± 0.01	9.83 ± 0.02	9.57 ± 0.02	0.028	1970±11	S0$_3$(5)	N4476
38	1630	12:35:37.97	+12:15:50.5	12.91	9.87 ± 0.01	9.20 ± 0.02	8.95 ± 0.02	0.039	1172±6	E2	N4551
39	1146	12:28:57.56	+13:14:30.8	12.93	10.34 ± 0.02	9.68 ± 0.02	9.45 ± 0.02	0.023	635±6	E1	N4458
40	1025	12:27:36.71	+08:09:14.8	13.06	10.17 ± 0.02	9.52 ± 0.02	9.30 ± 0.03	0.022	1071±6	E0/S0$_1$(0)	N4434
41	1303	12:30:40.64	+09:00:55.9	13.10	10.27 ± 0.02	9.61 ± 0.03	9.40 ± 0.04	0.020	875±10	SB0$_1$(5)	N4483
42	1913	12:42:10.70	+07:40:37.0	13.22	10.43 ± 0.02	9.78 ± 0.02	9.57 ± 0.04	0.022	1892±37	E7	N4623
43	1327	12:30:57.56	+12:16:17.2	13.26	9.86 ± 0.01	9.28 ± 0.01	9.07 ± 0.01	0.023	150±45	E2	N4486A
44	1125	12:28:43.37	+11:45:21.0	13.30	10.19 ± 0.02	9.37 ± 0.02	9.19 ± 0.03	0.030	195±47	S0$_1$(9)	N4452
45	1475	12:33:04.95	+16:15:55.9	13.36	10.83 ± 0.01	10.20 ± 0.02	10.01 ± 0.03	0.031	951±11	E2	N4515
46	1178	12:29:21.30	+08:09:23.0	13.37	10.51 ± 0.02	9.85 ± 0.02	9.64 ± 0.03	0.022	1243±2	E3	N4464
47	1283	12:30:18.40	+13:34:40.9	13.45	10.79 ± 0.02	10.15 ± 0.03	9.91 ± 0.04	0.029	876±10	SB0$_2$(2)	N4479
48	1261	12:30:10.39	+10:46:46.1	13.56	11.69 ± 0.04	11.11 ± 0.06	10.89 ± 0.09	0.029	1871±16	d:E5,N	N4482
49	698	12:24:05.00	+11:13:06.0	13.60	10.85 ± 0.03	10.22 ± 0.03	10.02 ± 0.05	0.026	2080±10	S0$_1$(8)	N4352
50	1422	12:32:14.21	+10:15:05.0	13.64	11.83 ± 0.04	11.23 ± 0.06	11.05 ± 0.10	0.031	1288±10	E1,N:	I3468
51	2048	12:47:15.32	+10:12:13.0	13.81	11.95 ± 0.03	11.31 ± 0.04	11.14 ± 0.08	0.032	1084±12	d:S0(9)	I3773
52	1871	12:41:15.72	+11:23:13.5	13.86	11.58 ± 0.03	10.92 ± 0.03	10.68 ± 0.06	0.030	567±10	E3	I3653
53	9	12:09:22.34	+13:59:33.1	13.93	...	...	...	0.039	1804±49	dE1,N	I3019
54	575	12:22:43.31	+08:11:53.7	14.14	11.33 ± 0.02	10.63 ± 0.03	10.42 ± 0.04	0.025	1231±9	E4	N4318

TABLE 1. GLOBAL MORPHOLOGICAL PROPERTIES OF PROGRAM GALAXIES.—*Continued*

ID	VCC	RA (J2000) (NED)	Dec (J2000) (NED)	B_T (mag)	J (mag)	H (mag)	K_s (mag)	$E(B-V)$ (mag)	v_{sys} (km s^{-1})	Type (NED)	Other Names
55	1910	12:42:08.69	+11:45:14.9	14.17	11.81 ± 0.05	11.07 ± 0.06	10.78 ± 0.09	0.031	206±26	dE1,N	I809
56	1049	12:27:54.86	+08:05:25.2	14.20	12.87 ± 0.07	12.24 ± 0.09	11.97 ± 0.13	0.022	716±36	S0(4)	U7580
57	856	12:25:57.81	+10:03:12.8	14.25	12.47 ± 0.06	11.77 ± 0.07	11.66 ± 0.13	0.024	1025±10	dE1,N	I3328
58	140	12:15:12.58	+14:25:59.1	14.30	11.97 ± 0.03	11.32 ± 0.04	11.20 ± 0.06	0.037	1072±46	$S0_{1/2}(4)$	I3065
59	1355	12:31:20.04	+14:06:53.5	14.31	...	...	...	0.034	1332±63	dE2,N	I3442
60	1087	12:28:14.90	+11:47:24.0	14.31	12.25 ± 0.05	11.61 ± 0.07	11.49 ± 0.12	0.027	675±12	dE3,N	I3381
61	1297	12:30:31.85	+12:29:26.0	14.33	11.08 ± 0.01	10.34 ± 0.02	10.13 ± 0.02	0.021	1555±4	E1	N4486B
62	1861	12:40:58.54	+11:11:04.4	14.37	12.34 ± 0.05	11.71 ± 0.06	11.55 ± 0.11	0.029	470±39	dE0,N	I3652
63	543	12:22:19.55	+14:45:38.6	14.39	12.71 ± 0.04	12.08 ± 0.06	11.93 ± 0.09	0.031	985±12	dE5	U7436
64	1431	12:32:23.37	+11:15:46.2	14.51	12.18 ± 0.04	11.53 ± 0.05	11.30 ± 0.08	0.051	1500±38	dE0,N	I3470
65	1528	12:33:51.62	+13:19:21.3	14.51	12.37 ± 0.03	11.73 ± 0.04	11.52 ± 0.06	0.028	1608±35	d:E1	I3501
66	1695	12:36:54.87	+12:31:12.5	14.53	13.31 ± 0.05	12.64 ± 0.07	12.51 ± 0.09	0.045	1547±29	dS0:	I3586
67	1833	12:40:19.65	+15:56:07.2	14.54	12.33 ± 0.03	11.69 ± 0.04	11.47 ± 0.05	0.036	1679±34	$S0_1(6)$	
68	437	12:20:48.82	+17:29:13.4	14.54	12.73 ± 0.04	12.12 ± 0.06	11.88 ± 0.09	0.029	1474±46	dE5,N	U7399A
69	2019	12:45:20.42	+13:41:33.0	14.55	12.84 ± 0.05	12.13 ± 0.07	11.94 ± 0.09	0.022	1895±44	dE4,N	I3735
70	33	12:11:07.76	+14:16:29.8	14.67	13.36 ± 0.05	12.71 ± 0.07	12.54 ± 0.09	0.037	1093±52	d:E2,N:	I3032
71	200	12:16:33.68	+13:01:53.1	14.69	13.55 ± 0.05	12.91 ± 0.06	12.72 ± 0.09	0.030	65±43	dE2,N	
72	571	12:22:41.14	+07:57:01.1	14.74	13.71 ± 0.07	13.05 ± 0.08	12.82 ± 0.14	0.022	1047±37	$SB0_1(6)$	
73	21	12:10:23.19	+10:11:17.6	14.75	13.58 ± 0.08	12.95 ± 0.10	12.85 ± 0.17	0.021	506±35	dS0(4)	I3025
74	1488	12:33:13.44	+09:23:49.8	14.76	13.53 ± 0.08	12.81 ± 0.09	12.70 ± 0.15	0.021	1157±48	E6:	I3487
75	1779	12:39:04.67	+14:43:51.5	14.83	14.39 ± 0.05	13.81 ± 0.07	13.80 ± 0.10	0.028	1313±45	dS0(6):	I3612
76	1895	12:41:52.00	+09:24:10.3	14.91	13.43 ± 0.06	12.70 ± 0.07	12.62 ± 0.13	0.017	1032±51	d:E6	U7854
77	1499	12:33:19.79	+12:51:12.8	14.94	13.74 ± 0.04	13.30 ± 0.07	13.10 ± 0.09	0.030	-575±35	E3 pec or S0	I3492
78	1545	12:34:11.54	+12:02:55.9	14.96	13.02 ± 0.04	12.43 ± 0.06	12.17 ± 0.07	0.042	2050±32	E4	I3509
79	1192	12:29:30.20	+07:59:34.0	15.04	11.97 ± 0.04	11.36 ± 0.07	11.02 ± 0.09	0.023	1426±22	E3	N4467
80	1857	12:40:53.10	+10:28:34.0	15.07	...	...	...	0.025	634±69	dE4:,N?	I3647
81	1075	12:28:12.29	+10:17:51.0	15.08	13.76 ± 0.09	13.25 ± 0.11	12.95 ± 0.16	0.027	1844±40	dE4,N	I3383
82	1948	12:42:58.02	+10:40:54.5	15.10	...	...	...	0.025	1672±98	dE3	
83	1627	12:35:37.25	+12:22:54.9	15.16	12.61 ± 0.02	11.90 ± 0.03	11.73 ± 0.04	0.039	236±41	E0	
84	1440	12:32:33.39	+15:24:55.2	15.20	12.81 ± 0.03	12.12 ± 0.04	11.98 ± 0.06	0.028	414±44	E0	I798
85	230	12:17:19.64	+11:56:36.2	15.20	14.04 ± 0.09	13.36 ± 0.10	13.34 ± 0.18	0.028	1490±65	dE4:,N:	I3101
86	2050	12:47:20.69	+12:09:58.7	15.20	14.32 ± 0.08	13.70 ± 0.12	13.30 ± 0.12	0.023	1193±48	dE5:,N	I3779
87	1993	12:44:12.02	+12:56:30.1	15.30	14.04 ± 0.05	13.40 ± 0.07	13.23 ± 0.09	0.025	875±50	E0	
88	751	12:24:48.34	+18:11:42.0	15.30	12.82 ± 0.03	12.18 ± 0.05	11.96 ± 0.06	0.032	710±39	dS0	I3292
89	1828	12:40:13.38	+12:52:29.0	15.33	13.87 ± 0.06	13.30 ± 0.08	13.12 ± 0.10	0.037	1517±57	dE2,N	I3635
90	538	12:22:14.83	+07:10:00.8	15.40	14.20 ± 0.08	13.57 ± 0.08	13.39 ± 0.13	0.020	500±50	E0	N4309A
91	1407	12:32:02.69	+11:53:24.8	15.49	13.45 ± 0.07	12.82 ± 0.09	12.87 ± 0.15	0.032	1001±11	dE2,N	I3461
92	1886	12:41:39.41	+12:14:52.4	15.49	...	...	...	0.033	1159±65	dE5,N	
93	1199	12:29:34.97	+08:03:31.4	15.50	13.26 ± 0.05	12.59 ± 0.06	12.43 ± 0.09	0.022	900±50	E2	
94	1743	12:38:06.77	+10:04:56.6	15.50	14.39 ± 0.11	14.11 ± 0.17	13.40 ± 0.17	0.019	1279±10	dE6	I3602
95	1539	12:34:06.77	+12:44:30.1	15.68	...	...	...	0.032	1390±50	dE0,N	
96	1185	12:29:23.43	+12:27:02.4	15.68	14.58 ± 0.08	13.89 ± 0.10	13.62 ± 0.11	0.023	500±50	dE1,N	
97	1826	12:40:11.24	+09:53:45.9	15.70	14.25 ± 0.07	13.58 ± 0.08	13.64 ± 0.13	0.017	2033±38	dE2,N	I3633
98	1512	12:33:34.56	+11:15:42.8	15.73	...	...	...	0.050	762±35	dS0 pec	
99	1489	12:33:13.84	+10:55:43.6	15.89	...	...	...	0.034	80±50	dE5,N?	I3490
100	1661	12:36:24.81	+10:23:04.6	15.97	...	...	...	0.020	1400±50	dE0,N	

NOTE. — RA, Dec and v_{sys} are from the NASA/IPAC Extragalactic Database; B_T and Hubble Type are from the VCC. Infrared magnitudes are from the 2MASS database. Magnitudes are not extinction corrected; $E(B-V)$ values are calculated from the reddening maps of Schlegel, Finkbeiner, & Davis (1998)

Table 2. Morphological Peculiarities.

ID	VCC	Dust	Small-scale Disk	Large-scale Disk	Nucleus	Bar	Comments
1	1226	C1			II		Dust lane
2	1316	C1			0		Dust filaments. Non thermal nucleus; saturated in $g-$band
3	1978				II		
4	881	C1			II		Dust filaments. The surface brightness profile dips towards the center
5	798	C1:		Y:	II		Possible dust patches. Visibly boxy within $r < 1''$
6	763	C2			0		Dust lanes; non-thermal nucleus
7	731				Ib		
8	1535	C3			0		Dust disk; visibly boxy in the inner region, disky at large radii
9	1903		Y		Id		Center saturated in $g-$band; small inner stellar disk
10	1632	C1			II		Dust filaments/patches
11	1231			Y:	II		Small nuclear bar?
12	2095			Y	Ib		ITD?
13	1154	C3			Id		Dust Disk
14	1062				Id		Evidence for distinct morphological components
15	2092				Ib	Y	
16	369				Ib	Y:	
17	759	C4			II		Small nuclear dust disk; stellar rings, arcs
18	1692		Y	Y	Ic		Edge-on stellar ring.
19	1030	C3		Y	0		Dust disk. Boxy isophotes in the inner region, disky at large radii
20	2000			Y	Id		Center saturated in $g-$band; visibly boxy bulge superimposed to a disk component. Possible remnant of stripped satellite present in the field.
21	685	C4	Y	Y	0		Dust disk; disk population of GCs
22	1664			Y	Ic		Disky isophotes
23	654				Ib	Y	Stellar ring; possible remnant of stripped satellite present in the field
24	944			Y	Ic		
25	1938			Y	Ib		ITD; possible spiral structure?
26	1279		Y		Id		
27	1720				Ia		
28	355	C1			Id	Y	Dust filaments
29	1619	C1			Ia		Dust filaments
30	1883				Ia	Y	
31	1242			Y	Ia		Large GC population
32	784				Ia		Visible isophotal twists
33	1537				Id	Y	ITD? Small GC system
34	778				Id	Y	
35	1321				Id		Visible isophotal twists
36	828				Ia		Visibly boxy
37	1250	C3			Ia		Dust disk
38	1630		Y		Ia		
39	1146		Y		Ia		
40	1025				Ic		
41	1303				Ib		Spiral arms
42	1913		Y	Y	Ia		Distinct morphological components
43	1327	C4	Y		II		Dust disk. Tidally truncated by interaction with M87
44	1125		Y	Y	Ia		ITD?
45	1475		Y		Ib		
46	1178				Ib		
47	1283				Ia	Y:	
48	1261				Ia		
49	698		Y	Y	Ia		
50	1422	C1:			Ia		Possible large-scale dust filaments
51	2048			Y	Ia		
52	1871				Ia		
53	9				Ie		Low surface brightness
54	575		Y	Y	Id		ITD or stellar ring
55	1910				Ia		
56	1049				II		
57	856				Ia		Dwarf spiral
58	140				Ia		
59	1355				Ia		
60	1087				Ia		
61	1297				Id		Tidally truncated by interaction with M87
62	1861				Ia		
63	543				Ia		
64	1431				Ia		
65	1528				Ia		
66	1695				Ia		Spiral pattern?
67	1833				II		
68	437				Ia		
69	2019				Ia		

TABLE 2. MORPHOLOGICAL PECULIARITIES.— *Continued*

ID	VCC	Dust	Small-scale Disk	Large-scale Disk	Nucleus	Bar	Comments
70	33				Ia		
71	200				Ia		
72	571	C2			0		Dust lane
73	21				Ie		dIrr/dE transition
74	1488			Y	Ia		
75	1779	C1			Ie		dIrr/dE transition, Dust filaments; small GC system
76	1895				Ia		
77	1499				II		dIrr/dE transition
78	1545				Ia		Substantial population of bright clusters
79	1192				Ia		Tidally truncated by interaction with M49
80	1857				Ie		Low surface brightness
81	1075				Ia		
82	1948				Ie		
83	1627				Ia		Small GC system
84	1440				Ia		Large GC system
85	230				Ia		
86	2050				Ia		
87	1993				Ib		
88	751			Y	Ia		
89	1828				Ia		
90	538				Ia		
91	1407				Ia		Large GC system
92	1886				Ia		
93	1199		Y		Ia		Spiral pattern? Tidally truncated by interaction with M49
94	1743				Ib		
95	1539				Ia		Large GC system
96	1185				Ia		
97	1826				Ia		Small GC system
98	1512				II		dIrr/dE transition
99	1489				Ia		
100	1661				Ia		

NOTE. — For each galaxy (col 2), the columns report the detection of dust (col. 3), a small or large-scale stellar disk (col. 4 and 5 respectively), a nucleus (col 6) and a stellar bar (col. 7). Other peculiarities are noted in column 8. A "Y" indicates the presence of a bar or stellar disk, a ":" reflects uncertainty. A disk is defined as having "small-scale" if it does not dominate the galaxy morphology at large radii, viceversa for a large-scale disk. Both a large and small-scale disk can be detected in the same galaxies when the two disks have different scale lengths or surface brightnesses, and therefore appear as distinct from inspection of the images, or in their effect on the surface brightness profile. The presence of dust is classified according to the dust morphology: C1 for faint wisps and patches, C2 for high extinction irregular dust lanes, C3 for large, patchy dust disks, and C4 for small, regular featureless dust disks (see §4.1.1 for detail). In the case of the column indicating whether a nucleus is present, we adopt the terminology used in Paper VIII: "0" means that the presence of a nucleus could not be investigated either because of the presence of significant dust contamination, or non-thermal emission from an active nucleus; II refers to galaxies which are non-nucleated; Ia certainly nucleated; Ib certainly nucleated, but the nucleus is too faint to derive a reliable fit; Ic likely nucleated; Id possibly nucleated; Ie the nucleus is offset from the isophotal center. An "ITD" in the last column stands for "Inner Truncated Disk".

Table 3. Best Fit parameters to the Luminosity Profile for Program Galaxies.

ID	VCC	Model	μ_{r_e} (mag arcsec^{-2})	γ	n	r_e ($''$)	r_b ($''$)	r_h ($''$)	$m_{nucleus}$ (mag)
1	1226	cS	23.51	0.086	5.503	208.01	1.94	···	···
			21.98	0.093	5.626	211.38	1.86	···	···
2	1316	cS	23.45	0.322	6.094	163.83	7.15	···	···
			21.86	0.309	6.021	164.18	6.60	···	···
3	1978	cS	22.52	0.206	4.766	98.16	2.56	···	···
			20.90	0.203	4.854	98.48	2.52	···	···
4	881	cS	25.29	0.021	7.016	411.84	0.72	···	···
			23.90	0.021	7.316	440.99	0.73	···	···
5	798	cS	23.90	0.224	6.813	170.82	0.62	···	···
			22.35	0.230	6.397	160.68	0.60	···	···
6	763	cS	23.70	0.302	7.337	146.97	1.85	···	···
			22.28	0.307	7.777	155.47	1.88	···	···
7	731	cS	23.61	0.235	5.871	115.39	1.35	···	···
			22.22	0.239	6.287	122.69	1.36	···	···
8	1535	···	···	···	···	···	···	···	···
9	1903	S	23.61	···	6.852	106.75	···	···	···
			22.44	···	7.843	126.44	···	···	···
10	1632	cS	23.27	0.252	7.088	85.12	0.65	···	···
			21.72	0.299	7.604	84.37	0.75	···	···
11	1231	S	20.32	···	2.955	16.89	···	···	···
			19.01	···	3.222	18.64	···	···	···
12	2095	S	20.37	···	3.280	11.87	···	···	···
			19.33	···	3.962	14.29	···	···	···
13	1154	S	21.63	···	4.918	28.15	···	···	···
			20.17	···	5.070	29.50	···	···	···
14	1062	S	20.49	···	3.291	16.92	···	···	···
			18.65	···	3.146	14.21	···	···	···
15	2092	S	21.47	···	4.279	24.13	···	···	···
			20.45	···	5.091	31.45	···	···	···
16	369	S	19.89	···	2.645	7.93	···	···	···
			18.30	···	2.761	7.74	···	···	···
17	759	S	21.71	···	3.245	26.18	···	···	···
			20.29	···	3.538	27.27	···	···	···
18	1692	S	19.68	···	2.458	9.50	···	···	···
			18.19	···	2.735	9.34	···	···	···
19	1030	···	···	···	···	···	···	···	···
20	2000	S	20.19	···	3.977	10.45	···	···	···
			18.60	···	4.458	9.44	···	···	···
21	685	S	20.23	···	3.170	11.91	···	···	···
			18.61	···	3.215	11.20	···	···	···
22	1664	S	21.00	···	3.982	15.76	···	···	···
			19.52	···	4.332	15.91	···	···	···
23	654	S	22.04	···	4.020	21.63	···	···	···
			20.52	···	4.032	20.78	···	···	···
24	944	S	20.60	···	3.320	12.57	···	···	···
			19.02	···	3.356	11.61	···	···	···
25	1938	S	21.00	···	3.945	14.79	···	···	···
			19.42	···	4.116	13.36	···	···	···
26	1279	S	20.27	···	1.937	11.45	···	···	···
			18.94	···	2.159	12.01	···	···	···
27	1720	S	22.75	···	4.466	32.52	···	0.085	18.41
			21.03	···	4.466	27.22	···	0.085	16.85
28	355	S	20.38	···	3.725	9.78	···	···	···
			18.67	···	3.692	8.83	···	···	···
29	1619	S	20.21	···	1.662	10.43	···	0.324	17.15
			18.75	···	1.662	9.98	···	0.324	15.61
30	1883	S	22.20	···	4.575	24.99	···	0.024	18.75
			20.86	···	4.575	25.02	···	0.024	17.63
31	1242	S	21.62	···	3.363	16.88	···	0.035	19.85
			20.14	···	3.363	16.67	···	0.035	18.16
32	784	S	21.20	···	3.006	14.24	···	0.161	18.36
			19.69	···	3.006	13.67	···	0.161	16.71
33	1537	S	20.28	···	2.781	8.01	···	···	···
			18.83	···	2.883	7.92	···	···	···
34	778	S	19.77	···	3.103	5.90	···	···	···
			18.09	···	3.036	5.19	···	···	···
35	1321	S	23.73	···	6.077	37.07	···	···	···
			22.02	···	5.797	30.00	···	···	···
36	828	S	20.95	···	2.203	10.81	···	0.208	18.55
			19.43	···	2.203	10.50	···	0.208	16.99
37	1250	cS	21.21	0.435	7.976	11.07	2.45	0.026	19.75
			20.12	0.407	7.976	11.78	2.33	0.026	18.22
38	1630	S	21.24	···	2.240	13.29	···	0.501	17.40
			19.71	···	2.240	13.11	···	0.501	15.74

TABLE 3. BEST FIT PARAMETERS TO THE LUMINOSITY PROFILE FOR PROGRAM GALAXIES.— *Continued*

ID	VCC	Model	μ_{r_e} (mag arcsec^{-2})	γ	n	r_e ($''$)	r_b ($''$)	r_h ($''$)	$m_{nucleus}$ (mag)
39	1146	S	22.09	···	2.043	18.60	···	0.780	15.38
			20.54	···	2.043	16.04	···	0.780	13.98
40	1025	S	21.18	···	3.661	11.13	···	···	···
			19.60	···	3.711	10.12	···	···	···
41	1303	S	21.94	···	3.791	15.18	···	···	···
			20.25	···	3.727	12.89	···	···	···
42	1913	S	21.83	···	2.275	14.67	···	0.597	17.57
			20.37	···	2.275	14.39	···	0.597	15.98
43	1327	S	20.27	···	2.719	6.61	···	···	···
			18.46	···	2.614	5.64	···	···	···
44	1125	S	21.51	···	2.087	13.26	···	0.060	20.49
			19.99	···	2.087	11.16	···	0.060	19.54
45	1475	S	21.21	···	3.133	9.49	···	···	···
			19.92	···	3.382	9.49	···	···	···
46	1178	S	20.50	···	3.729	6.58	···	···	···
			18.81	···	3.468	5.83	···	···	···
47	1283	S	22.57	···	2.410	19.28	···	0.053	20.67
			21.11	···	2.410	19.46	···	0.053	19.10
48	1261	S	22.97	···	2.171	20.95	···	0.041	19.51
			21.70	···	2.135	20.13	···	0.036	18.31
49	698	S	22.37	···	3.449	16.01	···	0.041	19.94
			20.90	···	3.365	15.20	···	0.041	18.64
50	1422	S	23.04	···	1.914	19.29	···	0.038	20.23
			22.01	···	2.101	21.98	···	0.035	19.02
51	2048	S	22.19	···	1.882	11.90	···	0.037	21.46
			21.10	···	1.973	12.64	···	0.031	20.33
52	1871	S	21.29	···	1.835	6.82	···	0.125	18.74
			19.90	···	1.983	6.92	···	0.108	17.51
53	9	S	23.87	···	1.022	29.62	···	···	···
			22.98	···	1.146	36.14	···	···	···
54	575	S	28.81	···	12.828	490.00	···	···	···
			27.60	···	13.325	490.00	···	···	···
55	1910	S	22.52	···	1.596	12.52	···	0.039	19.83
			21.06	···	1.564	12.01	···	0.038	18.66
56	1049	S	22.82	···	2.539	9.94	···	···	···
			21.37	···	2.017	8.38	···	···	···
57	856	S	22.85	···	1.165	14.72	···	0.163	18.98
			21.85	···	1.317	16.70	···	0.153	17.88
58	140	S	21.76	···	1.394	9.24	···	0.030	22.11
			20.56	···	1.422	9.27	···	0.022	21.22
59	1355	S	24.25	···	1.430	24.55	···	0.043	21.11
			23.38	···	1.647	30.52	···	0.038	20.10
60	1087	S	23.15	···	1.558	18.87	···	0.027	20.24
			22.00	···	1.675	20.37	···	0.027	18.92
61	1297	S	18.90	···	2.732	2.33	···	···	···
			17.35	···	2.788	2.29	···	···	···
62	1861	S	22.96	···	1.361	15.14	···	0.137	20.12
			21.96	···	1.593	18.24	···	0.119	19.09
63	543	S	23.21	···	1.605	17.14	···	0.031	23.88
			22.10	···	1.716	18.29	···	0.010	23.00
64	1431	S	22.16	···	1.538	9.86	···	0.238	19.68
			20.74	···	1.538	9.90	···	0.233	18.57
65	1528	S	22.36	···	2.041	9.90	···	0.010	22.41
			21.09	···	2.101	9.88	···	0.010	21.75
66	1695	S	23.86	···	2.302	20.21	···	0.010	22.70
			23.15	···	2.554	27.05	···	0.010	21.44
67	1833	S	21.79	···	1.856	7.38	···	···	···
			20.65	···	1.864	7.73	···	···	···
68	437	S	23.82	···	1.905	25.02	···	0.089	20.02
			22.63	···	1.984	25.99	···	0.083	19.04
69	2019	S	23.22	···	1.469	15.25	···	0.037	20.33
			22.38	···	1.723	19.06	···	0.029	19.23
70	33	S	22.54	···	1.053	9.10	···	0.033	22.19
			21.46	···	1.064	9.16	···	0.032	21.30
71	200	S	23.31	···	1.836	12.80	···	0.053	22.88
			22.15	···	1.933	13.12	···	0.038	21.97
72	571	S	23.57	···	2.750	13.26	···	···	···
			22.58	···	2.775	14.13	···	···	···
73	21	S	22.52	···	1.206	9.76	···	···	···
			22.01	···	1.316	12.28	···	···	···
74	1488	S	22.48	···	1.406	9.31	···	0.010	23.79
			21.74	···	1.394	10.50	···	0.046	22.95
75	1779	S	22.77	···	1.429	10.77	···	···	···
			21.84	···	1.314	11.29	···	···	···

TABLE 3. BEST FIT PARAMETERS TO THE LUMINOSITY PROFILE FOR PROGRAM GALAXIES.— *Continued*

ID	VCC	Model	μ_{r_e} (mag arcsec^{-2})	γ	n	r_e ($''$)	r_b ($''$)	r_h ($''$)	$m_{nucleus}$ (mag)
76	1895	S	22.73	···	1.372	10.07	···	0.023	23.62
			21.68	···	1.402	10.43	···	0.010	22.85
77	1499	S	21.44	···	1.236	5.50	···	···	···
			21.00	···	1.166	6.48	···	···	···
78	1545	S	23.18	···	2.545	11.24	···	0.050	21.94
			21.79	···	2.718	10.74	···	0.037	20.91
79	1192	S	22.01	···	2.908	7.27	···	0.120	19.10
			20.46	···	2.902	7.09	···	0.121	17.93
80	1857	S	23.99	···	0.768	20.82	···	···	···
			23.13	···	0.856	21.88	···	···	···
81	1075	S	23.57	···	1.242	14.57	···	0.040	21.09
			22.65	···	1.422	17.80	···	0.039	20.14
82	1948	S	23.47	···	1.152	10.94	···	···	···
			22.56	···	1.199	12.22	···	···	···
83	1627	S	20.99	···	2.006	3.73	···	0.197	18.84
			19.66	···	2.189	3.87	···	0.197	17.42
84	1440	S	22.37	···	3.124	7.75	···	0.063	19.72
			21.12	···	3.307	7.70	···	0.056	18.41
85	230	S	23.22	···	1.376	9.71	···	0.037	20.32
			21.97	···	1.353	9.10	···	0.034	19.25
86	2050	S	23.11	···	1.316	10.80	···	0.073	22.39
			22.09	···	1.421	11.74	···	0.066	21.44
87	1993	S	23.16	···	1.714	8.58	···	···	···
			22.34	···	1.998	10.96	···	···	···
88	751	S	22.67	···	2.025	9.95	···	0.046	21.23
			21.82	···	2.434	12.98	···	0.035	20.20
89	1828	S	23.77	···	1.464	14.55	···	0.060	21.52
			22.74	···	1.654	16.49	···	0.057	20.53
90	538	S	22.31	···	1.833	4.82	···	0.033	21.29
			21.17	···	1.867	4.86	···	0.030	20.18
91	1407	S	22.92	···	1.394	10.17	···	0.145	20.40
			21.82	···	1.521	10.89	···	0.127	19.43
92	1886	S	23.38	···	0.794	12.61	···	0.036	22.06
			22.45	···	0.833	13.40	···	0.041	21.07
93	1199	S	21.63	···	2.942	3.41	···	0.075	19.76
			20.03	···	3.016	3.32	···	0.063	18.42
94	1743	S	23.30	···	1.136	10.41	···	···	···
			22.23	···	1.178	10.72	···	···	···
95	1539	S	25.25	···	1.907	26.30	···	0.231	20.94
			23.74	···	1.622	22.38	···	0.265	19.84
96	1185	S	24.49	···	1.601	18.50	···	0.057	20.88
			23.39	···	1.712	21.16	···	0.050	19.94
97	1826	S	22.64	···	1.522	7.06	···	0.024	20.12
			21.45	···	1.508	6.87	···	0.025	18.94
98	1512[(1)]	cS	31.34	0.377	15.578	490.00	0.37	···	···
			26.35	0.281	7.104	76.82	0.38	···	···
99	1489	S	23.66	···	0.993	10.40	···	0.051	22.39
			22.65	···	1.012	11.09	···	0.058	21.54
100	1661	S	26.49	···	2.342	58.07	···	0.079	20.31
			24.63	···	1.931	39.27	···	0.082	19.28

NOTE. — For each galaxy, the first row reports parameters in the $g-$band, the second in the $z-$band. Surface brightnesses are not extinction corrected. Columns 1 and 2 list the ID and VCC numbers of the galaxies; column 3 shows whether the profile is best described by a core-Sérsic (cS) or Sérsic (S) model (§4.2.1). The next five columns list the parameters of the best fit model, as in equations 7 and 8; for the core-Sérsic models, I_e represents the surface brightness measured at one effective radius, and is related to I_b (equation 9), as $I_e = I_b \exp\{b_n[(r_b/r_e)^{1/n} - 1]\}$. The last two columns list the half-light radius and total magnitude of the nuclear King model, when fitted.

(1) Based on the dIrr/dE nature of this object, the irregular profile shape, and the large discrepancy between the values of r_e measured in the two filters, r_e and all integrated quantities for this galaxy are deemed unreliable.

Table 4. Global Structural Parameters for Program Galaxies.

ID	VCC	RA (J2000)	Dec (J2000)	r_e (arcsec)	$\mu(r_e)$ (mag arcsec^{-2})	$\langle\mu(r_e)\rangle$ (mag arcsec^{-2})	$\langle\epsilon\rangle$	$\langle B4\rangle$	$\langle\Theta\rangle$ (degrees)	m (mag)	$g-z$ (mag)
1	1226	12:29:46.74	+8:00:01.463	209.15	99.99	21.96	0.09±0.02	-0.002± 0.002	-19.9± 2.8	8.37	1.60±0.03
				212.51	99.99	20.42	0.09±0.02	-0.003± 0.003	-18.9± 2.1	6.79	
2	1316	12:30:49.42	+12:23:28.35	171.71	99.99	21.96	0.02±0.04	0.001± 0.007	46.1± 37.1	8.79	1.60±0.04
				170.74	99.99	20.35	0.02±0.01	0.001± 0.007	15.8± 36.7	7.19	
3	1978	12:43:40.08	+11:33:09.23	99.34	22.83	21.06	0.11±0.04	-0.004± 0.003	-83.6± 4.4	9.08	1.62±0.02
				100.05	21.21	19.45	0.11±0.05	-0.004± 0.004	-83.4± 3.6	7.45	
4	881	12:26:11.76	+12:56:46.06	411.84	99.99	23.60	0.19±0.02	-0.005± 0.006	-57.2± 4.9	8.53	1.57±0.05
				440.99	99.99	22.19	0.19±0.02	-0.005± 0.006	-57.2± 4.9	6.97	
5	798	12:25:24.06	+18:11:28.88	170.82	99.99	22.23	0.24±0.04	0.007± 0.006	30.2± 1.1	9.07	1.38±0.03
				160.68	99.99	20.70	0.23±0.03	0.008± 0.005	30.0± 0.8	7.68	
6	763	12:25:03.71	+12:53:12.89	149.73	99.99	22.03	0.18±0.02	-0.002± 0.012	-51.8± 7.2	9.16	1.56±0.01
				158.16	99.99	20.58	0.18±0.02	-0.003± 0.012	-52.5± 7.0	7.59	
7	731	12:24:28.35	+7:19:04.060	116.14	99.99	22.04	0.25±0.03	-0.002± 0.008	43.9± 0.5	9.72	1.53±0.05
				124.16	99.99	20.61	0.25±0.04	-0.001± 0.006	43.8± 0.4	8.15	
8	1535	...	...	...	...	...	...	...	...	...	...
9	1903	12:42:02.31	+11:38:48.73	106.75	23.99	21.93	0.34±0.02	0.028± 0.010	-16.8± 0.2	9.79	1.53±0.04
				126.44	99.99	20.69	0.35±0.02	0.028± 0.009	-16.3± 0.6	8.18	
10	1632	12:35:39.83	+12:33:21.24	85.93	23.58	21.61	0.05±0.01	0.001± 0.002	-60.7± 2.6	9.94	1.61±0.04
				85.99	22.08	20.03	0.05±0.01	0.002± 0.001	-59.8± 1.9	8.36	
11	1231	12:29:48.86	+13:25:45.53	16.89	20.55	19.09	0.43±0.04	0.014± 0.007	-86.3± 0.2	10.95	1.53±0.01
				18.64	19.23	17.72	0.43±0.03	0.014± 0.006	-86.3± 0.2	9.38	
12	2095	12:52:56.04	+11:13:51.86	11.87	20.45	19.08	0.34±0.04	0.030± 0.014	30.3± 0.3	11.71	1.44±0.01
				14.29	19.46	17.94	0.35±0.05	0.027± 0.012	30.1± 0.3	10.17	
13	1154	12:29:00.09	+13:58:42.17	28.15	21.60	20.14	0.14±0.03	0.003± 0.014	-73.6± 16.0	10.89	1.54±0.01
				29.50	20.04	18.65	0.15±0.02	0.003± 0.017	-73.9± 16.5	9.31	
14	1062	12:28:03.90	+9:48:13.879	16.92	20.51	19.20	0.27±0.06	-0.002± 0.006	86.8± 0.7	11.06	1.53±0.01
				14.21	18.69	17.38	0.28±0.07	-0.001± 0.007	86.5± 1.0	9.62	
15	2092	12:52:17.50	+11:18:50.19	24.13	99.99	20.04	0.19±0.02	0.005± 0.008	71.2± 69.0	11.13	1.50±0.01
				31.45	20.72	18.92	0.20±0.02	0.006± 0.009	70.0± 68.8	9.44	
16	369	12:19:45.26	+12:47:53.47	7.93	20.09	18.71	0.06±0.03	0.008± 0.008	-5.2± 37.9	12.22	1.57±0.01
				7.74	18.36	17.10	0.06±0.04	0.009± 0.008	-5.5± 37.7	10.66	
17	759	12:24:55.37	+11:42:15.97	26.18	21.65	20.43	0.31±0.04	-0.004± 0.016	-88.0± 0.6	11.34	1.54±0.01
				27.27	20.20	18.96	0.32±0.04	-0.005± 0.016	-88.4± 0.7	9.79	
18	1692	12:36:53.46	+7:14:46.355	9.50	19.76	18.54	0.35±0.09	0.000± 0.007	-21.7± 0.3	11.65	1.53±0.01
				9.34	18.19	17.00	0.36±0.09	-0.002± 0.007	-21.1± 1.0	10.15	
19	1030	...	...	...	...	...	...	...	...	...	...
20	2000	12:44:31.97	+11:11:25.05	10.45	20.15	18.80	0.40±0.04	0.005± 0.009	-84.9± 2.2	11.71	1.51±0.01
				9.44	18.51	17.14	0.40±0.03	0.004± 0.009	-85.3± 2.1	10.27	
21	685	12:23:57.84	+16:41:36.29	11.91	20.47	18.96	0.36±0.08	0.012± 0.016	28.1± 0.3	11.59	1.55±0.01
				11.20	18.83	17.33	0.36±0.07	0.011± 0.016	28.1± 0.3	10.09	
22	1664	12:36:27.02	+11:26:20.12	15.76	20.98	19.61	0.34±0.07	0.000± 0.004	46.8± 0.6	11.63	1.54±0.01
				15.91	19.62	18.09	0.34±0.07	-0.002± 0.005	46.2± 1.1	10.08	
23	654	12:23:35.28	+16:43:20.64	21.63	21.92	20.65	0.14±0.07	0.003± 0.007	67.4± 24.0	11.98	1.45±0.01
				20.78	20.47	19.12	0.14±0.07	0.003± 0.007	68.0± 25.8	10.54	
24	944	12:26:50.64	+9:35:03.122	12.57	20.59	19.30	0.39±0.05	0.004± 0.027	48.7± 0.6	11.81	1.48±0.01
				11.61	18.94	17.71	0.41±0.05	0.005± 0.027	48.4± 0.8	10.39	
25	1938	12:42:47.40	+11:26:32.44	14.79	21.22	19.62	0.49±0.12	0.009± 0.016	-54.7± 0.5	11.77	1.49±0.01
				13.36	19.63	18.01	0.51±0.12	0.010± 0.021	-54.3± 0.6	10.38	
26	1279	12:30:17.45	+12:19:42.49	11.45	20.27	19.25	0.20±0.07	-0.003± 0.013	-32.1± 2.8	11.96	1.46±0.01
				12.01	19.01	17.86	0.20±0.06	-0.006± 0.013	-31.6± 3.3	10.47	
27	1720	12:37:30.58	+9:33:17.531	32.75	22.81	21.32	0.24±0.01	0.002± 0.003	32.2± 0.4	11.75	1.44±0.02
				27.45	21.08	19.60	0.25±0.01	0.003± 0.003	32.3± 0.5	10.41	
28	355	12:19:30.57	+14:52:42.38	9.78	20.69	19.02	0.13±0.06	0.012± 0.025	-9.4± 16.4	12.08	1.52±0.01
				8.83	19.03	17.31	0.13±0.06	0.012± 0.026	-8.8± 15.0	10.59	
29	1619	12:35:30.65	+12:13:14.22	10.55	20.23	19.30	0.58±0.13	0.020± 0.013	-1.2± 0.7	12.18	1.42±0.01

Table 4. Global Structural Parameters for Program Galaxies.—*Continued*

ID	VCC	RA (J2000)	Dec (J2000)	r_e (arcsec)	$\mu(r_e)$ (mag arcsec^{-2})	$\langle\mu(r_e)\rangle$ (mag arcsec^{-2})	$\langle\epsilon\rangle$	$\langle B4\rangle$	$\langle\Theta\rangle$ (degrees)	m (mag)	$g-z$ (mag)
				10.13	18.87	17.84	0.58±0.12	0.020± 0.012	-1.4± 0.5	10.81	
30	1883	12:41:32.75	+7:18:53.211	24.99	21.97	20.74	0.21±0.02	0.000± 0.005	-45.2± 8.6	11.76	1.32±0.01
				25.02	20.64	19.39	0.21±0.02	0.000± 0.005	-45.1± 8.7	10.40	
31	1242	12:29:53.57	+14:04:07.00	16.88	21.82	20.32	0.25±0.09	0.000± 0.009	78.7± 0.6	12.19	1.46±0.01
				16.67	20.41	18.83	0.26±0.09	0.000± 0.009	79.1± 1.1	10.73	
32	784	12:25:14.74	+15:36:25.46	14.36	21.39	19.97	0.17±0.06	0.005± 0.008	-83.5± 3.2	12.19	1.43±0.01
				13.79	99.99	18.47	0.17±0.06	0.006± 0.009	-83.8± 2.8	10.77	
33	1537	12:34:06.13	+11:19:17.51	8.01	20.33	19.08	0.14±0.04	-0.006± 0.022	60.5± 69.2	12.56	1.45±0.01
				7.92	18.81	17.61	0.17±0.06	-0.004± 0.023	89.7± 76.8	11.12	
34	778	12:25:12.33	+14:45:43.70	5.90	19.79	18.52	0.18±0.04	0.003± 0.006	-16.0± 5.3	12.67	1.47±0.01
				5.19	18.18	16.84	0.18±0.04	0.002± 0.006	-15.1± 6.5	11.27	
35	1321	12:30:52.27	+16:45:31.36	37.07	23.62	22.12	0.10±0.04	0.003± 0.004	-73.5± 54.7	12.28	1.33±0.06
				30.00	21.75	20.43	0.10±0.04	0.001± 0.004	-74.3± 55.4	11.05	
36	828	12:25:41.72	+12:48:37.20	10.87	20.99	19.88	0.32±0.09	-0.019± 0.011	-37.5± 1.5	12.71	1.48±0.01
				10.56	19.52	18.36	0.32±0.09	-0.021± 0.012	-37.1± 2.3	11.25	
37	1250	12:29:59.11	+12:20:55.40	15.85	22.04	20.40	0.50±0.09	0.016± 0.019	26.5± 2.0	12.40	1.21±0.01
				16.55	21.06	19.26	0.49±0.09	0.016± 0.019	26.5± 1.6	11.17	
38	1630	12:35:38.05	+12:15:50.17	13.53	21.40	20.19	0.28±0.03	-0.005± 0.013	69.3± 0.4	12.54	1.50±0.01
				13.35	19.70	18.66	0.28±0.03	-0.005± 0.014	69.0± 0.7	11.03	
39	1146	12:28:57.58	+13:14:31.13	20.71	22.42	21.28	0.16±0.08	0.006± 0.006	6.2± 0.6	12.70	1.36±0.07
				18.29	99.99	19.77	0.17±0.09	0.007± 0.004	6.7± 0.8	11.46	
40	1025	12:27:36.71	+8:09:14.989	11.13	21.26	19.83	0.07±0.03	0.001± 0.003	35.1± 8.2	12.61	1.43±0.01
				10.12	19.67	18.24	0.07±0.03	-0.001± 0.003	38.6± 9.4	11.22	
41	1303	12:30:40.65	+9:00:55.580	15.18	21.83	20.58	0.25±0.04	-0.004± 0.009	61.5± 3.7	12.68	1.42±0.02
				12.89	20.02	18.89	0.26±0.04	-0.005± 0.009	60.6± 4.5	11.35	
42	1913	12:42:10.69	+7:40:35.584	14.97	21.91	20.77	0.50±0.12	-0.007± 0.016	-4.0± 0.9	12.90	1.43±0.01
				14.74	20.48	19.32	0.50±0.12	-0.008± 0.014	-3.8± 1.0	11.48	
43	1327	12:30:57.85	+12:16:14.95	6.61	20.39	19.08	0.30±0.10	0.006± 0.025	6.8± 4.2	12.99	1.63±0.01
				5.64	18.46	17.28	0.32±0.10	0.006± 0.021	6.1± 2.0	11.53	
44	1125	12:28:43.32	+11:45:18.07	13.26	21.77	20.45	0.68±0.03	0.037± 0.026	31.3± 0.4	12.85	1.42±0.01
				11.16	99.99	18.93	0.69±0.03	0.038± 0.022	31.3± 0.4	11.69	
45	1475	12:33:05.12	+16:15:56.13	9.49	99.99	19.94	0.30±0.16	0.011± 0.008	-5.8± 0.6	13.06	1.35±0.01
				9.49	99.99	18.61	0.30±0.15	0.010± 0.008	-5.3± 0.6	11.73	
46	1178	12:29:21.26	+8:09:24.564	6.58	20.48	19.15	0.31±0.03	0.009± 0.003	4.3± 0.3	13.06	1.47±0.01
				5.83	18.85	17.49	0.32±0.03	0.010± 0.003	4.5± 0.5	11.67	
47	1283	12:30:18.39	+13:34:40.06	19.28	22.50	21.44	0.30±0.13	-0.001± 0.008	19.4± 2.0	13.02	1.47±0.03
				19.46	21.20	19.98	0.32±0.13	0.000± 0.009	19.3± 1.6	11.53	
48	1261	12:30:10.35	+10:46:45.83	21.07	22.90	21.90	0.29±0.11	0.001± 0.006	-47.1± 2.8	13.29	1.20±0.05
				20.24	21.74	20.64	0.29±0.12	0.001± 0.007	-46.3± 3.5	12.12	
49	698	12:24:05.01	+11:13:04.29	16.01	22.42	21.06	0.38±0.12	-0.008± 0.005	-83.2± 0.9	13.04	1.38±0.02
				15.20	21.03	19.59	0.38±0.12	-0.009± 0.006	-83.6± 0.7	11.69	
50	1422	12:32:14.21	+10:15:04.81	19.35	23.17	22.03	0.27±0.04	0.011± 0.008	-20.4± 4.5	13.60	1.27±0.08
				22.10	22.20	20.96	0.28±0.05	0.010± 0.012	-20.4± 4.1	12.24	
51	2048	12:47:15.26	+10:12:12.42	11.90	22.34	21.19	0.54±0.02	0.027± 0.014	18.7± 0.7	13.82	1.22±0.01
				12.64	21.31	20.06	0.55±0.02	0.030± 0.015	18.8± 0.8	12.56	
52	1871	12:41:15.76	+11:23:13.92	6.94	21.40	20.33	0.14±0.02	-0.001± 0.005	27.9± 1.7	14.13	1.45±0.01
				7.04	19.96	18.91	0.14±0.02	0.000± 0.006	28.0± 1.7	12.68	
53	9	12:09:22.19	+13:59:33.33	29.62	23.96	23.17	0.18±0.18	-0.020± 0.057	-66.0± 9.2	13.81	1.15±0.15
				36.14	23.14	22.21	0.15±0.22	-0.008± 0.059	-70.1± 49.4	12.43	
54	575	12:22:43.29	+8:11:53.328	490.00	99.99	26.89	0.34±0.05	0.001± 0.008	63.2± 2.8	11.44	1.35±0.04
				490.00	99.99	25.55	0.34±0.05	-0.001± 0.010	62.4± 2.3	10.10	
55	1910	12:42:08.70	+11:45:15.69	12.63	22.55	21.62	0.19±0.06	-0.002± 0.010	-48.7± 9.9	14.12	1.41±0.04
				12.07	21.19	20.15	0.19±0.06	-0.003± 0.013	-48.8± 36.9	12.75	
56	1049	12:27:54.84	+8:05:25.200	9.94	22.65	21.66	0.17±0.02	0.002± 0.004	37.3± 1.8	14.68	1.10±0.04

TABLE 4. GLOBAL STRUCTURAL PARAMETERS FOR PROGRAM GALAXIES.—*Continued*

ID	VCC	RA (J2000)	Dec (J2000)	r_e (arcsec)	$\mu(r_e)$ (mag arcsec^{-2})	$\langle\mu(r_e)\rangle$ (mag arcsec^{-2})	$\langle\epsilon\rangle$	$\langle B4\rangle$	$\langle\Theta\rangle$ (degrees)	m (mag)	$g-z$ (mag)
				8.38	21.35	20.33	0.17±0.02	0.001± 0.009	36.8± 2.3	13.71	
57	856	12:25:57.96	+10:03:13.98	14.96	23.01	22.12	0.09±0.04	0.004± 0.015	87.5± 29.7	14.25	1.22±0.09
				16.94	22.02	21.05	0.10±0.03	-0.002± 0.028	80.3± 27.9	12.91	
58	140	12:15:12.60	+14:25:59.39	9.27	99.99	20.91	0.29±0.02	0.001± 0.007	0.8± 2.6	14.08	1.22±0.02
				9.27	99.99	19.69	0.29±0.04	0.002± 0.016	0.7± 3.2	12.86	
59	1355	12:31:20.19	+14:06:55.28	24.67	99.99	23.40	0.20±0.08	-0.008± 0.044	28.8± 48.4	14.44	1.19±0.01
				30.63	99.99	22.45	0.19±0.09	-0.006± 0.043	42.2± 56.6	13.02	
60	1087	12:28:14.84	+11:47:23.83	18.98	23.28	22.26	0.23±0.07	-0.004± 0.020	-76.8± 8.0	13.87	1.29±0.07
				20.49	22.18	21.06	0.10±0.06	0.010± 0.041	-79.0± 47.4	12.51	
61	1297	12:30:31.95	+12:29:24.36	2.33	18.90	17.71	0.14±0.05	0.007± 0.003	88.5± 4.6	13.88	1.53±0.01
				2.29	17.39	16.14	0.13±0.05	0.007± 0.003	89.9± 3.6	12.34	
62	1861	12:40:58.57	+11:11:03.61	15.26	99.99	22.14	···	···	···	14.22	1.33±0.13
				18.36	22.09	21.05	···	···	···	12.74	
63	543	12:22:19.58	+14:45:39.80	17.14	23.43	22.29	0.45±0.06	-0.005± 0.015	-53.9± 4.9	14.12	1.24±0.02
				18.29	22.26	21.14	0.45±0.08	-0.010± 0.024	-53.4± 6.9	12.83	
64	1431	12:32:23.39	+11:15:46.55	9.95	22.12	21.28	0.04±0.03	-0.002± 0.006	-19.5± 8.6	14.29	1.42±0.04
				9.96	20.75	19.85	0.04±0.03	-0.002± 0.011	-21.5± 9.3	12.86	
65	1528	12:33:51.62	+13:19:22.14	9.90	22.45	21.32	0.17±0.08	0.002± 0.006	-83.1± 1.3	14.34	1.29±0.04
				9.88	21.21	20.03	0.17±0.07	0.003± 0.007	-83.5± 1.5	13.06	
66	1695	12:36:54.85	+12:31:10.67	20.21	23.94	22.76	0.32±0.06	-0.008± 0.008	36.8± 5.2	14.23	1.15±0.10
				27.05	23.22	21.99	0.30±0.05	-0.004± 0.009	37.3± 6.4	12.83	
67	1833	12:40:19.67	+15:56:06.72	7.38	21.74	20.79	0.30±0.01	0.003± 0.006	-5.2± 0.7	14.46	1.21±0.02
				7.73	20.74	19.65	0.30±0.02	0.002± 0.013	-5.5± 0.8	13.21	
68	437	12:20:48.91	+17:29:12.84	25.13	99.99	22.82	0.28±0.07	-0.008± 0.014	76.7± 4.1	13.82	1.26±0.13
				26.11	22.84	21.60	0.28±0.07	-0.007± 0.013	76.3± 4.9	12.52	
69	2019	12:45:20.48	+13:41:32.33	15.36	99.99	22.35	0.28±0.13	0.004± 0.009	-32.1± 14.2	14.42	1.19±0.06
				19.18	22.56	21.42	0.25±0.10	0.004± 0.021	-31.7± 16.4	13.01	
70	33	12:11:07.71	+14:16:28.59	9.16	22.62	21.83	0.11±0.05	0.001± 0.031	32.5± 64.6	15.03	1.10±0.01
				9.19	21.53	20.74	···	···	···	13.93	
71	200	12:16:33.68	+13:01:54.19	12.80	23.34	22.32	0.13±0.06	0.001± 0.011	-7.5± 7.3	14.79	1.21±0.07
				13.12	22.37	21.13	0.14±0.06	0.003± 0.014	-6.3± 7.9	13.55	
72	571	12:22:41.19	+7:57:00.240	13.26	23.50	22.37	0.43±0.02	-0.010± 0.037	-72.5± 0.7	14.77	1.10±0.07
				14.13	22.36	21.37	0.43±0.02	-0.009± 0.022	-71.8± 0.9	13.63	
73	21	12:10:23.13	+10:11:19.22	9.76	22.64	21.74	0.37±0.14	-0.017± 0.061	-81.1± 4.9	14.79	0.82±0.04
				12.28	22.23	21.18	0.36±0.16	-0.011± 0.063	-81.8± 8.3	13.74	
74	1488	12:33:13.43	+9:23:49.796	9.31	22.68	21.62	0.35±0.03	0.012± 0.041	81.3± 2.4	14.78	0.88±0.06
				10.50	21.91	20.88	0.35±0.04	0.009± 0.075	80.4± 3.6	13.78	
75	1779	12:39:04.80	+14:43:52.22	10.77	23.00	21.90	0.46±0.09	-0.002± 0.035	38.6± 6.8	14.74	0.92±0.04
				11.29	21.98	21.01	0.45±0.06	0.000± 0.024	39.0± 5.7	13.75	
76	1895	12:41:52.02	+9:24:09.966	10.07	22.79	21.89	0.50±0.04	0.003± 0.023	38.9± 1.8	14.88	1.11±0.05
				10.43	21.87	20.81	0.50±0.05	0.005± 0.023	39.2± 4.6	13.73	
77	1499	12:33:19.77	+12:51:12.46	5.50	99.99	20.64	0.45±0.08	-0.007± 0.035	57.2± 2.9	14.94	0.51±0.02
				6.48	21.15	20.23	0.41±0.08	-0.003± 0.029	57.5± 2.7	14.18	
78	1545	12:34:11.55	+12:02:55.60	11.24	23.30	22.02	0.16±0.07	-0.001± 0.006	65.5± 3.6	14.77	1.34±0.07
				10.74	21.86	20.60	0.16±0.07	-0.003± 0.005	63.4± 4.9	13.45	
79	1192	12:29:30.26	+7:59:34.565	7.46	22.21	20.83	0.26±0.11	0.006± 0.005	29.8± 69.8	14.48	1.52±0.03
				7.21	99.99	19.27	0.27±0.11	0.008± 0.003	26.5± 60.0	12.98	
80	1857	12:40:53.21	+10:28:32.38	20.82	24.04	23.41	0.50±0.10	-0.006± 0.234	-69.1± 39.6	14.82	0.92±0.15
				21.88	23.26	22.50	···	···	···	13.81	
81	1075	12:28:12.43	+10:17:52.81	14.63	23.71	22.78	0.32±0.08	0.002± 0.036	25.2± 6.9	14.96	1.20±0.14
				17.86	22.84	21.79	0.32±0.08	0.002± 0.036	32.0± 66.6	13.54	
82	1948	12:42:58.16	+10:40:54.61	10.94	23.57	22.71	0.29±0.07	0.017± 0.025	85.1± 2.7	15.52	1.05±0.14
				12.22	22.63	21.77	0.29±0.05	0.019± 0.026	84.1± 5.1	14.34	
83	1627	12:35:37.26	+12:22:55.20	3.88	21.12	20.05	0.09±0.04	0.001± 0.003	-78.2± 2.0	15.11	1.42±0.02

TABLE 4. GLOBAL STRUCTURAL PARAMETERS FOR PROGRAM GALAXIES.— *Continued*

ID	VCC	RA (J2000)	Dec (J2000)	r_e (arcsec)	$\mu(r_e)$ (mag arcsec^{-2})	$\langle\mu(r_e)\rangle$ (mag arcsec^{-2})	$\langle\epsilon\rangle$	$\langle B4\rangle$	$\langle\Theta\rangle$ (degrees)	m (mag)	$g-z$ (mag)
				4.04	99.99	18.66	0.08±0.03	0.004± 0.005	-79.2± 2.4	13.64	
84	1440	12:32:33.41	+15:24:55.54	7.87	22.41	21.14	0.02±0.01	0.001± 0.004	80.0± 24.7	14.67	1.26±0.03
				7.82	21.22	19.86	0.02±0.01	0.001± 0.004	80.5± 36.8	13.40	
85	230	12:17:19.68	+11:56:35.66	9.82	23.24	22.40	0.13±0.05	-0.003± 0.017	34.5± 30.4	15.45	1.17±0.11
				9.22	22.09	21.16	0.15±0.06	-0.001± 0.019	36.5± 44.4	14.34	
86	2050	12:47:20.67	+12:09:58.95	10.83	23.25	22.29	0.49±0.07	0.009± 0.020	-55.5± 34.9	15.12	1.16±0.05
				11.77	22.29	21.23	0.49±0.07	0.012± 0.022	-55.7± 34.7	13.88	
87	1993	12:44:12.03	+12:56:30.93	8.58	23.46	22.20	0.06±0.12	0.002± 0.015	-31.1± 16.3	15.54	1.23±0.08
				10.96	22.54	21.31	0.06±0.13	0.003± 0.020	-41.9± 35.1	14.11	
88	751	12:24:48.38	+18:11:42.49	10.01	22.62	21.64	0.45±0.03	0.005± 0.013	-48.1± 1.1	14.64	1.33±0.04
				12.98	22.01	20.68	0.45±0.03	0.005± 0.014	-48.2± 0.9	13.12	
89	1828	12:40:13.38	+12:52:28.99	14.61	23.93	22.90	0.25±0.07	0.000± 0.034	-16.9± 6.9	15.09	1.25±0.12
				16.54	22.88	21.81	0.25±0.09	-0.004± 0.027	-16.5± 32.3	13.72	
90	538	12:22:14.78	+7:10:01.014	4.87	22.44	21.34	0.07±0.02	0.001± 0.005	59.5± 9.8	15.91	1.16±0.01
				4.91	21.30	20.19	0.07±0.02	0.000± 0.006	56.1± 10.4	14.74	
91	1407	12:32:02.79	+11:53:23.65	10.26	22.99	22.08	0.15±0.03	0.000± 0.016	-30.9± 4.4	15.03	1.23±0.08
				10.95	22.00	20.93	0.15±0.03	0.000± 0.019	-28.3± 11.2	13.74	
92	1886	12:41:39.39	+12:14:50.04	12.73	23.53	22.81	0.39±0.06	0.001± 0.069	-2.6± 8.5	15.29	1.00±0.14
				13.52	22.63	21.86	0.39±0.05	0.011± 0.015	-1.9± 2.7	14.21	
93	1199	12:29:35.05	+8:03:29.008	3.53	21.84	20.47	0.10±0.10	-0.001± 0.006	59.2± 48.7	15.74	1.56±0.01
				3.43	20.06	18.85	0.11±0.10	0.000± 0.005	36.3± 36.0	14.18	
94	1743	12:38:06.74	+10:04:56.22	10.41	23.33	22.55	0.55±0.05	-0.020± 0.100	-49.9± 2.4	15.47	1.14±0.10
				10.72	22.39	21.45	0.57±0.06	-0.015± 0.021	-49.5± 2.7	14.31	
95	1539	12:34:06.81	+12:44:29.66	26.53	25.27	24.27	0.09±0.04	-0.008± 0.029	50.0± 63.2	15.15	1.21±0.13
				22.50	23.72	22.82	0.13±0.05	0.001± 0.038	52.7± 75.9	14.06	
96	1185	12:29:23.53	+12:27:03.16	18.61	24.55	23.58	0.10±0.06	-0.002± 0.019	-11.0± 45.4	15.24	1.28±0.17
				21.27	23.52	22.44	0.09±0.05	0.003± 0.024	-14.3± 70.1	13.81	
97	1826	12:40:11.23	+9:53:46.504	7.18	22.68	21.78	0.20±0.06	-0.003± 0.008	-47.1± 3.5	15.51	1.16±0.05
				6.99	21.58	20.59	0.20±0.05	-0.004± 0.016	-46.1± 4.2	14.37	
98	1512[(1)]	12:33:34.72	+11:15:42.28	497.50	99.99	29.26	0.24±0.04	-0.006± 0.016	57.1± 8.1	13.79	1.19±0.13
				77.23	26.57	24.67	0.23±0.05	-0.004± 0.015	55.0± 6.2	13.24	
99	1489	12:33:13.93	+10:55:42.08	10.46	23.68	22.98	0.35±0.06	0.003± 0.067	63.8± 13.5	15.89	1.08±0.17
				11.15	22.75	21.96	0.35±0.13	-0.010± 0.065	68.5± 34.9	14.73	
100	1661	12:36:24.75	+10:23:05.12	58.50	99.99	25.39	0.08±0.06	-0.014± 0.052	75.4± 40.7	14.55	1.28±0.22
				39.49	24.60	23.61	0.05±0.10	0.007± 0.043	-77.3± 59.8	13.63	

NOTE. — For each galaxy, the first row reports parameters in the $g-$band, the second in the $z-$band. Magnitudes and surface brightnesses are not extinction corrected. Columns 3 and 4 list the RA and Dec of the galaxy center, at J2000, measured directly from the images (to be compared to the values given in Table 1). Column 5 lists the effective radius of the galaxy; these coincide with the values listed in column 7 of Table 3 for galaxies best fit by a Sérsic model, but are slightly larger for the galaxies best fit by a core-Sérsic model (for which column 7 of Table 3 lists the r_e of the Sérsic model fitting the outer parts). Columns 6 and 7 list the surface brightness at r_e, measured directly from the images when possible, and the mean surface brightness within r_e, integrated from the best fitting model. Columns 8, 9 and 10 list the average ellipticity, B4 coefficient, and major axis position angle measured between $1''$ and r_e. Average values are not listed if less than four points are available to compute the mean and standard deviation. Finally, the magnitudes listed in the next to last column exclude the nucleus, and are obtained by integrating the best fit profile to infinity. The colors listed in the last column are measured directly from the surface brightness profile for $1'' < r < r_e$. To avoid errors associated with the background subtractions, surface brightness values 1 mag below the sky or fainter are excluded.

(1) Based on the dIrr/dE nature of this object, the irregular profile shape, and the large discrepancy between the values of r_e measured in the two filters, r_e and all integrated quantities for this galaxy are deemed unreliable.

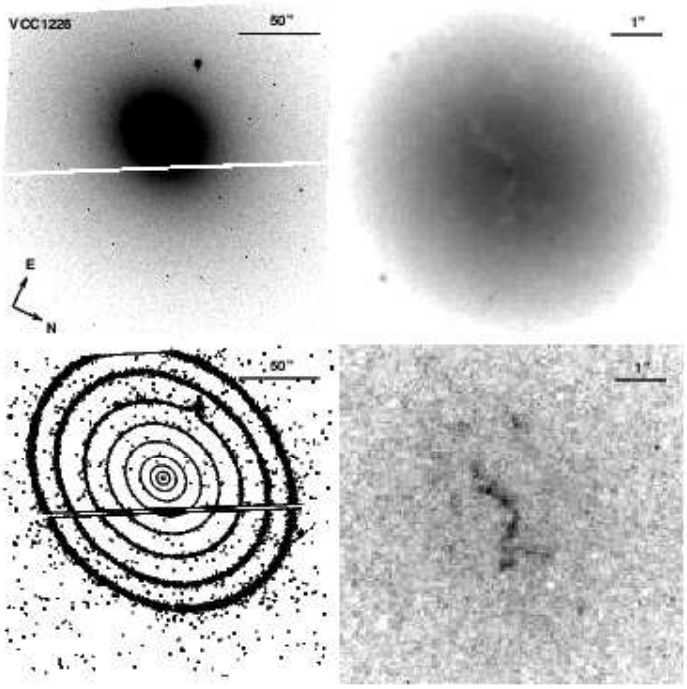

FIG. 1.— The ACSVCS $g-$band image for VCC 1226 (=M49; NGC 4472, Hubble Type E2/S01(2), see Table 1), the first ranked member of Virgo. The top panels show the ACS/WFC/F475W full frame (left panel) and a zoom towards the center (right panel). The bottom left panel shows a contour map of the $g-$band frame, with levels drawn at 0.05,0.1,0.2,0.4,0.8,1.6,3.2,6.4,12.8,25.6 electrons s^{-1} $pixel^{-1}$ (22.82 mag $arcsec^{-2}$ to 16.04 mag $arcsec^{-2}$, see equation 4). Finally, the bottom right panel shows a central section of the $g-z$ color image, with red regions appearing as dark areas and blue regions as light. The linear scale is shown in each panel. All images have been background subtracted.

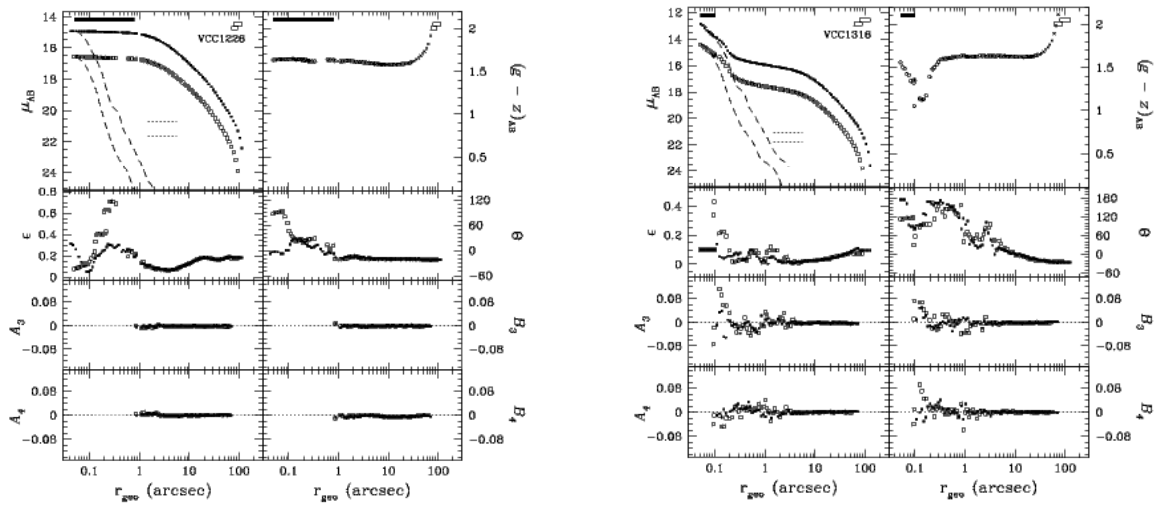

FIG. 2.— *(Left Panel)* Isophotal parameters for VCC 1226 (=M49; NGC 4472, Hubble Type E2/S01(2), see Table 1), plotted against the 'geometric mean' radius $r_{geo} = a \times \sqrt{1-\epsilon}$, with a measured along the semi-major axis of the galaxy. The panels show surface brightness (in magnitude $arcsec^{-2}$) in both g (open squares) and $z-$ bands (filled squares), $g-z$ color profile (both uncorrected for extinction), ellipticity, position angle (in degrees, measured from North to East) and parameters measuring deviations of the isophotes from pure ellipses. In all panels with the exception of the top right, open and closed symbols refer to g and $z-$band data respectively. Data are only plotted between $0''.049$ (= 1 WFC pixel) and the radius at which the galaxy counts fall below 10% of the sky; sky surface brightnesses are shown by the two short dashed horizontal lines (the fainter sky level is in the $g-$band). Crosses are used in plotting the color profile when the sum of the (background subtracted) counts in the two filters is lower than the sum of the background levels. Finally, a full horizontal bar in the top-left panel identifies a region where the analysis was performed on images corrected for dust obscuration, while two open horizontal bars identify regions where the fit was performed with fixed values of ϵ and θ (the topmost bar is for the z-band data, the bottom bar for the g-band data). Higher order coefficients are not shown in these regions (see text for further details). *(Right panel)* The same as for the left panel, but for VCC 1316 (=M87; NGC 4486, Hubble Type E0).

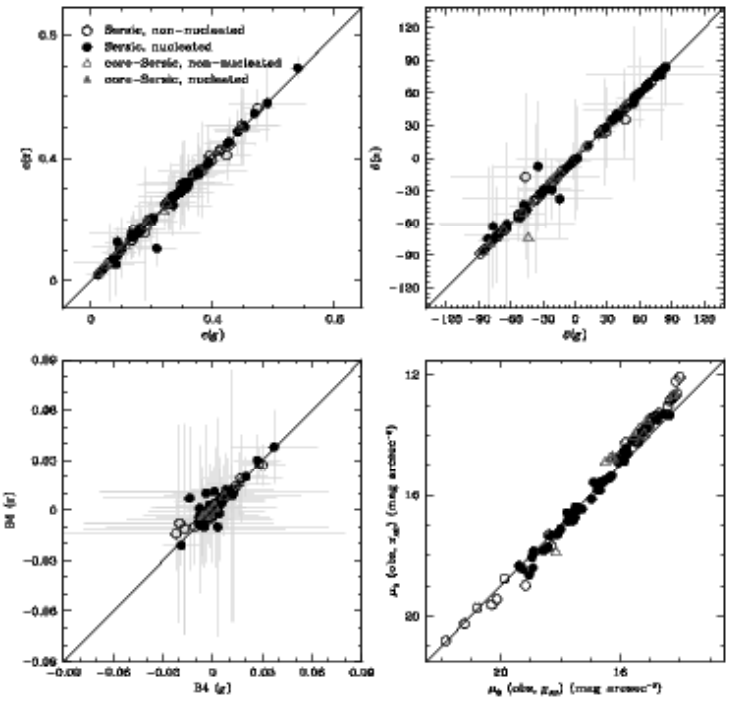

FIG. 3.— Comparison of the mean ellipticity, ϵ, position angle, θ, B4 coefficients, and extinction corrected central surface brightness, μ_0, measured in the g and $z-$bands. The mean values are calculated between $1''$ and one effective radius, excluding regions affected by dust or nuclei. Standard deviations from the mean values are plotted in yellow to avoid over-crowding the plot – such standard deviations are over-estimates of the intrinsic errors in the mean, since they are affected by real radial variation in ϵ, θ and B4. Filled and open symbols represent nucleated and non-nucleated galaxies respectively. Galaxies best fit by a Sérsic profile are shown in black; galaxies best fit by a core-Sérsic profile are shown in red (see §3.3).

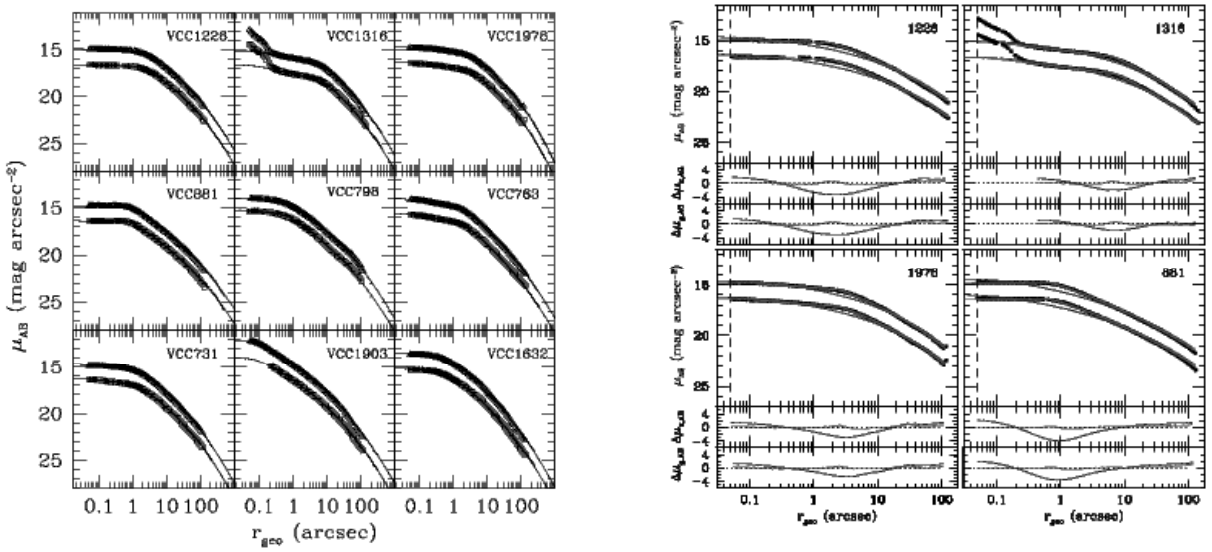

FIG. 4.— (Left) Composite surface brightness profiles, obtained by combining the ACSVCS g and $z-$band profiles (shown as open symbols) with ground-based $B-$band profiles drawn from the literature, and plotted as a function of the geometric mean radius. The solid curve represents the best-fit core-Sérsic model to the final composite profile (shown as solid symbols). For each galaxy, the brighter of the two profiles is measured in the $z-$band.

FIG. 5.— (Right) Surface brightness profiles in g (lower points) and z (upper points) for four galaxies in the ACS Virgo Cluster Survey. The data are plotted up to the radius at which the surface brightness falls below 10% of the sky, as in Figure 2. For each galaxy, and in each filter, we show as a solid line the best-fit Sérsic (blue) and core-Sérsic (red) models, each with the addition of a nuclear component when necessary (in these cases, the best fits to the nucleus and the galaxy are shown separately as dotted and dashed lines respectively). Residuals from the best fit are shown in the panels below over the range of radii used in constraining the fit (see text for further details). The data are plotted against the geometric mean radius. The dotted vertical line is placed at r=$0''.049$, corresponding to the ACS/WFC pixel size.

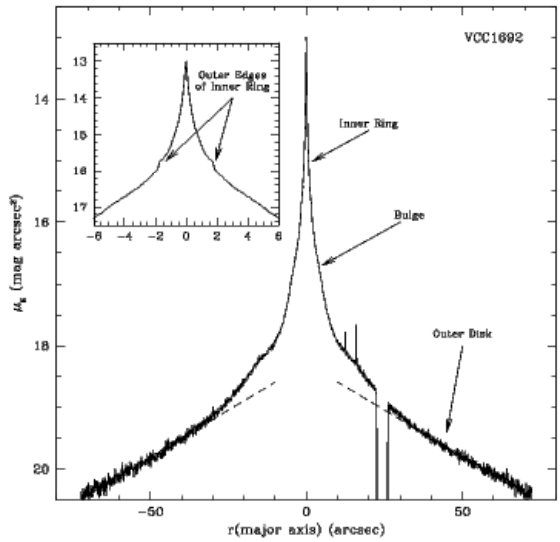

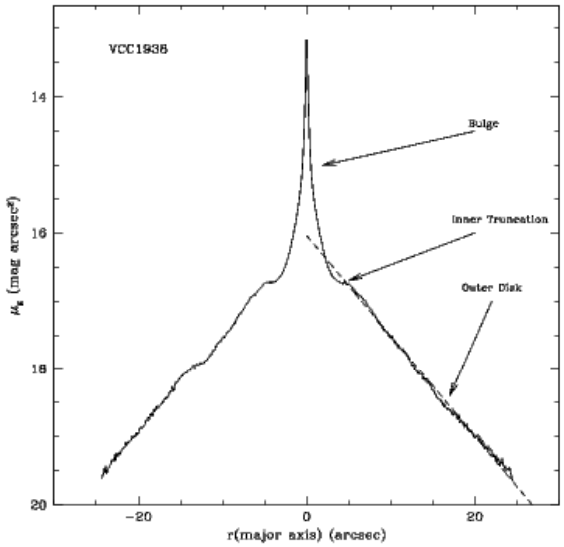

FIG. 6.— (Left) A cut through the $g-$band photometric major axis of VCC 1692 (NGC 4570), highlighting the several morphological components. As shown by the dashed line, the outer profile, dominated by a thin stellar disk, is roughly exponential. The bulge contribution is visible in the inner $\sim 20''$. The innermost $1''.8$ are dominated by the nuclear ring, the outer boundary of which are clearly visible in the expanded view shown in the inset.

FIG. 7.— (Right) A cut through the $g-$band photometric major axis of VCC 1938 (NGC 4638), clearly showing the inner truncation of he outer exponential disk.

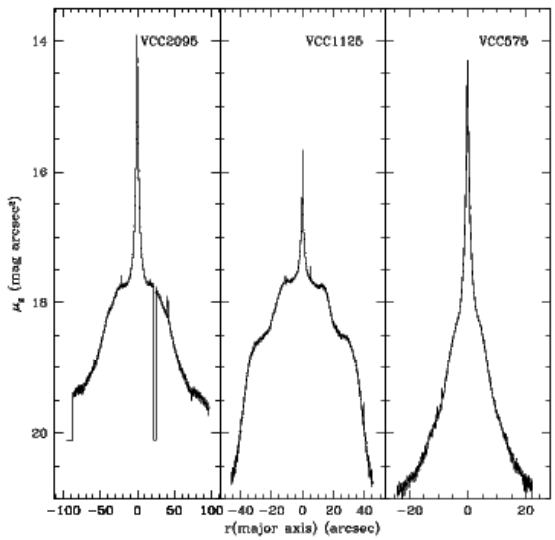

FIG. 8.— (Left) Residual map of VCC 1125, obtained by subtracting the best fitting isophotal model from the $g-$band image.

FIG. 9.— (Right) Cuts through the $g-$band photometric major axes of VCC 2095 (NGC 4762), VCC 1125 (NGC 4452) and VCC 575 (NGC 4318).

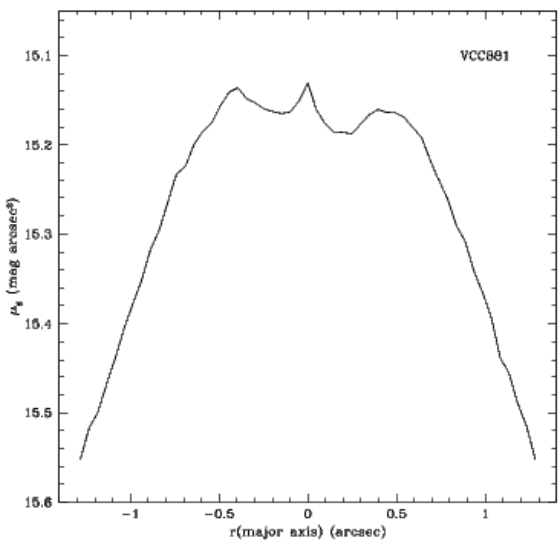

FIG. 10.— (Left) A cut through the $g-$band photometric major axis of VCC 881 (NGC 4406), showing the decrease in the surface brightness profile in the inner $0''.4$.

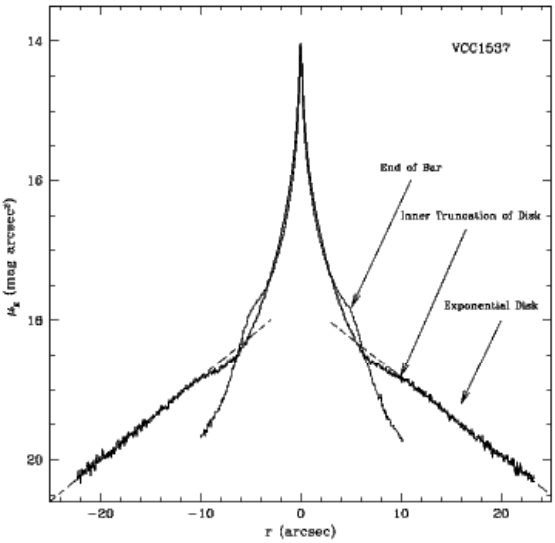

FIG. 11.— (Right) Cuts through the $g-$band photometric major axis (thick solid line) and through the bar axis (thin solid line) of VCC 1537 (NGC 4528) − the latter is misaligned by roughly 30° relative to the minor axis of the galaxy. The inner truncation in the exponential disk (approximated by the dashed line), as well as the ends of the bar are marked

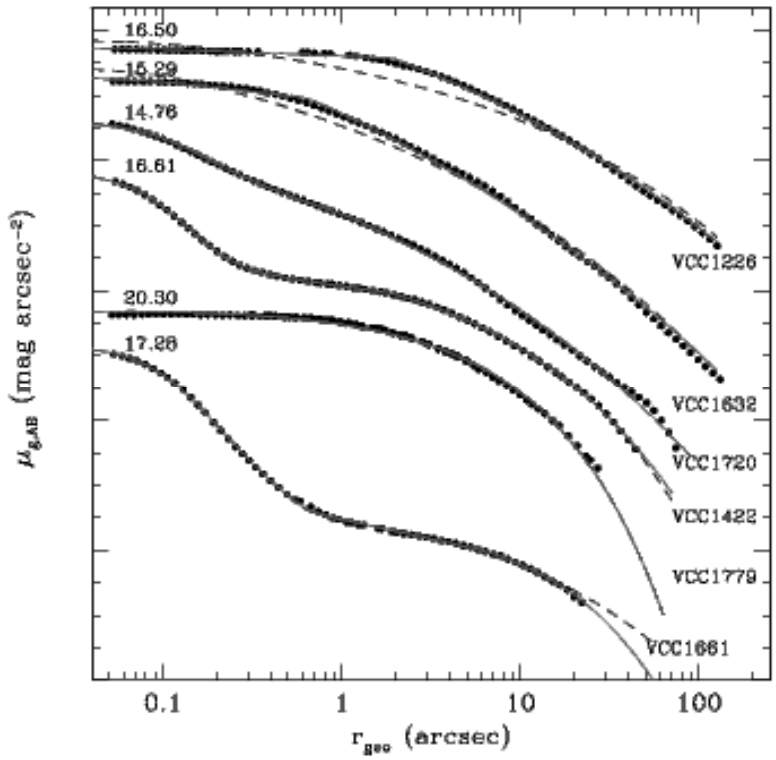

FIG. 12.— Representative $g-$band surface brightness profiles for six galaxies in the ACS Virgo Cluster Survey, from the brightest (VCC 1226) to the faintest (VCC 1661) galaxy in the sample, plotted as a function of the geometric mean radius. All galaxies are "regular" ellipticals, in the sense of not displaying significant morphological peculiarities (with the exception of the possible presence of a nuclear component). The galaxies are arranged, from top to bottom, in order of increasing total B-band magnitude (decreasing luminosity). They have been shifted in the vertical direction for clarity; the value of the $g-$band surface brightness profile at $0''.049$ is listed on the left-hand-side next to each galaxy profile, and tickmarks on the ordinate axis are separated by 1 mag arcsec^{-2}. For each galaxy, we overplot the best-fit Sérsic (dashed) and core-Sérsic (solid) model, with addition of a King model for nucleated galaxies (VCC 1720, VCC 1422 and VCC 1661).

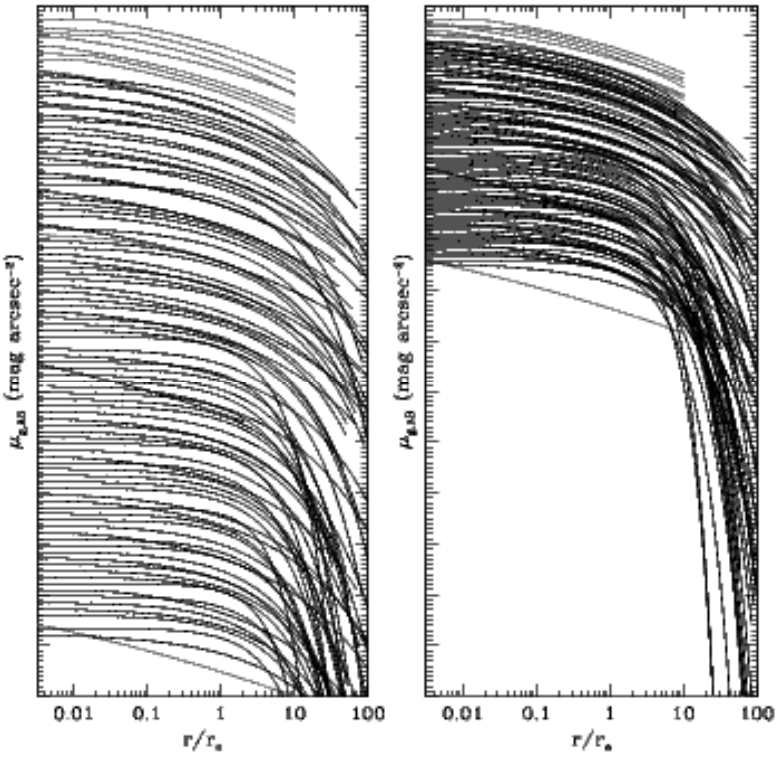

FIG. 13.— A compilation of the best-fit models for the $g-$band surface brightness profiles of all ACSVCS galaxies. The models exclude a nuclear component when present, and are shown before convolution by the ACS/WFC PSF. For each galaxy, the abscissa shows the isophotal radius normalized to the effective radius r_e, derived from the best fit. Along the ordinate, galaxies are ordered according to their total B-band magnitudes, with the brightest galaxy (VCC 1226) plotted as having the largest central surface brightness, and every other galaxy plotted as having central surface brightness shifted downwards, by a constant amount, relative to that of VCC 1226. Each small tick on the ordinate corresponds to 1 magnitude arcsec^{-2}. The two panels differ only in the range of surface brightness shown: to the right, the scale is shown to highlight difference in the innermost region. In both panels, galaxies best fitted by a core-Sérsic profile are shown in red.

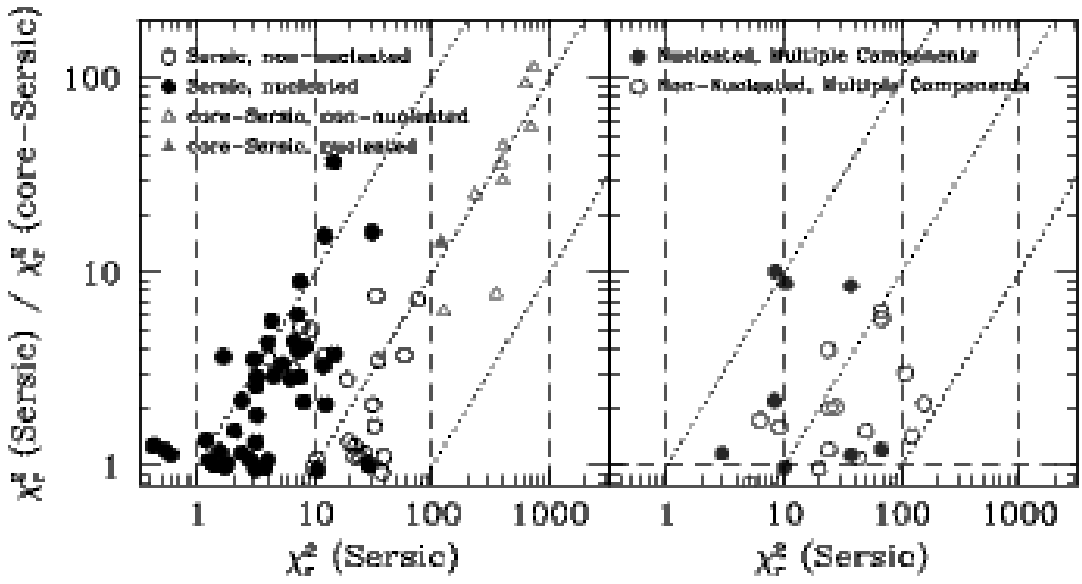

FIG. 14.— The ratio of the reduced χ^2 of the Sérsic and core-Sérsic fits *vs* the reduced χ^2 for the best Sérsic fit (see text for details). Galaxies with stellar disks or bars are shown in the right panel, 'regular' galaxies in the left panel. The dotted lines represent locii for which (from left to right) χ^2_r(core-Sérsic)=1,10,100; the dashed lines have the same meaning for χ^2_r(Sérsic). Galaxies plotted as triangles are best fit by a core-Sérsic profile.

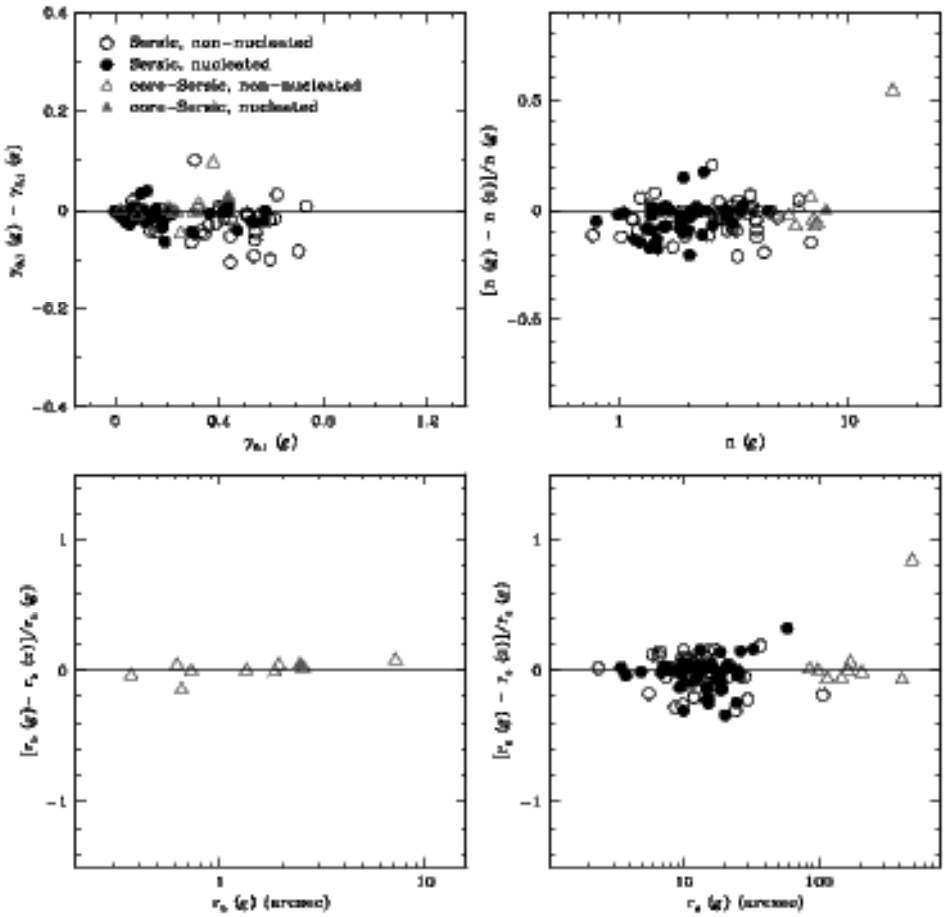

FIG. 15.— Comparison of γ, n, break and effective radii (r_b and r_e) for the best fits to the surface brightness profiles in the g and $z-$bands. Galaxies are color-coded as in Figure 3. In the case of galaxies best fit by a Sérsic profile, the logarithmic slope γ is calculated at $0''.1$ from the center, and is uniquely defined by n and r_e (see equation 16).

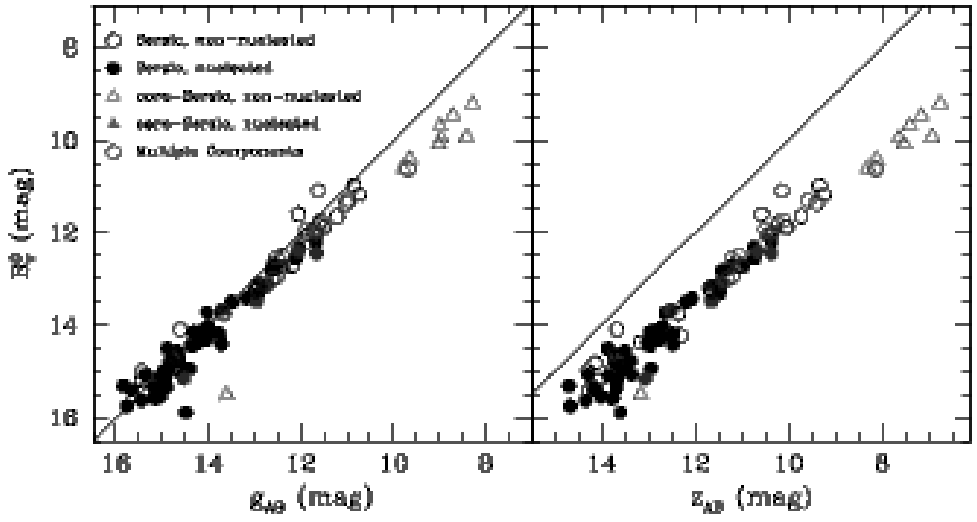

FIG. 16.— Comparison of the g and $z-$band total magnitudes, corrected for extinction, derived by integrating to infinity the best fitting surface brightness profiles, compared to the B_T^0 magnitudes from the RC3. The diagonal line shows a one-to-one correspondence. Galaxies with multiple morphological components, for which the model fits are not always satisfactory, are plotted in blue.

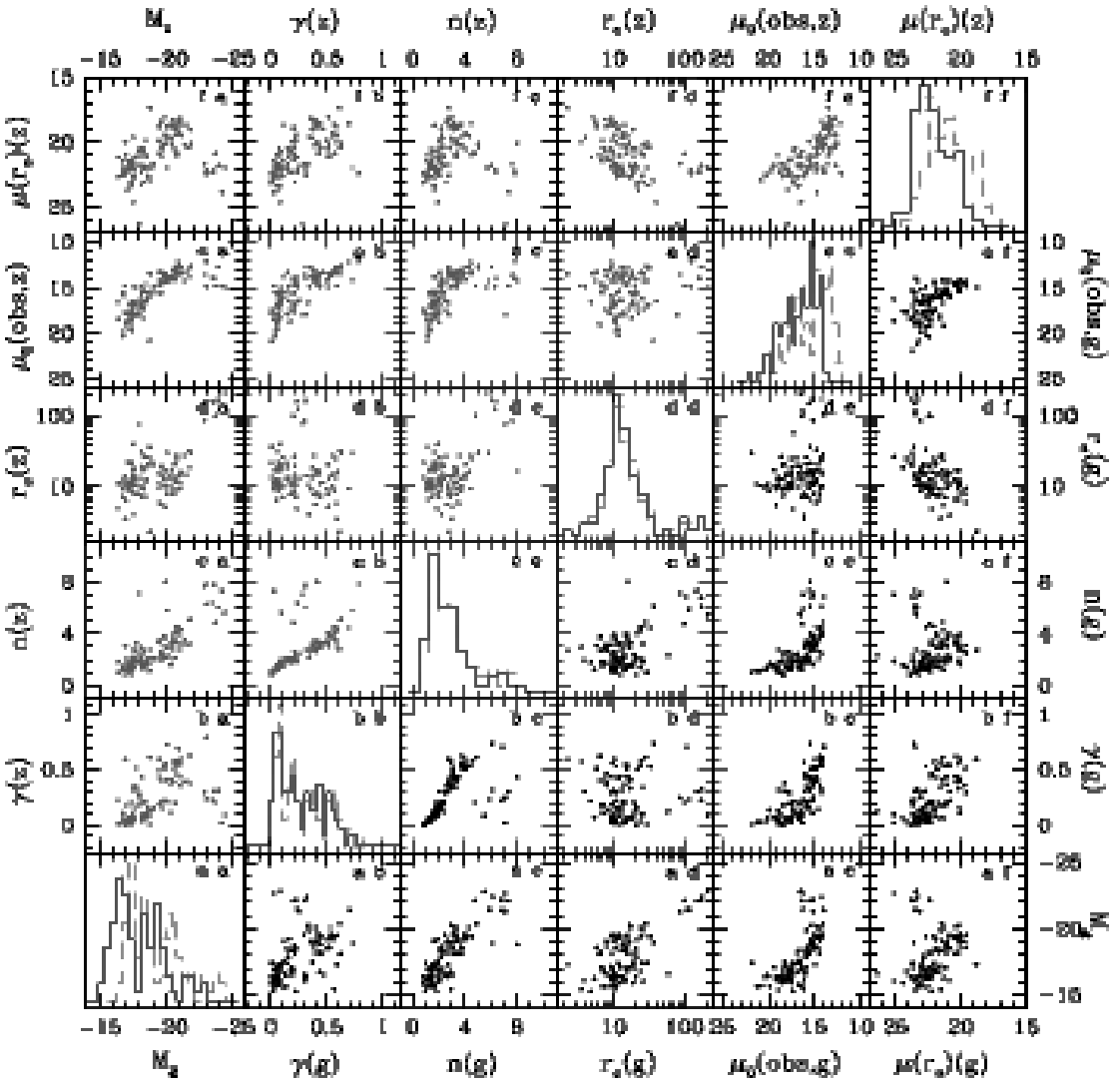

FIG. 17.— Correlations between fit parameters: total absolute magnitude from the model profile, integrated to infinity and extinction corrected; inner slope γ (in the case of galaxies best fit by a Sérsic profile, γ is defined as the logarithmic slope at $0''.1$ from the center, see equation 16); Sérsic index n; effective radius r_e, in arcseconds; extinction corrected central surface brightness μ_0 in mag arcsec^{-2}, measured directly from the images at $0''.049$, and therefore including a nuclear component when present; and extinction corrected surface at r_e, in mag arcsec^{-2}. Parameters recovered for the g and $z-$band images are shown in the panels below and above the diagonal line running from bottom-left to top-right, respectively. Histograms of each of the parameters (drawn as a solid and dashed line for the g and $z-$band respectively), are shown along the diagonal (the y-axis scale is not shown for the histograms). In this and all subsequent figures, histograms are created by binning the data with an "optimal" bin size given by $2 \times IQR \times N^{-1/3}$ (Izenman 1991), where N is the total number of objects, and IQR is the interquartile range (i.e. the range which includes the second and third quartile of the ranked distribution of the parameter under investigation).

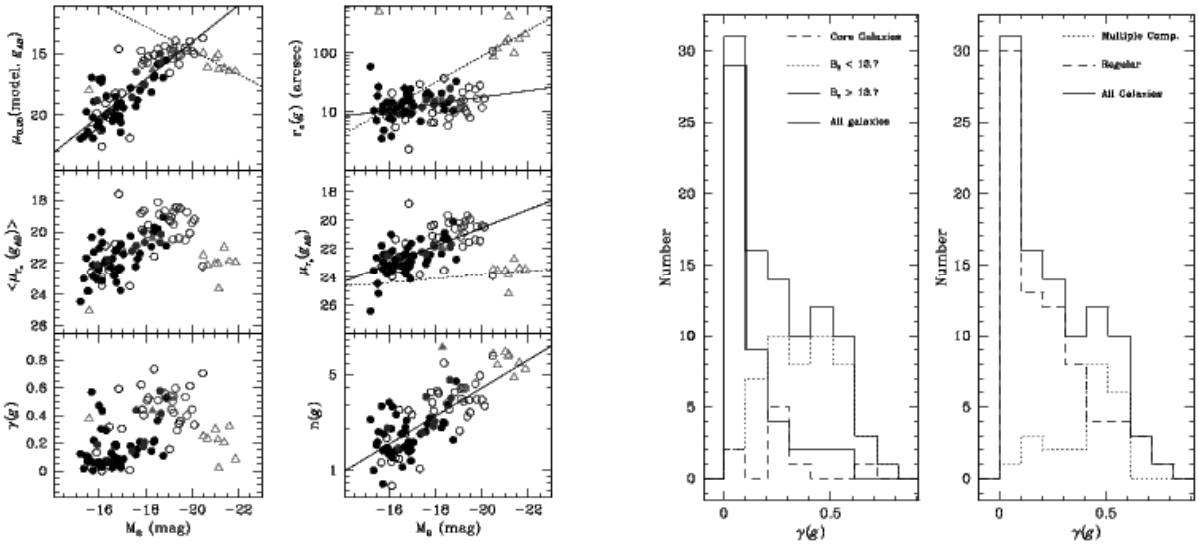

FIG. 18.— (Left) Correlation of parameters characterizing the inner (on the left) and outer (on the right) surface brightness profile and the total $B-$band magnitude of the host galaxies. On the left panels, from top to bottom, are shown the surface brightness measured from the best fitting model at $0''.049$, *prior* to PSF convolution and excluding a nuclear component, if present; the average surface brightness within one effective radius r_e, in mag arcsec^{-2}; and the slope γ of the inner profile at $r = 0''.1$, measured prior to PSF convolution (following equation 16 in the case of profiles best fit by a Sérsic model). On the right panels are shown the effective radius r_e; the surface brightness at r_e, in mag arcsec^{-2}; and the Sérsic index n characterizing the shape of the outer profile. Galaxies are color-coded as in the legend of Figure 16, blue points refer to galaxies with multiple morphological components.

FIG. 19.— (Right) The distribution of the $g-$band inner slope γ of the galaxy profile (i.e excluding a nuclear component) for the entire sample (shown by the solid line), and the sample divided according to their total $B-$band magnitude (left panel) and the presence of multiple morphological components (right panel). γ is measured from the best fit profiles, and therefore represents the slope prior to PSF convolution and excluding a nuclear component. In the case of galaxies best fit by a Sérsic profile, γ is measured at $0''.1$ from the center following equation 16.

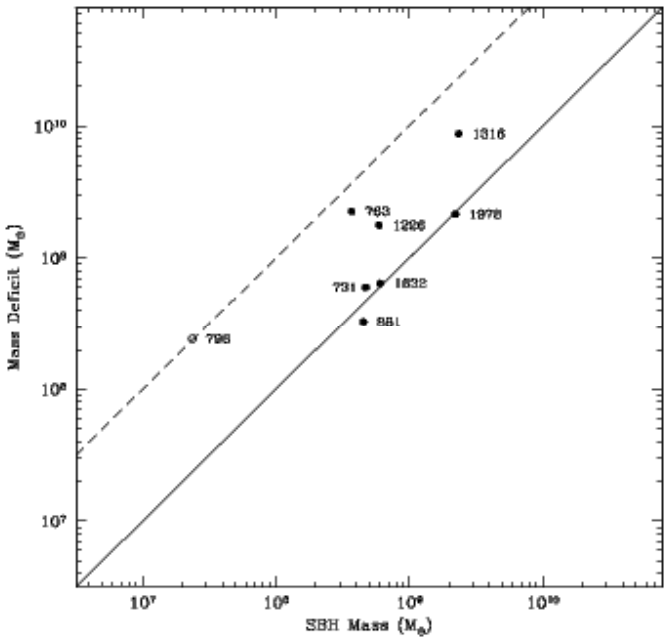

FIG. 20.— The core "mass deficit", defined as the difference between the mass enclosed within the break radius by the Sérsic model that best fits the outer surface brightness profile and the best fit core-Sérsic model, plotted against the mass estimated for the nuclear SBH (see text for details). The solid and dashed lines are plotted for a mass deficit equal to, and ten times larger than, the SBH mass. VCC 798 (NGC 4382), shown by the open circle, is likely to host a large scale stellar disk.

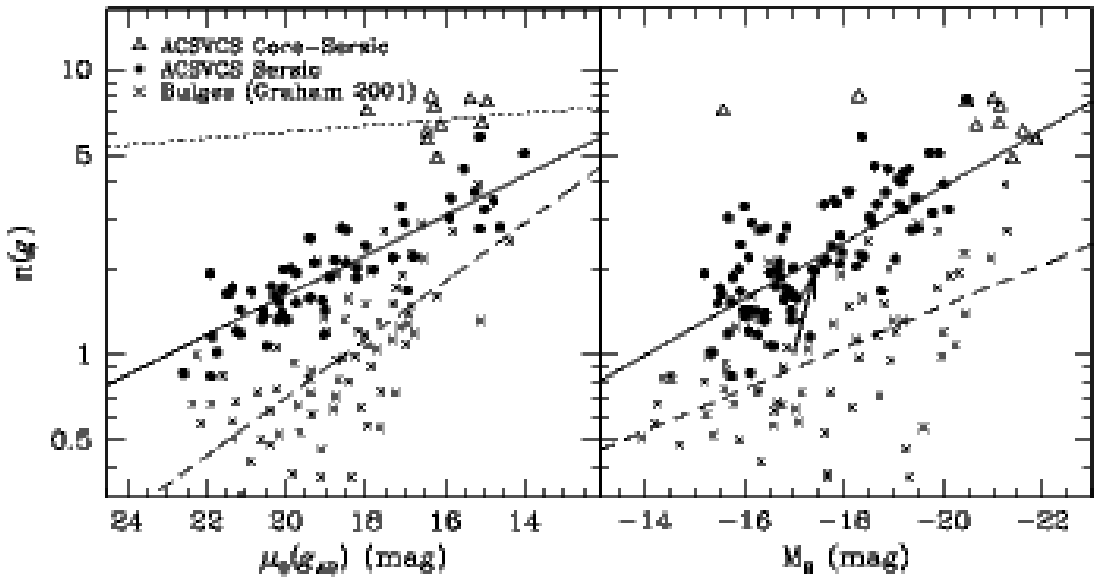

FIG. 21.— Left panel: The Sérsic index n, plotted against the surface brightness estimated from the best fitting model at $0''.049$, *prior to* PSF convolution. Right panel: n, plotted against the total, extinction corrected absolute $B-$band magnitude of the host galaxy (from the RC3). The ACSVCS galaxies are shown as solid circles and open triangles depending on whether the surface brightness profile is best fit by a Sérsic or core-Sérsic model, respectively. Crosses represent bulges from Graham (2001); $B-$band central surface brightnesses from this paper have been converted to $g-$band by assuming $g - B \sim 0.55$ (Fukugita et al. 1995), in addition the bulge data have been extinction corrected and total magnitudes have been rescaled to $H_0 = 72$ km/s/Mpc. The solid line represents the best least square fit to the "Sérsic" galaxies (solid circles), the dotted line shows the best least square fit to the "core-Sérsic" galaxies, and the dashed line shows the best fit to the bulges. The arrow in the bottom right panel shows the change in n and M_B undergone by an exponential ($n = 1$) bulge after merging with a satellite of half its mass, according to N-body simulations by Eliche-Moral et al. (2005).

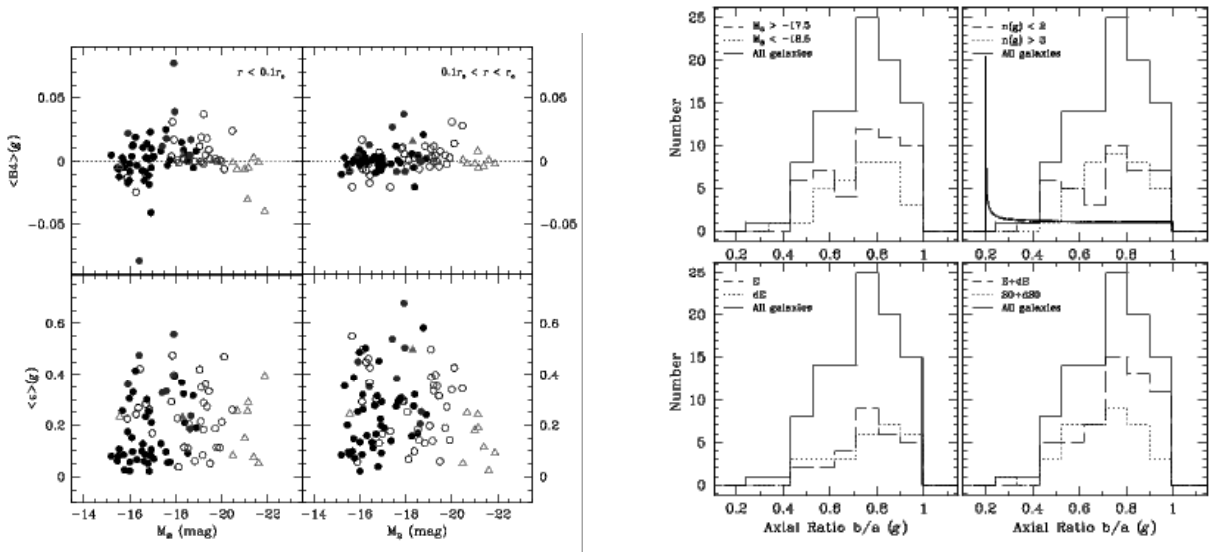

FIG. 22.— (Left) Correlations between the extinction corrected $B-$band magnitude and mean ellipticity and B4 coefficients. The latter are calculated within 10% of the effective radius r_e (excluding the nuclear region, if a nucleus is present) in the left panels, and between $0.1r_e$ and r_e in the panels to the right. Galaxies are color-coded as in the legend of Figure 16, blue points refer to galaxies with multiple morphological components.

FIG. 23.— (Right) The distribution of minor to major axes ratios, b/a, for the ACSVCS galaxies. In all panels, the thick solid line shows the distribution for the entire sample. In the upper left and right panels the sample is divided according to absolute $B-$band magnitude and Sérsic index n respectively; the thick continuous line in the right panel shows the distribution of axial ratios expected for a population of galaxies with intrinsic $b/a = 0.2$ and seen at random orientations. In the bottom left and right panels, the sample is divided according to morphological classification.

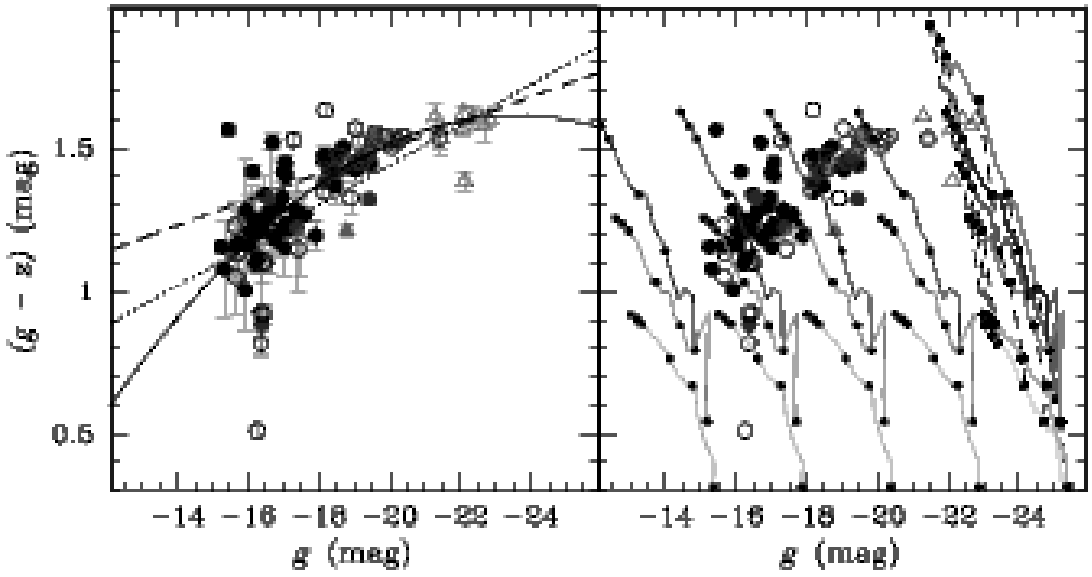

FIG. 24.— Color-Magnitude diagram for the 100 galaxies which comprise the ACSVCS. Galaxies are-coded as in Figure 16. In the left panel, the data are plotted with errorbars; the dashed and dotted lines corresponds to least-square fits to galaxies fainter and brighter than $M_g = -18$ respectively, while the curved line represents the best quadratic fit to the entire sample (see equations 31, 32 and 33). The solid lines in the right panel show the prediction of the stellar population synthesis models of Bruzual & Charlot (2003). Models of constant metallicity and varying age are shown as solid lines for [Fe/H]=−2.25 (yellow), −1.65 (cyan), −0.64 (green), −0.33 (red), +0.09 (blue), +0.56 (magenta). Points along the isometallicity tracks corresponds to ages of 1, 2, 4, 8, 12, 15 Gyr (from left to right). Finally, from top to bottom, the $g-$band magnitudes have been scaled to a total mass $M = 10^{12}$, 10^{11}, 10^{10}, 10^{9}, and 10^{8} $M_\odot$. All magnitudes have been extinction corrected.

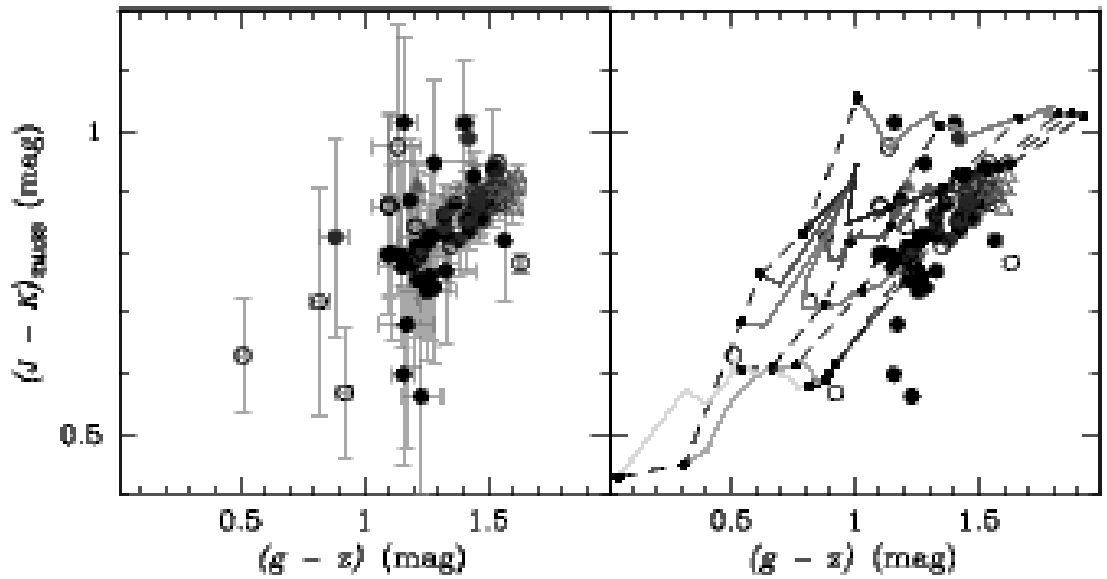

FIG. 25.— $g - z$ vs $J - K$ color-color diagrams. J and $K-$band magnitudes are from the 2MASS database. Galaxies are coded as in Figure 24, as are the stellar population synthesis models. All magnitudes have been extinction corrected.